A Subgrid Model for Supernova Remnants as Sources of Cosmic Rays in Cosmological Hydrodynamical Simulations

Daniel Karner

Munich 2023

A Subgrid Model for Supernova Remnants as Sources of Cosmic Rays in Cosmological Hydrodynamical Simulations

Daniel Karner

Master's thesis
at the University Observatory Munich
Faculty of Physics at the Ludwig-Maximilians-Universität in Munich

submitted by
Daniel Karner
from Rohrbach bei Mattersburg

Supervisor: apl. Prof. Dr. Klaus Dolag
Co-supervisors: Dr. Ildar Khabibullin & Ludwig M. Böss, MSc

Munich, 17.08.2023

Ein Subgitter-Modell für Supernovaüberreste als Quellen von kosmischer Strahlung in kosmologischen hydrodynamischen Simulationen

Daniel Karner

Masterarbeit
an der Universitäts-Sternwarte München
Fakultät für Physik der Ludwig-Maximilians-Universität München

vorgelegt von
Daniel Karner
aus Rohrbach bei Mattersburg

Betreuer: apl. Prof. Dr. Klaus Dolag
Mitbetreuer: Dr. Ildar Khabibullin & Ludwig M. Böss, MSc

München, den 17.08.2023

Contents

List of Figures ix

List of Tables xi

Abstract xiii

Zusammenfassung xv

1 Introduction 1
- 1.1 Comment on units and notation . . . 2
- 1.2 Overview over cosmic ray physics . . . 3
- 1.3 Sources of cosmic rays . . . 7
- 1.4 The supernova paradigm . . . 8
  - 1.4.1 Basic arguments . . . 8
  - 1.4.2 Radiation signatures . . . 11

2 Particle acceleration at collisionless shocks 15
- 2.1 A brief historical overview . . . 15
- 2.2 Elementary considerations . . . 16
- 2.3 Macroscopic approach . . . 16
- 2.4 Microscopic approach . . . 20
- 2.5 Summary of assumptions . . . 23

3 A model for cosmic ray spectra from supernova remnants 27
- 3.1 Different types of supernovae . . . 27
- 3.2 Evolution of supernova remnants . . . 29
- 3.3 Cosmic ray spectrum at the shock front . . . 33
- 3.4 Magnetic field amplification . . . 35
- 3.5 Energy loss mechanisms . . . 40
- 3.6 Contributions to the overall CR spectrum . . . 44
- 3.7 Constraining the model parameters . . . 48

4 Numerical implementation 51
- 4.1 Cosmic ray model in *OpenGadget3* . . . 52
- 4.2 Sub-grid implementation of CR spectra . . . 53
- 4.3 Coupling supernova seeding to star formation in *OpenGadget3* . . . 55

5 Test simulations and results 57
- 5.1 Test environment for CR seeding . . . 57
- 5.2 Simulation of a galaxy with simple power-law seeding . . . 57

6 Conclusions 65

A List of abbreviations **67**

B Used software **69**

C The distribution function and its moments **71**

D Derivation of the time $t_0(r,t)$ **75**

E Adiabatic energy losses **77**

Bibliography **82**

Danksagung **83**

Selbstständigkeitserklärung **85**

List of Figures

1.1 All-particle cosmic ray spectrum from Evoli (2020) 4
1.2 Spectral energy distribution of supernova remnant G106.3+2.7 12

2.1 Shock geometry 17
2.2 Probability for a randomly oriented vector to have a certain angle to a fixed direction (kindly provided by Julian Sommer) 20

3.1 Shock radius and velocity 32
3.2 Downstream magnetization versus shock velocity 34
3.3 Maximum proton momentum at shock. 36
3.4 Power spectrum of unordered magnetic field component 36
3.5 Motion of a charged particle in magnetic fields with different strengths 37
3.6 Magnetic field amplification upstream and downstream. 39
3.7 Adiabatic loss function $L(t_0, t)$ 42
3.8 CR proton and electron spectrum for a supernova of type Ia 46

4.1 Testcase for the discretization routine 53

5.1 Initial setup for testcase of CR seeding 58
5.2 Time development of gas particle distribution in our test bed 58
5.3 Radial pressure profiles 60
5.4 Temporal evolution of simulated galaxy. 61
5.5 Average magnitude of magnetic flux density $\langle|\mathbf{B}|\rangle$ along the line of sight (head-on projection). 62
5.6 Average magnitude of magnetic flux density $\langle|\mathbf{B}|\rangle$ along the line of sight (edge-on projection). 62
5.7 Surface mass density. 63
5.8 Gas temperature averaged along the line of sight. 63
5.9 Cosmic ray proton pressure. 64
5.10 Cosmic ray electron pressure. Note the clumpy structure in the early snapshots due to spatially discrete seeding by SNRs. 64

D.1 Time when plasma at a given location was shocked 76

List of Tables

3.1 Parameters for the three different types of supernovae in our model 33
3.2 Additional free model parameters 48

Abstract

In this Master's thesis we introduce a sub-grid model for the SPH code *OpenGadget3*, which describes supernova remnants as cosmic ray sources. After some initial explanations of the main features of the cosmic ray energy spectrum, arguments are presented showing that supernova remnants are by far the most important source of Galactic cosmic rays. The particles are accelerated by the shock wave of the ejected material. The underlying physical mechanism is the so-called diffusive shock acceleration, which is briefly presented in a separate chapter. In particular, from simple basic assumptions it is shown that the resulting particle spectrum in momentum space is a power-law.

Based on that, in the main part of this work we describe how the particle spectrum can be calculated, which is finally released into the interstellar medium by supernova remnants. The model includes descriptions for the time evolution of shock radius and velocity, particle escape, amplification of the self-generated magnetic field, and energy losses from adiabatic expansion as well as from synchrotron radiation and inverse Compton scattering. The resulting spectra for protons and electrons largely follow a power-law and consist of two components. These include high-energy particles escaping at the shock front and less energetic ones, which suffer from energy losses inside the supernova remnant before being released.

In addition to the theoretical part of this work, we briefly discuss the numerical implementation in *OpenGadget3* in the last two chapters and also go into the existing modules for star formation and cosmic rays. Finally, we show graphically visualized results of the simulation of a spiral galaxy, which, among other things, illustrates the injection of cosmic rays by supernova remnants.

Zusammenfassung

In dieser Masterarbeit führen wir ein Subgitter-Modell für den SPH-Code *OpenGadget3* ein, welches Supernovaüberreste als Quellen von kosmischer Strahlung beschreibt. Nach einigen anfänglichen Erläuterungen zu den wichtigsten Eigenschaften des Energiespektrums der kosmischen Strahlung werden Argumente vorgestellt, die zeigen, dass Supernovaüberreste die mit Abstand wichtigste Quelle von galaktischer kosmischer Strahlung sind. Die Teilchen werden dabei an der Stoßwelle des ausgeworfenen Materials beschleunigt. Der zu Grunde liegende physikalische Mechanismus ist die sogenannte diffusive Stoßbeschleunigung, welche in einem eigenen Kapitel kurz vorgestellt wird. Insbesondere wird mit einfachen Grundannahmen gezeigt, dass das resultiernde Teilchenspektrum im Impulsraum ein Potenzgesetz ist.

Davon ausgehend, beschreiben wir im Hauptteil dieser Arbeit, wie das Teilchenspektrum berechnet werden kann, welches von Supernovaüberresten letztendlich in das interstellare Medium freigesetzt wird. Das Modell beinhaltet Beschreibungen für die zeitlichen Entwicklung des Stoßwellenradius und der -geschwindigkeit, das Entkommen von Teilchen, die Verstärkung des selbsterzeugten Magnetfeldes und Energieverluste durch adiabatische Ausdehnung sowie durch Synchrotronstrahlung und inverse Compton-Streuung. Die resultierenden Spektren für Protonen und Elektronen folgen weitgehend einem Potenzgesetz und setzen sich aus zwei Komponenten zusammen. Dazu gehören hochenergetische Teilchen, die an der Stoßfront entweichen und weniger energiereiche, die im Inneren des Supernovaüberrests Energieverluste erleiden, bevor sie freigesetzt werden.

Neben dem theoretischen Teil dieser Arbeit diskutieren wir in den letzten beiden Kapiteln noch kurz die numerische Implementierung in *OpenGadget3* und gehen dabei auch auf die bereits vorhandenen Module für Sternentstehung und kosmische Strahlung ein. Zum Abschluss zeigen wir grafisch visualisierte Ergebnisse der Simulation einer Spiralgalaxie, welche unter anderem die Injektion von kosmischer Strahlung durch Supernovaüberreste veranschaulicht.

1 Introduction

Cosmic rays (CRs) are highly energetic, non-thermal particles that are part of the thin medium between stars in a galaxy and galaxies within a cluster. The study of their origin, propagation and interaction with other components of the interstellar medium (ISM) forms one of the most active branches of contemporary research that is referred to as "high-energy astrophysics". Since the discovery of cosmic rays by the Austrian physicist and Nobel laureate Victor Franz Hess more than a century ago (see Hess, 1912), who referred to them as "durchdringende Strahlung", the combined efforts of theorists and experimentalist from different fields, like particle, plasma and astrophysics, have greatly expanded our knowledge of these high-energy particles. Yet, there are still many open questions concerning the composition, origin and propagation of cosmic rays. They will be addressed by future observational campaigns and more detailed simulations, which become possible due to the increasing power of computers.

One could ask the question if cosmic ray physics is not just a sub-branch of particle physics or if astrophysicists should care about this at all. Therefore, we will briefly motivate the relevance of cosmic rays in the theoretical framework of modern astrophysics by following the arguments in Draine (2011). Firstly, it is interesting to observe that the energy densities of various quantities in the local interstellar medium – like the magnetic flux density, far-infrared radiation from dust, starlight, thermal kinetic energy, turbulent kinetic energy and cosmic rays – are all comparable in magnitude and lie within the range from 0.2 MeV m^{-3} to 2 MeV m^{-3} (see Draine, 2011, tab. 1.5). This near-equipartition is only partly coincidental (e.g. the cosmic microwave background radiation has an energy density that lies within the above range) and illustrates that there must exist a number of feedback processes that couple the energy densities of different ISM components. For example, magnetic field amplification through turbulent motions of plasma might explain the similarity between magnetic and turbulent energy density. One can also argue that if the starlight energy density was much larger than the gas pressure, the radiation pressure acting on dust grains could remove gas from the galactic plane, which would regulated star formation. Similarly, if the cosmic ray energy density significantly exceeded that of the magnetic field, they could not be confined and would escape the galaxy more rapidly, which would lead to a decline in u_{CR}. Moreover, cosmic rays contribute to the heating of gaseous and molecular clouds and they can penetrate deep into the dust cocoons surrounding proto-stars (dark clouds), which are optically very thick to almost all kinds of electromagnetic radiation (especially UV). Therefore, cosmic rays are the only source of ionising radiation (and heating) inside dense molecular clouds and influence chemical reaction chains (e.g. the formation of OH and H_2O, which require the ionization product H_3^+ as a starting point). Even more important than their influence on ISM microphysics is the potential for CRs to launch galactic winds – an important feedback mechanism for regulating star formation efficiency – via momentum and heat transfer to the interstellar medium. The attractiveness of CRs as cause for these winds lies in the long cooling time scale (compared to the thermal gas) and the strong coupling to the ISM (via interactions with plasma waves and inelastic collisions with the gas), as discussed in the recent review Ruszkowski and Pfrommer (2023).

Cosmic rays are not only a key component of the interstellar medium, but they also cause radio synchrotron emission at much larger scales in the intracluster medium (ICM) of galaxy

clusters (e.g. van Weeren *et al.*, 2019). This radiation provides a direct observational proof that large-scale magnetic fields and a population of relativistic electrons, that loose energy via synchrotron radiation, exist within the ICM. These diffuse, non-thermal radio sources are divided into three groups, namely (1) radio halos with linear sizes of ~ 1 Mpc, whose morphology follows the gas distribution in the ICM, (2) radio relics (or cluster radio shocks), which are giant diffuse synchrotron sources powered by merger shocks during the hierarchical structure formation (mostly in cluster outskirts) and (3) sources of revived fossil plasma from active galactic nuclei (AGN), i.e. re-accelerated electrons from a supra-thermal, non-radiative seed population in the ICM, which are characterized by their ultra-steep radio spectra (due to losses) and often irregular morphologies.

Last but not least, there is another good reason why studying cosmic rays is a worthwhile endeavour: they are witnesses of the most extreme acceleration processes in the universe and can help deciphering the nature of those accelerators. Especially in the case of UHECRs there is still no comprehensive model (not to mention an observationally confirmed source) that can explain how it is possible that some natural processes can accelerate particles to energies three orders of magnitude above what can be reached at the largest man-made particle accelerator, the Large Hadron Collider (LHC) at CERN. Admittedly, jets arising from accretion disks around massive black holes are the favoured and most plausible model today, but there remain still many unsolved details. Even the origin of galactic cosmic rays, which seemed to be a closed case for many years thanks to the (much better understood) supernova paradigm, has given rise to a number of review articles in the last decade that pointed out the difficulties of this standard paradigm. We will touch upon this issue in section 1.4.

Hopefully, the outline above has convinced the reader that cosmic ray physics is an important cornerstone in tackling research questions on ISM dynamics, galaxy evolution and compact objects.

1.1 Comment on units and notation

Throughout this thesis it is attempted to use a coherent notation for various physical quantities that closely follows conventions in the contemporary scientific literature. In cases where one symbol is used for different quantities, subscripts are employed to avoid confusion. Some clarifications, a list of abbreviations and additional background information have been moved to the appendix.

One thing that might be awkward and lead to some confusion concerns the classification of supernovae. Roughly speaking, in this thesis we just distinguish between thermonuclear (Ia) and core-collapse (II, Ib, ...) supernovae, because the former expand in a uniform ambient medium, whereas the latter expand in the progenitor star's wind. However, the classification of supernovae is *not* based on the explosion mechanism, but on the detected spectrum. As a consequence, core-collapse supernovae encompass multiple spectral types, namely II, IIb, Ib, Ic, but all thermonuclear supernovae are of type Ia. Nevertheless, in the scientific literature the two main types of supernovae are sometimes distinguished by calling one type Ia (correct) and the other one type II (not correct, because there is a degeneracy). If in the later chapters of this thesis a distinction between type Ia and type II supernovae is made, then this actually refers to the explosion mechanism and not to the spectral type!

Another misunderstanding may arise from the imprecise usage of the term "supernova energy". The quantity of interest in this thesis is the kinetic energy of the ejected material, which is typically assumed to be 10^{44} J. The energy that goes into electromagnetic radiation is of the same order of magnitude and mainly caused by the decay of freshly synthesized radionuclides, which

powers the tail of the light curve. For core-collapse supernovae the most important decay chain is $^{56}\mathrm{Ni}(e^+\nu_e)\,^{56}\mathrm{Co}(e^+\nu_e)\,^{56}\mathrm{Fe}$, where the released positrons rapidly annihilate with surrounding electrons and produce γ-rays. However, in the case of a core-collapse supernova most of the stellar core's binding energy goes into neutrinos, namely 10^{46} J. Although we are solely interested in the kinetic energy of the ejecta, one should keep in mind that this is only $\sim 1\%$ of the neutrino energy!

Throughout this thesis SI units (Système international d'unités) are used. This is not only in accordance with virtually all other fields of physics and engineering, but also with the recommendations of the International Astronomical Union (IAU). Without any further comment I quote from chapter 5 of the IAU style manual[1]:

> "The international system (SI) of units, prefixes, and symbols should be used for all physical quantities except that certain special units, which are specified later, may be used in astronomy, without risk of confusion or ambiguity, in order to provide a better representation of the phenomena concerned. SI units are now used to a varying extent in all countries and disciplines, and this system is taught in almost all schools, colleges and universities. The units of the centimetre-gram-second (CGS) system and other non-SI units, which will be unfamiliar to most young scientists, should not be used even though they may be considered to have some advantages over SI units by some astronomers."

Equations containing electromagnetic quantities and whose appearance therefore depends on the choice of units can be translated into the outdated CGS system by using the following simple replacement rules for the electric charge q and the magnetic flux density B:

$$q_{\mathrm{CGS}} = \frac{q_{\mathrm{SI}}}{\sqrt{4\pi\varepsilon_0}}\,, \qquad B_{\mathrm{CGS}} = \sqrt{\frac{4\pi}{\mu_0}}B_{\mathrm{SI}}\,, \qquad \varepsilon_0\mu_0 = \frac{1}{c_{\mathrm{SI}}^2}\,.$$

Note that in the SI system there appear two natural constants, namely the vacuum electric permittivity ε_0 and the vacuum magnetic permeability μ_0. Together, they are not independent, because one can always be expressed through the other by including the speed of light or other natural constants, as shown below. The Committee on Data of the International Science Council (CODATA) recommends the following values (cf. Tiesinga *et al.*, 2021):

$$\varepsilon_0 = 8.854\,187\,812\,8(13)\cdot 10^{-12}\ \mathrm{F\,m^{-1}}\,, \tag{1.1}$$

$$\mu_0 = \frac{4\pi\alpha\hbar}{e^2 c} = 1.256\,637\,062\,12(19)\cdot 10^{-6}\ \mathrm{N\,A^{-2}}\,. \tag{1.2}$$

The last two digits in braces contain a measurement uncertainty. As usual, c is the speed of light in vacuum, e is the elementary charge, $\hbar$ is the reduced Planck constant and α is the fine-structure constant.

1.2 Overview over cosmic ray physics

The name "cosmic rays" is of purely historical origin, since after its discovery at the beginning of the 20th century it was believed that the ionizing radiation coming from outer space consists of high-energy photons (like X-rays or γ-rays). However, cosmic rays are particle radiation that

[1] see https://www.iau.org/static/publications/stylemanual1989.pdf

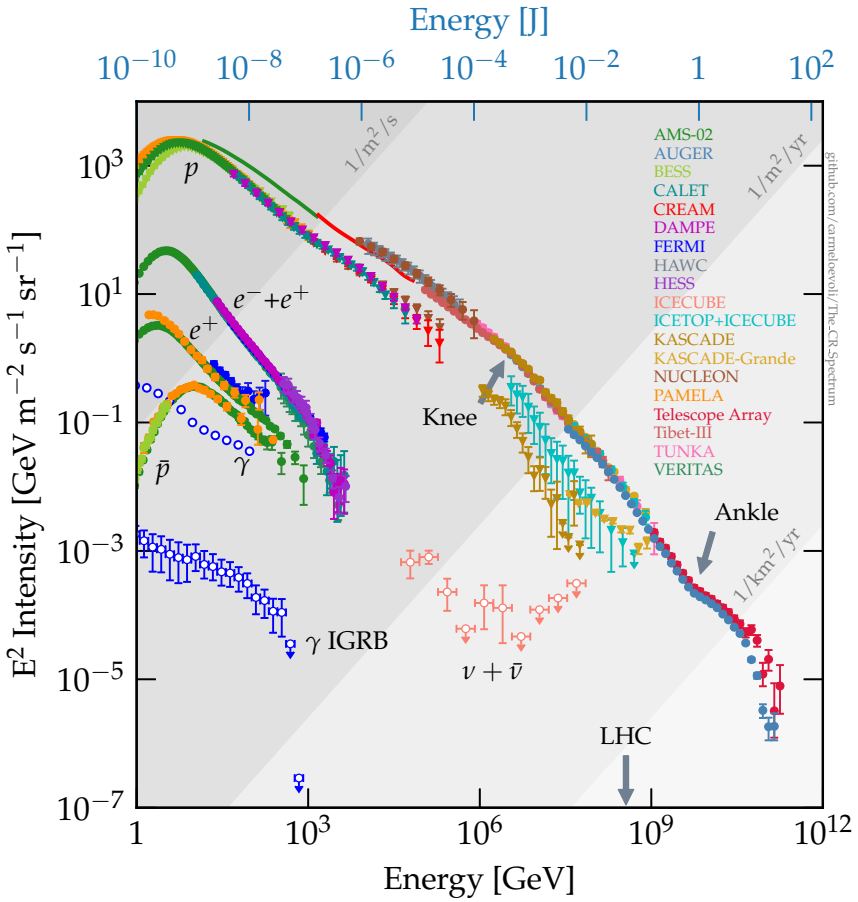

Figure 1.1: Collection of state-of-the-art measurement data from different experimental groups (for detailed references see Evoli, 2020). Note that the all-particle CR spectrum is an almost featureless power-law over several decades in energy! One also sees that the most energetic cosmic rays are beyond the capacities of the world's largest particle accelerator, the Large Hadron Collider (LHC). Note that the plot does not show the usually quoted centre-of-mass energy $\sqrt{s_{\rm pp}} = 14$ TeV, but the corresponding proton energy $E_{\rm p} \approx 1.0 \cdot 10^8$ GeV in the fixed-target frame.

primarily consists of atomic nuclei (99%) and a small number of energetic electrons (only 1%). The vast majority of nuclei are protons (90%) and α-particles (9%); the rest (1%) are heavier elements up to uranium. Note that even though electrons and protons are equally abundant in the universe, the CR electron-to-proton ratio is only $\sim 10^{-2}$. Indeed, if one assumes that both species have the same abundance and spectral slope, an elementary (though non-trivial) analysis leads to the conclusion that the spectra's normalization depends on the electron-to-proton mass ratio at relativistic particle energies (for a complete derivation see Schlickeiser, 2002, chap. 19.4).

A compilation of state-of-the-art measurements of the all-particle cosmic ray spectrum from various space- and ground-based experiments is shown in figure 1.1. One can see immediately, why the CR spectrum is sometimes called the "best power-law in nature". If intensity is plotted against particle energy in a simple log-log diagram, one would see an almost featureless power-law (a simple straight line) ranging over ten(!) decades in energy from ~ 10 GeV to $\sim 10^{11}$ GeV. In order to flatten certain parts of the spectrum and make small features better visible, the intensity is usually multiplied by some power of the energy (like E^2, $E^{2.3}$, E^3). In particular, the spectral energy distribution νF_ν is related to the differential energy flux via

$$\nu F_\nu \propto E^2 \frac{{\rm d}N}{{\rm d}E}\,, \tag{1.3}$$

where $N(E)$ is the number of CRs with energies above E, which is often suggestively written as $N(>E)$. The two main features arising from the spectrum are referred to as "knee" and "ankle" after an anatomic analogy. If we write the differential cosmic ray energy spectrum, which is proportional to the intensity, as $\mathrm{d}N(>E)/\mathrm{d}E \propto E^{-\tilde{q}}$, this can be quantified as follows: the knee marks a steepening of the spectral index from $\tilde{q} \approx 2.7$ to $\tilde{q} \approx 3.1$ at an energy of $E_{\mathrm{knee}} \approx 3 \cdot 10^6$ GeV = 3 PeV, whereas the ankle is a flattening back to $\tilde{q} \approx 2.7$ at $E_{\mathrm{ankle}} \approx 5 \cdot 10^9$ GeV (e.g. Thoudam *et al.*, 2016). Cosmic rays with energies larger than 10^9 GeV = 1 EeV, which is ten times more than what can be achieved with the world's largest particle accelerator LHC, are often referred to as ultra-high-energy cosmic rays (UHECRs) and believed to be of extragalactic origin. Before we discuss these features and their physical interpretation, a few comments on the lower and upper bound of the CR energy are in order.

An elementary particle is referred to as being relativistic when its kinetic energy exceeds its rest mass energy equivalent. Since protons and electrons have rest masses of 938.3 MeV/c^2 and 0.511 MeV/c^2, both of them would be considered relativistic if their kinetic energy exceeded 1 GeV. However, when the cosmic ray spectrum is measured, the energy range below a few GeV not accessible due to the strong influence of the Sun. On the one hand, a small fraction of cosmic rays directly comes from the Sun, where they are created in violent events in the solar atmosphere, like flares and magnetic reconnection. Consequently, the intensity of those particles follows the rapid variations in solar activity. On the other hand, the majority of cosmic rays is of galactic or extragalactic origin and anti-correlated to solar activity, because cosmic rays from outside the solar system with low energies are effectively shielded from the solar neighbourhood when the solar wind is strong. Therefore, the only way to measure those low-energy cosmic rays is to place a space satellite outside the heliosphere (so far, only the two Voyager probes have reached such a large distance from Earth). Although the investigation of low-energy non-solar cosmic rays suffers from severe practical limitations, they are by no means unimportant for the interstellar medium. Since the CR spectrum rapidly declines with increasing energy (typically as $\sim E^{-2}$), most of the heating and ionisation is provided by CRs with kinetic energies of ~ 100 MeV. Apart from that, cosmic rays with energies above ~ 10 GeV, that are not created by the Sun or influenced by solar activity, only show weak modulations over time.

Additionally, also the highest energy cosmic rays in the regime of $\sim 10^{20}$ eV are shielded from us (cf. Longair, 2011, chap. 15.12). However, the reason for this is not the Sun, but the cosmic microwave background radiation that fills the entire universe. If the energy of a cosmic ray particle is high enough, the CMB photons appear strongly blue-shifted in its rest frame. Hence, the production of new elementary particles becomes possible. For protons that are bombarded with γ-rays, one expects pion production for photon energies above 200 MeV via one of the following reactions:

$$\begin{aligned}
\gamma + p &\rightarrow \Delta^+ \rightarrow n + \pi^+ \,, \\
\gamma + p &\rightarrow \Delta^+ \rightarrow p + \pi^0 \,, \\
\gamma + p &\rightarrow \Delta^+ \rightarrow n + N\pi^+ \,.
\end{aligned}$$

Note that the delta baryon Δ^+ is a short-lived intermediate state that rapidly decays by creating a pion. The most frequent decay modes of the unstable reaction products are:

$$\begin{aligned}
n &\rightarrow p + e^- + \bar{\nu}_e \,, \\
\pi^+ &\rightarrow \mu^+ + \nu_\mu \,, \\
\mu^+ &\rightarrow e^+ + \nu_e + \bar{\nu}_\mu \,, \\
\pi^0 &\rightarrow 2\gamma \,.
\end{aligned}$$

We also note that the Bethe-Heitler pair production

$$p + \gamma \rightarrow p + e^- + e^+$$

is another important loss mechanism for ultra-high energy cosmic rays. Its cross section is larger than for the pion production, but the energy loss per produced electron-positron pair is much smaller. Although the proton is never effectively destroyed in any of these reactions (if a π^+ is produced, the free neutron will eventually decay back into a proton), it will loose a significant fraction of its kinetic energy over time. It is therefore expected that the mean free path of protons above 10^{20} eV is limited to a few Mpc. Since the highest energy cosmic rays are not produced within the Milky Way, but come from extragalactic sources, one expects the so-called Greisen-Zatsepin-Kuzmin (GZK) cut-off at the high-energy end of the CR spectrum. Indeed, the UHECRs show a pronounced steepening above $\sim 5 \cdot 10^{19}$ eV, which is compatible with a GZK cut-off, but could also be related to a maximum particle acceleration efficiency in astrophysical sources. Moreover, this conclusion even holds in the case that cosmic rays with the highest energies are composed of heavy nuclei instead of protons (this will only affect the cut-off energy). The reason is that the absorption of γ-rays with energies of a few 10 MeV (the typical binding energy per nucleon) excites one ore more nuclei, which are then ejected from the nucleus. This will then happen again to the shrunken nucleus, leading to its gradual disintegration.

The increasing quality of CR data has also revealed several minor features in the overall CR spectrum that can only be understood through a solid theoretical modelling of sources and of the CR propagation. We will not go into further detail here, but merely mention the common interpretation of the knee and the ankle. We first define the rigidity R of a nucleus with momentum p and charge number Z as $R \coloneqq pc/(Ze)$. It has units of voltage (energy per charge) and is defined such that the particle's Larmor radius can be written as $r_\mathrm{L} = p/(ZeB) = R/(Bc)$. This quantity is useful in high energy astrophysics, because many acceleration processes depend on the rigidity (a prototypical example is diffusive shock acceleration, which will be discussed in chapter 2). This can be illustrated by considering particle acceleration at the shock front of a supernova remnant as an example. The acceleration will definitely stop, if the particle's gyro-radius exceeds the remnant's size, because it cannot be confined any more.[2] This not only sets a simple upper limit to r_L, but also to R, because all particles experience the same local magnetic field, so B is constant. If the rigidity is fixed by the basic physics of the acceleration process, heavier nuclei can reach higher energies. If protons cannot be accelerated beyond $E_\mathrm{max,p} \approx 3 \cdot 10^{15}$ eV by any Milky Way source, then an iron nucleus can still be accelerated up to $E_\mathrm{max,Fe} = 26\, E_\mathrm{max,p} \approx 8 \cdot 10^{16}$ eV, where we made the safe assumption that nuclei at such high energies are fully ionized. The superposition of the cut-offs in the spectra of individual elements then naturally leads to a knee in the CR spectrum.

By contrast, the ankle is thought to be the transition from the galactic to the extra-galactic CR component. The main argument is that a proton with energy $\sim 10^{18}$ eV has a gyro-radius of 360 pc, which is comparable to the scale height of the Milky Way's (thin) disk (assuming a typical interstellar magnetic field of 0.3 nT). If one neglects some of the complexity of CR transport, this implies that protons with such high energies cannot be confined within the Milky Way. More specifically, CRs with energies below the ankle are expected to propagate diffusively within the Milky Way – as we will see later – meaning that they arrive at Earth from all directions and cannot be directly attributed to a source. By contrast, if there would exist an accelerator within our Galaxy that was able to generate UHECRs, they would propagate ballistically towards

[2] As we will see later, this criterion can be tightened by requiring that the diffusion length is only a fraction of the shock radius.

Earth so that an observer would see them coming from a specific region in the sky, namely where the source is located. However, no such astrophysical object exists within the Milky Way and the (approximate) isotropy of UHECRs suggest that their extragalactic sources are distributed isotropically over the entire sky. One of the big problems when investigating the arrival directions and composition of the highest energy CRs is the extremely low flux. In the cut-off region (at $\sim 5 \cdot 10^{19}$ eV) only one particle per square kilometre per century is detected, as indicated in figure 1.1. It is therefore not surprising why until today no conclusive data have been obtained that would connect the UHECR arrival directions to potential sources. However, number statistics improve over time.

1.3 Sources of cosmic rays

Any astrophysical accelerator that is energetic enough can in principal act as CR source. In the following we list a few examples (cf. Vink, 2020, chap. 11.1.5 and references therein):

- Supernova remnants: The strong, collisionless shock of the remnant with Mach number ~ 1000 allows particles to gain energy via diffusive shock acceleration (DSA), which will be discussed in chapter 2. As we will see in the next section, SNRs are the preferred sources for galactic cosmic rays, because they are frequent and energetic enough to maintain the observed energy density of CRs.

- Pulsar wind nebulae: Pulsars are fast rotating neutron stars with strong magnetic fields that emit periodic radio pulses (also observed in other wavelengths). This radiation results from various physical processes taking place in the so-called magnetosphere – a highly magnetized volume immediately surrounding the neutron star. Although the exact details of the radiation mechanism are not fully understood yet, it is clear that the strong and rapidly varying magnetic field induces an electric field powerful enough to remove charged particles (mainly protons and electrons) from the pulsar's surface. Once they are in the magnetosphere they will be accelerated to relativistic energies and their gyration along magnetic field lines will cause them to emit synchrotron radiation in the γ-ray-band. It is expected that the γ-photons are energetic enough to produce electron-positron pairs, which are again accelerated and emit their own γ-rays starting an electron-positron cascade. The particles attached to open field lines will eventually escape the pulsar and carry the "frozen-in" magnetic field with them, giving rise to the pulsar wind. Although rapidly spinning neutron stars have an enormous reservoir of rotational energy that could be tapped to produce cosmic rays, the composition of accelerated particles is expected to consist mainly of electrons and positrons (in equal amounts). Since the observed CR spectrum is dominated by atomic nuclei, pulsar wind nebulae cannot be the main sources of Galactic cosmic rays, although they might provide a significant fraction of the leptonic component.

- Winds from massive stars: The idea is that young star clusters that contain many massive, short-lived stars with strong, fast winds can act as CR factories. The energy is provided by interacting stellar winds, whereas the acceleration itself could take place either in the vicinity of the stars or in superbubbles; these are multi-parsec expanding cavities in dense molecular clouds caused by stellar winds and supernovae of massive stars. Since the stellar feedback is dominated by supernovae, superbubbles are not really an alternative source of cosmic rays, but instead an attractive environments for CR acceleration, because the powerful mechanically and magnetically turbulent flows allow cosmic rays to be efficiently scattered (longer confinement in bubble environment) and accelerated (through repeated

crossings of multiple SNR shocks or wind termination shocks). Since the acceleration efficiency is expected to be higher than for isolated supernovae, reaching energies of several PeV (above the knee) seems less challenging.

- Active galactic nuclei: The central engine of each AGN is a supermassive black hole at a galaxy's heart that accretes large amounts of matter from its surroundings. Several particle acceleration mechanisms have been proposed, all of which involve the relativistic jet perpendicular to the accretion disk. An example for this is the one-shot "espresso" acceleration process proposed by Caprioli (2015), which might be able to produce UHECRs. However, also the relativistic termination shock resulting from interactions of the jet with the ambient medium is expected to play a significant role.

- X-ray binaries: If the compact object in the binary sytem is a stellar-mass black hole with an accretion disk and a jet, then particles might be accelerated in similar way as in the case of an AGN, but of course on smaller spatial and energy scales. This gives rise to the term "micro-quasar".

- Tidal disruption events: A star passing by a black hole will be disrupted by the strong tidal forces if the impact parameter is small enough. The resulting transient AGN-like jets can be a potential source of UHECRs, for which a low injection rate is already sufficient, despite the rarity of such events (one in $\sim 30\,000$ yr within the Milky Way) and the short duration of UHECR production in a TDE jet (weeks or months).

Probably all of these sources contribute to the overall cosmic ray spectrum. However, when it comes to Galactic cosmic rays, supernovae are thought to be the main contributors. One reason is of course that sources, which are either very rare or extremely energetic, can be excluded a priori. In the following section we will discuss the main arguments in favour of supernova remnants.

1.4 The supernova paradigm

By now, the idea that supernova remnants are responsible for the vast majority of galactic cosmic rays (up to the knee) has been elevated to the rank of a paradigm – one could also call this ironically "standard folklore" (see the critical discussion in Drury, 2018). As we shall see, the oldest and still most convincing argument in favour of supernova remnants is also the simplest: It is almost impossible to think of any other plausible source for galactic cosmic rays that would release the required amount of energy to maintain the observed CR energy density.

1.4.1 Basic arguments

There are several very good arguments that support the standard paradigm on the origin of galactic cosmic rays, which are listed below (see e.g. Bykov *et al.*, 2018; Cristofari, 2021, and references therein):

1. By far the strongest argument is that supernova explosions are the only galactic sources with enough energy to sustain the measured cosmic ray energy density of ~ 0.5 MeV m^{-3}. This can be understood by the following, simplified back-of-the envelope estimation (this can be found in many textbooks and review articles, but here we mostly follow the pedagogical treatment of Longair, 2011, chap. 15.6): From the primary-to-secondary cosmic ray ratio one can estimate that a high-energy particle arriving at Earth has typically traversed

$\xi = 50$–$100\ \mathrm{kg\,m^{-2}}$ of matter on average (the so-called grammage). If we assume that the interstellar gas, which has a typical number density of $\langle n \rangle = 10^5$–$10^6\ \mathrm{m^{-3}}$, is solely composed of hydrogen and helium (neglecting all heavier elements), the mean molecular weight is given by

$$\langle m \rangle = \frac{n_\mathrm{H} m_\mathrm{p} + n_\mathrm{He} m_\mathrm{He}}{n_\mathrm{H} + n_\mathrm{He}} = \frac{n_\mathrm{H} + 4 n_\mathrm{He}}{n_\mathrm{H} + n_\mathrm{He}}\, m_\mathrm{p} = \frac{1 + 4 f_\mathrm{He}}{1 + f_\mathrm{He}}\, m_\mathrm{p}\,, \quad f_\mathrm{He} \coloneqq \frac{n_\mathrm{He}}{n_\mathrm{H}}\,. \tag{1.4}$$

For a helium abundance of $f_\mathrm{He} = 0.1$ one gets $\langle m \rangle \approx 1.3 m_\mathrm{p}$. All this information can then be used to estimate an escape time τ_esc via the simple relation

$$\xi = \langle \rho \rangle v \tau_\mathrm{esc} = \langle m \rangle \langle n \rangle c \tau_\mathrm{esc}\,. \tag{1.5}$$

By assuming that CRs propagate nearly with the speed of light, one finds $\tau_\mathrm{esc} \approx 2.4$–$49$ Myr. If CRs would travel ballistically along straight lines, this escape time would correspond to a path length of

$$\lambda = c \tau_\mathrm{esc} \approx 7.5 \cdot 10^2\text{–}1.5 \cdot 10^4\ \mathrm{kpc}\,, \tag{1.6}$$

which is far larger than the scale height of the galactic thin disc (~ 0.3 kpc) and even the thick disc (~ 1.5 kpc). This is the strongest argument why cosmic rays cannot propagate along straight lines through the Milky Way, like light rays (in weak gravitational fields), but have to show a diffusive behaviour instead. Much more could be said about the transport of cosmic rays in the galactic environment, but we will not further elaborate this issue here and merely note that a robust theoretical understanding of CR propagation is absolutely crucial for interpreting the observed CR data in the solar neighbourhood.

If one estimates the Milky Way's volume, in which cosmic rays can be confined for the duration τ_esc, by taking a cylinder with radius $r_\mathrm{d} = 15$ kpc and height $h = 2 \cdot 300$ pc, then the total cosmic ray energy that is lost per unit time is

$$L_\mathrm{CR} = \frac{E_\mathrm{CR}}{\tau_\mathrm{esc}} = \frac{u_\mathrm{CR}\, V}{\tau_\mathrm{esc}} = \frac{u_\mathrm{CR}\, \pi r_\mathrm{d}^2 h}{\tau_\mathrm{esc}} = 6.5 \cdot 10^{32}\text{–}1.3 \cdot 10^{34}\ \mathrm{W}\,. \tag{1.7}$$

Now comes the crucial point: The typical kinetic energy of the ejected material from a supernova explosion is roughly 10^{44} J. Since supernovae occur on average three times per century within the Milky Way, the corresponding power is

$$L_\mathrm{SN} \approx 9.5 \cdot 10^{33}\ \mathrm{W}\,. \tag{1.8}$$

Therefore, in order to sustain the cosmic ray power by supernovae alone, the fraction of the shock kinetic energy, which is used to accelerate particles from the thermal pool up to cosmic-ray energies, must lie in the range $\eta_\mathrm{SN} \approx 1\%$–$15\%$. More refined estimates around $\eta_\mathrm{SN} \approx 10\%$ are often quoted in the scientific literature, too. Admittedly, the required efficiency is rather high, but not unrealistically high. This argument is so powerful, because there are no real alternative sources in the Milky Way that could provide enough energy for cosmic ray acceleration. Indeed, most of the source candidates mentioned in the previous section are energetically less favourable than supernova remnants (see Vink, 2020, chap. 11.1.5 and references therein).

2. The source composition of the bulk of CR material is a mix of $\sim 80\%$ ISM material (with solar system abundances) and $\sim 20\%$ outflow from massive stars or ejecta from

SNe (including those elements preferentially locked in dust). This tells us that although supernovae provide the energy for acceleration, the accelerated nuclei stem mostly from the surrounding ISM (including old material from winds of low-mass stars) and not from the exploding star itself (freshly synthesized elements from supernova have different abundances compared to the ISM). SNRs are thought to be able to accelerate CRs until the end of the Sedov-Taylor phase, when the remnant's diameter has reached a size of ~ 100 pc, which is a significant fraction of the (thin disk) scale height. This implies that shocks from SNRs are indeed large enough to accelerate nuclei from a significant fraction of the galactic volume, which cannot be achieved by any other CR sources, since their filling factors are too small.

3. From observations of the non-thermal radiation coming from SNRs it is now well-established that in situ production of CRs indeed takes place. As will be briefly discussed in the next section, the main signatures are synchrotron emission emitted by ultra-relativistic electrons and gamma-rays from the decay of neutral pions that are produced by interactions between CR protons and the ambient medium.

4. In first approximation, the observed CR spectrum is a power-law in momentum, $f(p) \propto p^{-\alpha}$, with a slope $\alpha \approx 4.7$ (corresponding to a slope $\tilde{q} = 2.7$ in energy space) that is similar to the prediction $\alpha = 4$ of the first order Fermi acceleration mechanism at strong shocks. Note that spectral steepening during the diffusive propagation is also expected, as will be elaborated below. No other process naturally produces similar spectral shapes with the "correct" slope for electrons and protons.

5. Observations of the electron synchrotron emission in the X-ray band have established that the magnetic field in SNRs is amplified order-of-magnitudes above the typical ISM strength. This is absolutely necessary in order to accelerate protons to PeV energies, as we will show now. We first have to make some remarks on particle scattering by Alfvén waves, which leads to a diffusion barrier that keeps cosmic rays confined at the shock. The diffusion coefficient D can generally be expressed through the scattering mean free path λ_{mfp} and the average particle velocity $\langle v \rangle$ as

$$D = \frac{1}{3}\langle v \rangle \lambda_{\mathrm{mfp}} \quad \Longrightarrow \quad D_{\mathrm{B}} = \frac{1}{3} c r_{\mathrm{L}} = \frac{pc}{3eB} \approx \frac{E}{3eB} \,. \tag{1.9}$$

In the last step we introduced the Bohm diffusion coefficient D_{B}, which corresponds to a situation where particles propagate nearly with the speed of light and have a mean free path comparable to their Larmor radius; hence this is the minimum possible value for D. A criterion for the maximum particle energy can be formulated by demanding that the diffusion length $l_{\mathrm{diff}} = D/v_{\mathrm{sh}}$ must be smaller than a certain fraction χ of the shock radius (otherwise the particle could no longer be confined at the shock and would escape). This leads to

$$\frac{D_{\mathrm{B}}}{v_{\mathrm{sh}}} \leq \frac{D}{v_{\mathrm{sh}}} = l_{\mathrm{diff}} \overset{!}{<} \chi R_{\mathrm{sh}} \tag{1.10}$$

$$\Longrightarrow \quad E_{\mathrm{max}} < 3\chi e B R_{\mathrm{sh}} v_{\mathrm{sh}} \,. \tag{1.11}$$

By choosing $\chi = 0.1$ one finds that

$$E_{\mathrm{max}} \approx 9.3 \left(\frac{B}{\mathrm{nT}}\right)\left(\frac{v_{\mathrm{sh}}}{1000\ \mathrm{km\,s^{-1}}}\right)\left(\frac{R_{\mathrm{sh}}}{\mathrm{pc}}\right) \mathrm{TeV} \,. \tag{1.12}$$

Hence, without significant magnetic field amplifications PeV energies cannot be reached.

Although the energy argument alone indicates quite unambiguously that supernova remnants are *the* source of galactic cosmic rays, there are still some difficulties that will be discussed below:

1. Measurements of the carbon-to-boron ratio indicate that the CR spectrum injected into the ISM is steepened during the diffusive propagation towards Earth by $\propto E^{-0.3}$–$E^{-0.6}$. This is indeed expected, because all radiative loss processes (Bremsstrahlung, synchrotron and inverse Compton emission) become more efficient at higher particle energies. However, the steepening is not strong enough to reproduce the observed CR energy spectrum $\propto E^{-2.7}$. Hence, the source must inject a spectrum $\propto E^{-2.1}$–$E^{-2.4}$, which has a steeper slope than the predicted $\tilde{q} = 2$ from DSA. This will be further investigated in the next section, where the theoretical foundations of the test-particle approach to DSA are stated. In particular, non-linear effects will turn out to be crucial, which is however not surprising when keeping in mind that cosmic rays gain $\sim 10\%$ of the shock kinetic energy and can therefore modify the shock structure.

2. The isotopic ratio of $^{22}\mathrm{Ne}/^{20}\mathrm{Ne}$ in the CR spectrum is a factor ~ 5 larger than in the solar system. The favoured explanation for this abundance anomaly involves so-called Wolf-Rayet stars, which are capable of producing more of the neutron rich isotope ^{22}Ne than of ^{20}Ne. Wolf-Rayet stars are very massive and luminous stars in an evolutionary phase that is characterized by high mass-loss rates due to strong and fast stellar winds. In the hydrogen-burning zones all of the initial CNO nuclei are transformed into ^{14}N, which is then transformed in the helium-burning zone into ^{22}Ne through the reaction chain $^{14}\mathrm{N}(\alpha,\gamma)\,^{18}\mathrm{F}(e^{+}\nu_e)\,^{18}\mathrm{O}(\alpha,\gamma)\,^{22}\mathrm{Ne}$. Since stellar evolution models show that the helium burning zone is not connectively linked to the outer layers, enhanced amounts of ^{22}Ne can only appear at the surface if the outer hydrogen layers are removed (e.g. through a strong stellar wind), which is a characteristic feature of Wolf-Rayet stars. An in-depth discussion of the amount of ^{22}Ne enrichment in CR nuclei that can be attributed to Wolf-Rayet stars, together with arguments disfavouring other sources of ^{22}Ne, like nova outbursts and pulsating red giants, can be found in Casse and Paul (1982). Hence, one expects that the strong stellar winds and the final supernova explosions of these stars enrich their environment, which is most likely a super-bubble. Due to their short lifetimes, Wolf-Rayet stars will be the first members of the bubble's stellar population that explode and consequently enrich their neighbourhood with material that can later be processed by the shocks of subsequent supernovae. This shows how important it is to carefully distinguish between the source responsible for CR acceleration and the matter that is actually elevated from the thermal pool to high energies.

3. If supernovae are the main source of galactic cosmic rays, they have to accelerate protons at least up to the knee (a few PeV). In other words, they have to be pevatrons. In principle, the detection of γ-rays in the $\sim$ 100 TeV range would probe the acceleration of PeV CR protons. In practice, observations of all known SNR shells in the VHE domain have revealed cut-offs indicating that PeV CRs are not efficiently produced. There are, however, some strong candidates – for example, evidence for PeV protons in the SNR G106.3+2.7 is discussed in Fang *et al.* (2022).

1.4.2 Radiation signatures

In this subsection we briefly discuss the non-thermal radiation from (young) SNRs, because this is the strongest observational evidence that SNRs can accelerate particles to very high energies

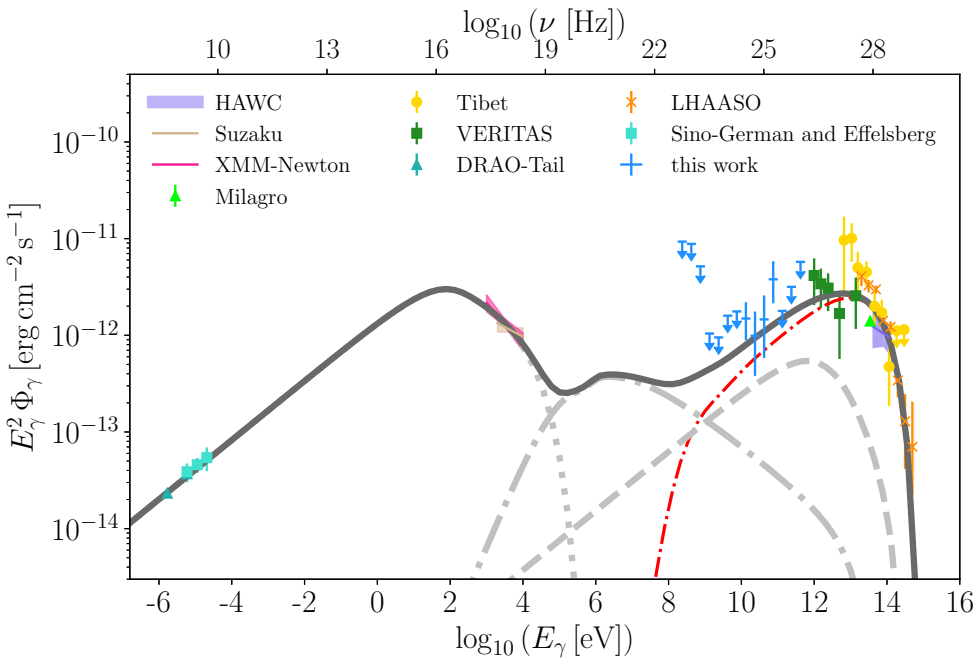

Figure 1.2: Broadband spectral energy distribution of supernova remnant G106.3+2.7 (see Fang *et al.*, 2022, and references therein). For the multi-wavelength data points coming from different experiments 95% upper limits or 1σ error bars are shown. The thick solid line represents the overall model spectrum; the contributions from electrons are shown in light-grey, whereas the proton contribution is shown in red. The injection spectra of both populations are assumed to be exponentially cut off power laws. The electrons produce radio to X-ray photons through synchrotron emission in a magnetic field (dotted curve; note the wide energy range!), hard X-ray to sub-GeV γ-ray through bremsstrahlung emission with gas in the interstellar medium (dash dotted curve), and γ-rays above 10 GeV through inverse Compton scattering of the CMB (dashed curve). The protons produce γ-rays through hadronic interaction with the surrounding gas (dash-dotted curve).

(for further details see Vink, 2020, chap. 12 and references therein). The different components of non-thermal radiation are nicely illustrated by the broadband spectral energy distribution of SNR G106.3+2.7, which is shown in figure 1.2 and was taken from Fang *et al.* (2022).

First of all, the gyration of high-energy charged particles in a magnetic field always leads to synchrotron emission, which ranges from the X-ray to the radio band in the case of SNRs. More specifically, the polarized radio synchrotron emission in the MHz–GHz frequency band extends over the remnant's whole volume and is produced by non-thermal relativistic electrons with energies of around a few GeV. On the other hand, the X-ray synchrotron emission is confined to thin filaments near the shock and comes from electrons with tens of TeV gyrating in an amplified magnetic field (far above typical ISM values) immediately behind the shock front.

Apart from that, SNRs also emit γ-rays with energies above 1 GeV. There is one hadronic channel for γ-ray production and two leptonic ones. The former consists of cosmic ray protons that produce neutral pions through energetic collisions with hydrogen nuclei in the ambient medium, which then decay into γ-rays. The leptonic channel consists of (1) bremsstrahlung emitted by high-energy electrons that are decelerated when interacting with protons in the ambient gas and (2) inverse Compton scattering between CR electrons and photons from the interstellar radiation field (including the CMB). These processes can be summarized as follows:

$$\text{pion production:} \qquad \mathrm{CRp} + p \rightarrow p + p + \text{pions}\,, \quad \pi^0 \rightarrow 2\gamma\,, \tag{1.13}$$

$$\text{bremsstrahlung:} \qquad \mathrm{CRe} + p \rightarrow e + p + \gamma\,, \tag{1.14}$$

$$\text{inverse Compton scattering:} \qquad \mathrm{CRe} + \gamma_{\mathrm{ISRF}} \rightarrow e + \gamma\,. \tag{1.15}$$

The lightest pion π^0 has a rest mass of $m_{\pi^0} = 134.98\ \mathrm{MeV/c^2}$. So if a CR proton hits a thermal proton at rest (corresponding to the fixed-target frame), it must have a minimum kinetic energy of $\sim$280 MeV in order to produce a neutral pion (cf. Vink, 2020, chap. 13.6.2). The two γ-rays from the pion decay each have an energy of $m_{\pi^0}c^2/2$ in the pion's rest frame, which gives rise to the so-called "pion bump" in the observed γ-ray spectrum.

2 Particle acceleration at collisionless shocks

In this chapter particle acceleration at shocks is discussed. In particular, it is shown that the standard theory of diffusive shock acceleration, which treats cosmic rays as simple test particles, naturally leads to a distribution function that can be described as a power-law in momentum space. Additionally, there are a number of non-linear effects, like the back-reaction of cosmic rays on the shock structure or self-induced magnetic field amplification via plasma instabilities, whose influence on the CR spectrum is discussed. This serves as a theoretical motivation for one of the most crucial ingredients of our CR model – the distribution function at the shock front of the supernova remnant.

2.1 A brief historical overview

Although the original idea of particle acceleration by reflection at "magnetic mirrors" was already developed in the late 1940s by Enrico Fermi (see Fermi, 1949, 1954), the simplest version of the theory, namely steady diffusive acceleration of test particles at a one-dimensional parallel shock, was not worked out until the late 1970s, when it was published in four independent papers. Essentially it was shown that repeated crossing of the shock front by cosmic rays in combination with diffusive scattering at plasma waves leads to a momentum spectrum following a power-law, where the slope only depends on the shock compression ratio. This central result was demonstrated by using two different approaches, namely a macroscopic one, that is based on the transport equation for the distribution function, and a microscopic one, that focuses more one the physics behind diffusive shock acceleration and systematically investigates what happens to a test particle during the acceleration process. The former approach was independently discussed in the following three papers:

- Axford *et al.* (1977): This is the earliest of the four papers and was published in the "Proceedings of the 15th international Cosmic Ray Conference".
- Krymskii (1977): Although this two-page article (in Russian) appeared 5 months later, it was the first to be published in the peer-reviewed literature.
- Blandford and Ostriker (1978): This article is also rather brief (3 pages) and already cites the paper by Axford, Leer & Skadron.

On the other hand, the microscopic approach to DSA was worked out by Anthony R. Bell in a series of two papers:

- Bell (1978a): The microphysics behind diffusive shock acceleration is discussed.
- Bell (1978b): Discussion of other aspects concerning DSA, like injection into the acceleration process, treatment of non-relativistic particles and estimates for the resulting synchrotron emission.

2.2 Elementary considerations

Before we have a quantitative look at the test-particle theory of diffusive shock acceleration, we follow a quick back-of-the-envelope calculation in Longair (2011, chap. 7.4), which illustrates the basic ideas of Fermi acceleration. Let us assume that the energy gain ΔE in one acceleration cycle is proportional to the particle's momentary energy E_0, i.e. $\Delta E = E - E_0 = \beta E_0$, and that the particle stops participating in the next acceleration cycle with a constant "escape probability" P_{esc}, which does not depend on energy. As will be shown later, these ad-hoc presuppositions are direct consequences of the underlying assumption that the particle transport is diffusive, even though details of the scattering process never enter the calculation. If all particles start with the same initial energy E_0, then after k cycles there are $N = N_0(1 - P_{\mathrm{esc}})^k$ particles left in the acceleration region and each of them has an energy of at least $E = E_0(1 + \beta)^k$, because some will be accelerated to even higher energies in subsequent cycles. Therefore it is suggestive to write this cumulative number as $N(> E)$. The auxiliary number k can be eliminated by taking the logarithm of both equations and dividing them:

$$\frac{\ln(N/N_0)}{\ln(E/E_0)} = \frac{k\,\ln(1 - P_{\mathrm{esc}})}{k\,\ln(1+\beta)} = \frac{\ln(1 - P_{\mathrm{esc}})}{\ln(1+\beta)} \tag{2.1}$$

$$\Longrightarrow \quad \frac{N(> E)}{N_0} = \left(\frac{E}{E_0}\right)^{\ln(1-P_{\mathrm{esc}})/\ln(1+\beta)} \tag{2.2}$$

$$\Longrightarrow \quad \frac{\mathrm{d}N(> E)}{\mathrm{d}E} \propto E^{-\alpha}\,. \tag{2.3}$$

In the last step, we converted the cumulative particle number $N(> E)$ into the differential energy spectrum. Note that the power-law exponent $\alpha \coloneqq 1 - \ln(1 - P_{\mathrm{esc}})/\ln(1+\beta)$ only depends on the two constants P_{esc} and β. As we will see, α can solely be expressed in terms of the shock compression ratio $\sigma = \rho_2/\rho_1$ via $\alpha = (\sigma + 2)/(\sigma - 1)$, which is quite remarkable.

The quantitative derivations in the following two sections are by now quite well-known and can be found in many review articles (e.g. Bell, 2013; Blandford and Eichler, 1987; Jones, 1994; Jones and Ellison, 1991; Urošević *et al.*, 2019) or textbooks (e.g. Padmanabhan, 2001, chap. 4.10; Thorne and Blandford, 2017, chap. 23.6). The following presentation (with some supplements from the aforementioned literature) is mainly based on the review Drury (1983), which also contains more references to the original literature and early papers that implicitly touch upon variants of diffusive shock acceleration. Some additional background on the distribution function in kinetic theory and its moments can be found in appendix C.

2.3 Macroscopic approach

At first, we present a brief summary of what is called the "macroscopic approach to DSA", meaning that the theoretical derivation of the resulting cosmic ray spectrum is based on the transport equation for the CR distribution function, which is a macroscopic description. We consider the shock to be an infinite planar discontinuity in the y-z-plane and choose an inertial frame, where the shock front is at rest at $x = 0$. In this reference frame the fluid streams parallel to the x-axis, which makes the problem effectively one-dimensional. The velocity field of the fluid is then given by $u(x)\hat{\mathbf{e}}_x$, where we assume that $u(x)$ is piecewise constant (stationary), so

$$u(x) = \begin{cases} u_1 & \text{for } x < 0\,, \\ u_2 & \text{for } x > 0\,. \end{cases} \tag{2.4}$$

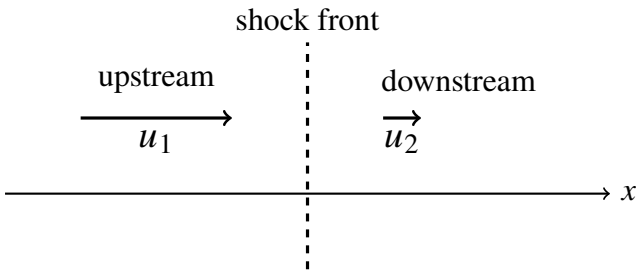

Figure 2.1: Simplified shock geometry that is assumed in the test-particle theory of diffusive shock acceleration. In this reference frame the shock front (an infinite plane) is at rest at $x = 0$. The fluid streams in from the upstream region ($x < 0$) and exits into the downstream region ($x > 0$).

where u_1 is the upstream velocity and u_2 is the downstream velocity. Normally, one would write the distribution function $f(\mathbf{x}, \mathbf{p}, t)$ as a function of position $\mathbf{x}$ and $\mathbf{p}$ as measured in the reference frame in which the shock is stationary and the plasma is moving. However, it is more convenient to measure the momentum in the local fluid rest frame (denoted by $\tilde{\mathbf{p}}$), because then the distribution is isotropic, i.e. it can be written as $f(\mathbf{x}, \tilde{p}, t)$, where $\tilde{p} \coloneqq |\tilde{\mathbf{p}}|$. The general transport equation for the distribution function can be derived from the relativistic Vlasov equation, which expresses particle number conservation in phase space, and has the form

$$\frac{\partial f}{\partial t} + u\frac{\partial f}{\partial x} = \frac{\tilde{p}}{3}\frac{\partial u}{\partial x}\frac{\partial f}{\partial \tilde{p}} + \frac{\partial}{\partial x}\left(D(x,\tilde{p})\frac{\partial f}{\partial x}\right) + Q(x,\tilde{p})\,, \tag{2.5}$$

which is shown in Blandford and Eichler (1987). Here, $D(x, \tilde{p})$ is the spatial diffusion coefficient along the magnetic field lines, i.e. perpendicular to the shock front. If we assume that the distribution function is stationary, neglect the source term $Q(x, \tilde{p})$ and use expression (2.4) for the fluid velocity, the transport equation simplifies to

$$\frac{\partial (fu)}{\partial x} = u\frac{\partial f}{\partial x} = \frac{\partial}{\partial x}\left(D(x,\tilde{p})\frac{\partial f}{\partial x}\right). \tag{2.6}$$

If one integrates this equation over one side of the shock from 0 to x (so that $u(x)$ remains constant), one finds

$$f(x,\tilde{p})u = D(x,\tilde{p})\frac{\partial f(x,\tilde{p})}{\partial x} + \tilde{A}(\tilde{p}) \tag{2.7}$$

$$\Longrightarrow \quad \frac{\partial f(x,\tilde{p})}{\partial x} = \frac{u}{D(x,\tilde{p})} f(x,\tilde{p}) - \tilde{A}(\tilde{p})\,, \tag{2.8}$$

where $\tilde{A}(\tilde{p})$ is an arbitrary function that only depends on momentum. By introducing $A(\tilde{p}) \coloneqq \tilde{A}(\tilde{p})/u$, which again is independent of x for our chosen domain of integration, we can rewrite this as

$$\frac{\partial}{\partial x}(f(x,\tilde{p}) - A(\tilde{p})) = \frac{\partial f(x,\tilde{p})}{\partial x} = \frac{u}{D(x,\tilde{p})}(f(x,\tilde{p}) - A(\tilde{p}))\,. \tag{2.9}$$

This first-order, homogeneous ordinary differential equation in x has the standard solution

$$f(x,\tilde{p}) = A(\tilde{p}) + B(\tilde{p})\,\exp\left(\int_0^x \frac{u}{D(x,\tilde{p})}\,\mathrm{d}x\right). \tag{2.10}$$

We now have a look at the solution in the upstream region $x < 0$ and note that for $x \to -\infty$ the exponent goes to zero, since both u_1 and $D(x, \tilde{p})$ are positive and bounded. More precisely, in the following we assume that

$$\lim_{x \to \pm\infty} \int_0^x \frac{1}{D(x, \tilde{p})} \, \mathrm{d}x = \pm\infty \,. \tag{2.11}$$

With this assumption we can determine the unknown functions $A(\tilde{p})$ and $B(\tilde{p})$ from the boundary conditions. By evaluating the solution (2.10) at $x = -\infty$, one finds

$$A(\tilde{p}) = f(x = -\infty, \tilde{p}) =: f_-(\tilde{p}) \,. \tag{2.12}$$

Similarly, evaluating the solution at $x = 0$ yields

$$B(\tilde{p}) = f(x = 0, \tilde{p}) - f(x = -\infty, \tilde{p}) =: f_0(\tilde{p}) - f_-(\tilde{p}) \,. \tag{2.13}$$

In conclusion, the upstream distribution function is given by

$$f(x, \tilde{p}) = f_-(\tilde{p}) + (f_0(\tilde{p}) - f_-(\tilde{p})) \, \exp\left(- \int_x^0 \frac{u_1}{D(x', \tilde{p})} \, \mathrm{d}x' \right) \quad \text{at } x < 0 \,. \tag{2.14}$$

Similarly, the downstream solution can be found. However, from (2.11) we immediately see that $f(x, \tilde{p})$ would grow without bounds if $B(\tilde{p})$ would not vanish, which implies that $f(x, \tilde{p}) = C(\tilde{p})$ for $x > 0$, where $C(\tilde{p})$ is again an arbitrary function that solely depends on momentum. An important thing to note is that $f(x, \tilde{p})$ is continuous across the shock front $x = 0$, because the parallel magnetic field has no discontinuity, so the cosmic rays unaffectedly continue their helical paths after crossing the shock front. Only the choice

$$f(x, \tilde{p}) = C(\tilde{p}) = f_0(\tilde{p}) \quad \text{at } x > 0 \tag{2.15}$$

joins the two solutions.

The particle flux, as measured in the shock's frame, is given by

$$F(x, \tilde{p}) = -D \frac{\partial f}{\partial x} - u \frac{\tilde{p}}{3} \, , \frac{\partial f}{\partial \tilde{p}} \, , \tag{2.16}$$

where the first term represents the diffusive flux and the second term arises, because we use the momentum in the fluid rest frame, but the position in the shock rest frame. Now we calculate the fluxes upstream and downstream, which are then both evaluated at the shock position $x = 0$:

$$F_-(x, \tilde{p})\Big|_{x=0} = (-f_0(\tilde{p}) + f_-(\tilde{p})) \, u_1 - u_1 \frac{\tilde{p}}{3} \frac{\partial f_0(\tilde{p})}{\partial \tilde{p}} \, , \tag{2.17}$$

$$F_+(x, \tilde{p})\Big|_{x=0} = -u_2 \frac{\tilde{p}}{3} \frac{\partial f_0(\tilde{p})}{\partial \tilde{p}} = -\frac{u_1}{\sigma} \frac{\tilde{p}}{3} \frac{\partial f_0(\tilde{p})}{\partial \tilde{p}} \, . \tag{2.18}$$

Here we wrote the downstream velocity in terms of the compression ratio $\sigma = u_1/u_2$. By setting both expressions equal, corresponding to a continuous flux across the shock, we obtain a differential equation for $f_0(\tilde{p})$:

$$F_-(x, \tilde{p})\Big|_{x=0} \stackrel{!}{=} F_+(x, \tilde{p})\Big|_{x=0} \quad \Longleftrightarrow \quad \tilde{p} \frac{\partial f_0(\tilde{p})}{\partial \tilde{p}} = \frac{3\sigma}{\sigma - 1} (f_-(\tilde{p}) - f_0(\tilde{p})) \, . \tag{2.19}$$

The solution of this standard first-order ordinary differential equation is the sum of the homogeneous solution and a particular solution of the inhomogeneous equation:

$$f_+(\tilde{p}) = f_0(\tilde{p}) = f_0(\tilde{p}_0)\tilde{p}^{-\alpha} + \alpha\tilde{p}^{-\alpha}\int_{\tilde{p}_0}^{\tilde{p}} \tilde{p}'^{\alpha-1} f_-(\tilde{p}')\,\mathrm{d}\tilde{p}' \;, \quad \alpha := \frac{3\sigma}{\sigma-1}\,, \tag{2.20}$$

where we defined the slope $\alpha := 3\sigma/(\sigma-1)$. This result deserves some further discussion. In some references, the homogenous term in the solution is completely ignored without real justification. From a mathematical point of view, this is untenable, but from a physical perspective one can argue that the homogenous term resembles a source term, which is problematic, because in our above derivation no particles are created.[1] In fact, the only source for the downstream distribution $f_+(\tilde{p})$ is the spectrum $f_-(\tilde{p})$ that was advected into the shock from upstream, which is exactly represented by the second term. It can be understood more clearly by assuming that the upstream distribution function is a power-law of the form $f_-(\tilde{p}) \propto \tilde{p}^{-\alpha+\delta}$. Then the second term can be integrated analytically, yielding

$$\alpha\tilde{p}^{-\alpha}\int_{\tilde{p}_0}^{\tilde{p}} \tilde{p}'^{\alpha-1} f_-(\tilde{p}')\,\mathrm{d}\tilde{p}' \propto \alpha\tilde{p}^{-\alpha}\int_{\tilde{p}_0}^{\tilde{p}} \tilde{p}'^{\alpha-1}\,\tilde{p}'^{-\alpha+\delta}\,\mathrm{d}\tilde{p}' \tag{2.21}$$

$$= \frac{\alpha}{\delta}\tilde{p}^{-\alpha}\left(\tilde{p}^{\delta} - \tilde{p}_0^{\delta}\right). \tag{2.22}$$

Now, if the distribution function far upstream is steeper than $\tilde{p}^{-\alpha}$, meaning that $\delta < 0$, the second term in the parenthesis of equation (2.22) will be dominant and the downstream spectrum will be proportional to $\tilde{p}^{-\alpha}$. In the opposite case, when $\delta > 0$ and therefore $f_-(\tilde{p})$ is flatter than $\tilde{p}^{-\alpha}$, the resulting CR distribution far downstream will also be flattened and proportional to $\tilde{p}^{-\alpha+\delta}$. Since the gas at $x = -\infty$ can be considered as ambient medium that has not been shocked yet, one can safely assume that its distribution function is thermal, i.e. a exponentially suppressed Maxwell-Boltzmann distribution, that is steeper than any power law. Consequently, we expect that the CR spectrum far downstream is the simple power law $f_+(\tilde{p}) \propto \tilde{p}^{-\alpha}$.

It is remarkable, that the spectral slope α does not dependent on the details of the diffusion coefficient $D(x, \tilde{p})$, but solely on the compression ratio σ. For strong shocks in a non-relativistic monatomic gas with adiabatic index $\gamma_{\mathrm{ad}} = 5/3$ we have $\sigma = 4$ as a consequence of the Rankine-Hugoniot jump conditions for hydrodynamical shocks and thus $\alpha = 4$. For relativistic particle energies the distribution function $f(p) \propto p^{-4}$ corresponds to an energy spectrum $f(E) \propto E^{-2}$ (see equation (C.17) in appendix C), is in good (but not exact) agreement with the slope of CRs arriving at Earth.

Last but not least, we note that this standard result can also be obtained in an alternative way, when the injection term in the transport equation is not neglected, but modelled as $Q(x, \tilde{p}) \propto \delta_{\mathrm{D}}(x)\,\delta_{\mathrm{D}}(\tilde{p} - \tilde{p}_{\mathrm{inj}})$, where the Dirac delta distribution is denoted by δ_{D}. So the underlying assumption is that only particles with a certain momentum $\tilde{p}_{\mathrm{inj}}$ are injected at the shock front $x = 0$ (for details see Blasi, 2013, sec. 3.3).

[1] In Drury (1983) the homogenous term is interpreted as injection of thermal particles from the background plasma into the acceleration process. This viewpoint is criticized in Jones and Ellison (1991), because there is no energy cut-off for the homogenous term, so it cannot be normalized. Additionally, Monte Carlo calculations suggest that thermal leakage injection should not be treated differently than any other injection process. Since Jones' arguments seem to be more stringent, we will also adopt this viewpoint in the remaining section.

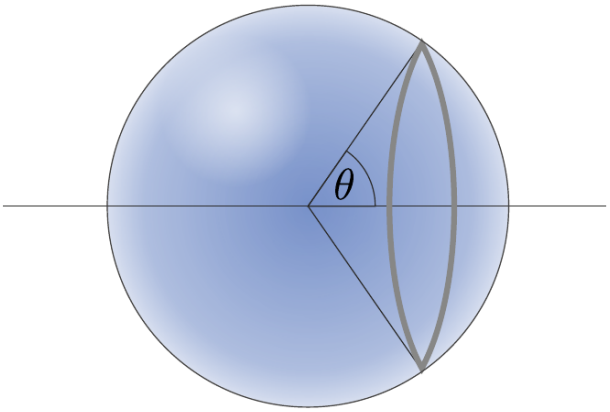

Figure 2.2: The probability that a randomly oriented (unit) vector has an angle in the range $[\theta, \theta + \Delta\theta]$ with respect to a fixed axis (horizontal line) is proportional to the thin grey area on the surface of the sphere, which is given by circumference × thickness = $2\pi \sin(\theta)\Delta\theta$. This sketch was kindly provided by Julian Sommer.

2.4 Microscopic approach

In this approach we will follow the motion of a test-particle across the shock front and calculate the average momentum gain during each acceleration cycle. In this section the distribution function is not used directly any more, but instead the particle density $n(x,t)$, which is simply $f(x,p,t)$ integrated over momentum space (see appendix C). Again, the configuration is essentially one-dimensional. We already know from our elementary analysis of the stationary transport equation that for any physical solution the downstream density has to be constant and identical to the density at the shock front, which is denoted by $n_0(p) \coloneqq n(x = 0, p)$. Consequently, the downstream flux, that tries to advect the particles away from the shock front, is given by $F_{\mathrm{adv}}(p) = n_0(p)u_2$. At the beginning of each acceleration cycle the test particle crosses the shock front from upstream to downstream, which is an inevitable consequence of the coupling to the plasma's motion. The question then is whether the particle can re-cross the shock front and get back to the upstream side or whether it gets advected so far downstream that it will never again return to the shock again, meaning that the acceleration process is terminated. This question can be answered by considering the particle flux from downstream to upstream. By our fundamental assumption of rapid momentum isotropisation, in the rest frame of the downstream fluid one half of the test particles moves to the left and the other half moves to the right. Additionally, we make the simplifying assumption that all particles have the same relativistic speed $v \approx c$, so that their velocities only differ in orientation, but not in magnitude. Therefore, the particle flux averaged over all angles is

$$F_{\mathrm{cross}} = \int_0^{2\pi} \mathrm{d}\varphi \int_0^{\pi/2} \mathrm{d}\theta \, \frac{1}{2} n_0 v \cos(\theta) P(\theta, \varphi) \, . \tag{2.23}$$

As usual, φ is the azimuthal angle and θ is the angle between the particle's velocity and the shock normal (i.e. the unit vector $\hat{\mathbf{e}}_x$), hence $v\cos(\theta)$ is the velocity projected onto the x-axis. Since the geometry of our problem is azimuthally symmetric, the probability $P(\theta, \varphi)$ that the particle's velocity vector points in the direction specified by the two angles, can only depend on θ. By a simple geometric argument (see figure 2.2) one can show that $P(\theta, \varphi) = K \sin(\theta)$. The constant K can easily be determined from the condition that any probability density function must be

normalized to one, so

$$1 \stackrel{!}{=} \int_0^{2\pi} \mathrm{d}\varphi \int_0^{\pi/2} \mathrm{d}\theta\, P(\theta,\varphi) = 2\pi K \int_0^{\pi/2} \mathrm{d}\theta \sin(\theta) = 2\pi K \quad \Longrightarrow \quad K = \frac{1}{2\pi}\,. \tag{2.24}$$

As expected, the correct normalization cancels with the factor 2π from the trivial angular integration over φ. By taking this into account and using the common variable substitution $\mu \coloneqq \cos(\theta)$, the flux of particles re-crossing the shock front is given by

$$F_{\mathrm{cross}} = \int_0^{\pi/2} \frac{1}{2} n_0 v \cos(\theta)\sin(\theta)\,\mathrm{d}\theta = \int_0^1 \frac{1}{2} n_0 v \mu\,\mathrm{d}\mu = \frac{1}{4} n_0 v\,. \tag{2.25}$$

This is an important result, because the ratio of the two fluxes yields the probability that the test particle is advected far downstream and never returns to the shock front again:

$$P = \frac{F_{\mathrm{adv}}}{F_{\mathrm{cross}}} = \frac{u_2 n_0}{v n_0/4} = \frac{4u_2}{v}\,. \tag{2.26}$$

We also emphasize that in this derivation we do not allow that particles escape towards upstream infinity, meaning that once a particle has made it to the upstream side again, it will eventually be advected downstream with 100% probability. Conversely, a particle in the downstream fluid recrosses the shock front only with a finite probability $P = 1 - 4u_2/v$.

If a particle has momentum p and pitch angle μ in the rest frame of the upstream fluid, then it sees the shock approaching with velocity $v_{\mathrm{sh}} = u_1$ from the right to left. Hence, the particle's energy in the (primed) shock frame can be calculated by performing a Lorentz boost along the relative velocity $u_1\hat{\mathbf{e}}_x$ between the two frames:

$$\frac{E'}{c} = \gamma_{u_1}\left(\frac{E}{c} + \frac{u_1 p_x}{c}\right) = \gamma_{u_1}\left(\frac{E}{c} + \frac{u_1 p\cos(\theta)}{c}\right) \tag{2.27}$$

$$\Longrightarrow \quad p' \approx p + \frac{u_1 p\cos(\theta)}{c}\,. \tag{2.28}$$

In the last step we used that the shock is non-relativistic, i.e. $u_1 \ll c$ and therefore $\gamma_{u_1} \approx 1$, but the test particle is already (mildly) relativistic, i.e. $E \approx pc$ and $E' \approx p'c$. Similarly, the upstream particle momentum p can be expressed in the rest frame of the downstream fluid by performing a Lorentz boost along the relative velocity $(u_1 - u_2)\mathbf{e}_x$:

$$p' \approx p + \frac{(u_1-u_2)p\cos(\theta)}{c} \quad \Longleftrightarrow \quad \Delta p \approx \frac{(u_1-u_2)p\cos(\theta)}{c}\,. \tag{2.29}$$

In the last step we introduced the momentum change Δp that a particle experiences when it crosses the shock front from upstream to downstream. Thus the flux-averaged change in momentum is

$$\langle \Delta p\rangle = \frac{\int_0^1 \Delta p(\mu)\,\frac{n_0 v}{2}\mu\,\mathrm{d}\mu}{\int_0^1 \frac{n_0 v}{2}\mu\,\mathrm{d}\mu} = \frac{\int_0^1 \Delta p(\mu)\,\mu\,\mathrm{d}\mu}{\int_0^1 \mu\,\mathrm{d}\mu} = \frac{(u_1-u_2)p}{c}\,\frac{\int_0^1 \mu^2\,\mathrm{d}\mu}{\int_0^1 \mu\,\mathrm{d}\mu} \tag{2.30}$$

$$= \frac{(u_1-u_2)p}{c}\,\frac{1/3}{1/2} = \frac{2(u_1-u_2)p}{3c}\,. \tag{2.31}$$

The same can be repeated analogously for the opposite case when a particle crosses the shock from downstream to upstream. There are only two differences, namely that the relative velocity

changes sign and is then given by $u_2 - u_1$, but so does the angle μ, which then runs from $\mu = -1$ to $\mu = 0$. Therefore, the total flux-averaged momentum gain during one acceleration cycle, i.e. one forward and one reverse crossing of the shock front, is given by

$$\langle \Delta p \rangle = \frac{4(u_1 - u_2)p}{3c} \,. \tag{2.32}$$

If we use p_n to denote the momentum of a particle that returns from downstream k times (and has therefore crossed the shock $2k$ times), then for large k and $v \gg u_1$ it can be recursively written as

$$p_k = p_k - p_{k-1} + p_{k-1} \approx \langle \Delta p \rangle + p_{k-1} = \left(\frac{4(u_1 - u_2)}{3c} + 1 \right) p_{k-1} \tag{2.33}$$

$$= \left(\frac{4(u_1 - u_2)}{3c} + 1 \right)^2 p_{k-2} = \ldots = \left(\frac{4(u_1 - u_2)}{3c} + 1 \right)^k p_0 \,. \tag{2.34}$$

By taking the logarithm on both sides and using $(u_1 - u_2)/c \ll 1$, we obtain an explicit expression for k:

$$k = \ln\left(\frac{p_k}{p_0}\right) \ln\left(\frac{4(u_1 - u_2)}{3c} + 1 \right)^{-1} \approx \ln\left(\frac{p_k}{p_0}\right) \left(\frac{4(u_1 - u_2)}{3c} \right)^{-1} . \tag{2.35}$$

From our above considerations we infer that the probability P_k of the particle reaching at least momentum p_k, i.e. of returning at least k times from downstream or equivalently not being advected for k acceleration cycles, is

$$P_k = \prod_{j=1}^{k} \left(1 - \frac{4u_2}{v_j} \right) \approx \prod_{j=1}^{k} \left(1 - \frac{4u_2}{c} \right) = \left(1 - \frac{4u_2}{c} \right)^k , \tag{2.36}$$

where we assumed that the particle velocity v_j in every cycle is already close to the speed of light.

We can now eliminate k from the above expressions by taking the logarithm:

$$\ln(P_k) = k \ln\left(1 - \frac{4u_2}{c} \right) \approx -k \, \frac{4u_2}{c} = -\ln\left(\frac{p_k}{p_0}\right) \frac{3c}{4(u_1 - u_2)} \, \frac{4u_2}{c} = -\ln\left(\frac{p_k}{p_0}\right) \frac{3u_2}{u_1 - u_2} \tag{2.37}$$

$$\implies \quad P_k = \left(\frac{p_k}{p_0}\right)^{-3u_2/(u_1 - u_2)} = \left(\frac{p_k}{p_0}\right)^{-3/(\sigma - 1)} . \tag{2.38}$$

It is now convenient to define the integral spectrum $N(x, p)$ as the number density of particles that have been accelerated at least to a momentum p (or higher):

$$N(x, p) \coloneqq \int_p^\infty 4\pi p'^2 f(x, p') \, \mathrm{d}p' \,. \tag{2.39}$$

Note that we already encountered this quantity, but expressed in energy space, in section 2.2. For simplicity, we assume that all particles, which are initially advected from the upstream side, have a distribution function that is peaked around a certain momentum p_0,

$$f_-(p) = f(x = -\infty, p) = n_0 \, \delta_\mathrm{D}(p - p_0) \,, \tag{2.40}$$

where n_0 is the number density at upstream infinity. The corresponding integral spectrum is then a step function:

$$N_-(p) = N(x = -\infty, p) = \begin{cases} 0 & \text{for } p > p_0 \,, \\ n_0 & \text{for } p \le p_0 \,. \end{cases} \tag{2.41}$$

From the Rankine-Hugoniot jump conditions for the (number) density we then infer that $N_+(p) = N(x = +\infty, p) = \sigma n_0$ for $p \leq p_0$. The downstream integral spectrum is the initial number density $N_+(p_0) = \sigma n_0$ multiplied by the probability of crossing the shock sufficiently often to reach at least a certain momentum $p_k > p_0$:

$$N_+(p_k) = P_k \, N_+(p_0) = \sigma n_0 \left(\frac{p_k}{p_0}\right)^{-3/(\sigma-1)} . \tag{2.42}$$

Finally, the distribution function $f(p)$ can be obtained by differentiating equation (2.39):

$$f(p) = -\frac{1}{4\pi p^2}\frac{\partial N_+(p)}{\partial p} \propto \left(\frac{p}{p_0}\right)^{-3/(\sigma-1)-3} = \left(\frac{p}{p_0}\right)^{-3\sigma/(\sigma-1)} , \quad p > p_0 . \tag{2.43}$$

which is again a power-law with the same slope as in our previous derivation (2.20). An alternative discussion of the microscopic approach that emphasizes more the role of particle number conservation in phase space is presented in Jones and Ellison (1991).

2.5 Summary of assumptions

We just introduced the two most common approaches to diffusive shock acceleration; alternatives can be found in the extensive literature, like in Blandford and Eichler (1987). As it turned out, the universal power-law spectrum resulting from DSA only depends on the compression ratio of the shock and not on the detailed microphysical aspects of particle scattering and diffusion caused by plasma waves. In the following we list some of the simplifying assumption the went into this elementary test-particle approach:

1. The shock front was assumed to be a sharp discontinuity that leaves the velocity of crossing particles unaffected. In reality, every physical shock wave has a finite thickness that is of the same order of magnitude as the particle mean free path, which corresponds to a few gyroradii of thermal protons. For a spherical shock wave, one would expect that particles with a high enough energy have such a large diffusion length ahead of the shock that it exceeds the shock's radius of curvature. In that case the particle is expected to escape upstream, which is not incorporated in our discussion above. In fact, the underlying assumption is that every particle upstream will eventually be advected downstream.

2. The distribution function was assumed to be isotropic in the upstream and downstream reference frame, which means that the particle momentum has to get isotropized through elastic and random scattering at plasma waves very rapidly after crossing the shock front.

3. We assumed that cosmic rays are isotropised in the fluid rest frame both upstream and downstream through pitch-angle scattering at plasma waves, but those scattering centres do not have to move with the same velocity as the fluid. Hence, the relative velocity between upstream and downstream scattering centres does not have to be $u_1 - u_2$, which would also change the power-law slope α.

4. A rather problematic aspect of the derivations above is the assumption that the test particle is already relativistic, which was made in equation (2.28), where we set $E = pc$. Therefore, we emphasize that the distribution function expected from the test-particle approach to diffusive shock acceleration is an *exact* power-law in momentum and not in energy space, because the conversion $E(p) = \sqrt{(pc)^2 + (mc^2)^2}$ introduces a non-linearity at

low momenta. However, for ultra-relativistic energies this effect becomes negligible and $f(p) \propto p^{-\alpha}$ indeed transforms into $f(E) \propto E^{-\alpha+2}$, as can be seen from equation (C.17).

5. A related problem concerns injection of particles from the thermal pool into the DSA process – the so-called "injection problem". To better understand this issue, we again emphasize that in the above derivations we assumed that the shock front was an infinitely thin discontinuity that particles cross unaffectedly during an acceleration cycle. However, a real collisionless shock wave has of course a finite thickness of a few scattering mean free paths, which is of the same order-of-magnitude as a few thermal gyroradii . Therefore, only high-momentum particles with gyroradii significantly larger than those of the thermal population can cross the shock without major deflections. The whole point is that such a supra-thermal seed population of particles able to participate in DSA was assumed to exist a priori. By contrast, in real astrophysical shock waves there are separate mechanisms that pre-accelerate particles strong enough such that DSA can finally take over. The responsible processes are inherently linked to the microphysical details of collisionless shocks and must therefore be investigated with (particle-in-cell) simulations (for further details see Caprioli *et al.*, 2015). From now on, we treat the injection momentum as some model parameter that has to be specified a priori or related to other (time-dependent) quantities, like the shock velocity. We will return to this topic at the end of chapter 3.

There is an additional issue with the standard prediction of DSA: the distribution function does not have a natural momentum cut-off, which leads to a diverging CR energy for $\alpha \leq 4$ if the CR spectrum is integrated from the injection momentum up to infinity:

$$E_{\mathrm{tot}} = 4\pi \int_{p_{\mathrm{min}}}^{\infty} f(p) p^2 E_{\mathrm{CR,kin}}(p)\, \mathrm{d}p \tag{2.44}$$

$$\propto \int_{p_{\mathrm{min}}}^{\infty} p^{-\alpha+2} \left(\sqrt{(pc)^2 + (m_{\mathrm{p}}c^2)^2} - m_{\mathrm{p}}c^2 \right) \mathrm{d}p \tag{2.45}$$

$$\xrightarrow[E \approx pc]{p_{\mathrm{min}} \gg m_{\mathrm{p}}c} \quad E_{\mathrm{tot}} \propto \int_{p_{\mathrm{min}}}^{\infty} p^{-\alpha+2+1}\, \mathrm{d}p = \begin{cases} p^{4-\alpha}\big|_{p_{\mathrm{min}}}^{\infty} & \text{for } \alpha \neq 4 \\ \ln(p)\big|_{p_{\mathrm{min}}}^{\infty} & \text{for } \alpha = 4 \end{cases} \rightarrow \infty \quad \text{for } \alpha \leq 4\,. \tag{2.46}$$

This problem cannot be curated by the simple argument that $\alpha = 3\sigma/(\sigma - 1) > 4$ for $\sigma < 4$ and $\sigma = 4$ is never reached exactly, because it would require an infinitely high Mach number. The reason is twofold – firstly, upstream escape of relativistic protons, which was neglected so far, will increase the compression ratio from $\sigma = 4$ to $\sigma = 7$, because the gas in front of the shock is then relativistic and has an adiabatic index of $\gamma = 4/3$ instead of $\gamma = 5/3$, which will be discussed in the next section??. Subsequently, the total CR energy would hopelessly diverge. Secondly, no real acceleration process, no matter how efficient, is able to accelerate a particle from the thermal pool to infinite energy within a finite amount of time. Hence, imposing an upper cut-off of the distribution function is physically well motivated.

As pointed out e.g. by Blasi (2013) the absence of a maximum energy is related to the assumption of stationarity, meaning that a time-independent distribution function is imposed, which can only be fulfilled if particles can escape from the accelerator. It was nicely demonstrated by Caprioli *et al.* (2009) that a maximum momentum p_{max} naturally arises from the solution of the stationary CR transport equation if the boundary condition $f(x = x_0, p) = 0$ is used, where $x_0 < 0$ is some finite location upstream of the shock. In fact, the resulting distribution function

at the shock front $f_0(p)$ converges to a power law $f_0(p) \propto (p/p_{\max})^{-\alpha}$ for $p \ll p_{\max}$, but is exponentially suppressed for $p \gg p_{\max}$, where $f_0(p) \propto \exp(-p/p_{\max})$. It can be shown that this really corresponds to an upstream particle escape by calculating the CR flux at $x = x_0$, which is indeed non-zero and directed towards upstream infinity. Note, however, that this procedure differs significantly from the derivation in section 2.3, where we integrated up to upstream infinity and expressed the solution of the transport equation in terms of $f_-(p) \coloneqq f(x = -\infty, p)$. Moreover, setting a free escape boundary at a finite distance ahead of the shock is only appropriate when the shock speed is constant in time, which is of course not the case for the decelerating forward shock of a supernova remnant.

3 A model for cosmic ray spectra from supernova remnants

In the main chapter of this Master's thesis, we introduce a model for the cosmic ray spectrum that is released into the interstellar medium by a supernova remnant. It will serve as a sub-grid recipe for CR seeding by supernova remnants in cosmological hydrodynamical simulations, as explained in chapter 4. The basic theory behind all this is of course by no means original, but has been published several years, if not decades ago. However, two crucial papers on this subject appeared fairly recently, namely Cristofari *et al.* (2021) and Morlino and Celli (2021). Each of them contains a model for cosmic rays produced by supernova remnants that takes new results from plasma physics into account (especially the latest findings of particle-in-cell simulations) and allows estimating to what extent energies above the knee in the PeV range can be achieved by CR protons. The model in this thesis is a mixture of these two articles and therefore relies heavily on them – they are the most important references in the bibliography by far.

Of course, any model that is still simple enough to allow a semi-analytical treatment, can only be a caricature of reality. This deficit lies in the very nature of virtually all sub-grid recipes that are used in large-scale cosmological simulations of systems as complex as whole galaxies or even galaxy clusters. Immediately the question arises how reliable, realistic and useful this model really is. A big advantage of an analytical model, that is build step by step from basic principles, is of course its transparency with respect to all assumptions and simplifications that went into it. They will be discussed in great detail throughout this thesis. The model's usefulness can only be addressed a posteriori after running simulations and investigating if there are any new insights or differences to simpler models. From the famous philosophical principle of "Ockham's razor" it is clear that a complicated model that essentially leads to the same conclusions as a simpler one does not really have a scientific value, apart from demonstrating that the simplifications were not too crude in the first place.

3.1 Different types of supernovae

We follow the notation of Cristofari *et al.* (2020, 2021), who distinguish amongst three types of SNe in their cosmic-ray model, which they call Ia, II and II* (see table 3.1 for a general overview). As already mentioned in section 1.1, there is an ambiguity between the physical explosion mechanism and the spectral classification. Since the proposed abbreviations are quite handy, we will also adopt them here and emphasize their precise meaning:

1. Thermonuclear supernovae have the unique spectral type Ia (so in this case the notation above is "unproblematic"). Although no progenitor star has been certainly identified through observations, there are strong hints (e.g. from SN 2011fe) that the exploding star is a carbon-oxygen white dwarf that accretes matter from a binary companion until the Chandrasekhar mass of $\sim 1.4\ M_\odot$ is reached. When this happens a runaway thermonuclear fusion is triggered that tears the white dwarf apart, so that no stellar remnant (besides a

surviving companion) is left. An alternative scenario is provided by so-called double-degenerated models, where the exploding star is a carbon-oxygen white dwarf and its companion is also a white dwarf. According to Maguire (2017), "there are many theoretical predictions of what exactly triggers the primary white dwarf to explode: the steady accretion of the secondary white dwarf onto the primary which reaches the Chandrasekhar mass and explodes, the violent merger of the two white dwarfs which triggers a carbon detonation, or the so-called "double-detonation" scenario, where the detonation of He on the primary white-dwarf surface triggers a carbon detonation in its core that unbinds the star."

2. Core-collapse supernovae are here referred to as type II. Their progenitors are massive stars (above $\sim 8\ \mathrm{M}_\odot$) in the final stages of nuclear burning when silicon is fused to iron. Typically, the progenitors are red supergiants, but in rare cases also a blue supergiant can explode – a famous example is SN 1987A in the Large Magellanic Cloud. Since iron has the highest binding energy of all nuclei, no energy release through nuclear fusion is possible after this stage. If the inactive iron core exceeds the Chandrasekhar mass, it can no longer be supported through electron degeneracy pressure and will start to collapse into a neutron star or a black hole. The bounce-back of the infalling stellar envelope together with heating from neutrinos (released through electron capture of protons) trigger an explosion.

3. To illustrate the wide range of explosion energies resulting from type II, Cristofari *et al.* (2020) also introduce a class of very rare, high-energy core-collapse SNe that they call II*. In the following we assume that the ejecta of these special supernovae have a kinetic energy that is five times larger than the benchmark value of $E_{\mathrm{SN}} \approx 10^{44}$ J. By contrast, the ejecta mass is set to a rather low value of just $1\ \mathrm{M}_\odot$, which enables the cosmic rays to gain very high energies, as found by the parameter study in Cristofari *et al.* (2020).

One of the most important differences between thermonuclear and core-collapse supernovae is that the former expand in a uniform interstellar medium, whereas the latter expand in the circumstellar wind caused by the massive progenitor star. Building a realistic model for shock waves of type II supernovae is extremely challenging, because stellar winds of high-mass (red giant) stars are known to be clumpy and asymmetrical. Moreover, the mass loss does not happen at a constant rate, but might vary significantly over time. Consequently, it is important to keep in mind that the simple density profile of the ambient medium, which is discussed in the next section, is not very adequate for core-collapse SNe.

Additionally, one should take into account that type II supernovae can only occur in galaxies with ongoing star formation, because stars with masses $\gtrsim 8\ \mathrm{M}_\odot$ have main-sequence lifetimes of $\lesssim 35$ Myr. On the contrary, SNe Ia will explode between a few 100 Myr and a few Gyr after formation. That is why in numerical simulations a SN II is treated as prompt event that occurs in the same timestep as star formation (see chapter 4). One should also keep in mind that the usually quoted SN frequencies of 2 (or 3) per century (II) and 1 per century (Ia) are estimates for spiral galaxies similar to the Milky Way. In elliptical galaxies with no current star formation and an old stellar population one would expect that almost 100% of all SNe are of type Ia. Last but not least, we assume that 1.5% of all core-collapse supernovae are of type II*, which is the value required by Cristofari *et al.* (2020) to reproduce the observed CR spectrum with their model. Note that all these considerations on the frequency of certain supernova events are actually not needed for the computation of the CR spectrum, but it is very important for the stochastic seeding in a cosmological model.

3.2 Evolution of supernova remnants

The temporal evolution of a supernova remnant is often simplified by dividing it into four phases (see e.g. Longair, 2011, chap. 16.7; Vink, 2020, chap. 5 and references therein):

1. Ejecta-dominated phase (also called free-expansion phase): During the earliest phase of the supernova remnant evolution the ejected material from the progenitor star is accelerated to very high velocities of about 10^4 km s^{-1}. This greatly exceeds the speed of sound in the interstellar medium (~ 15 km s^{-1}), which leads to the formation of a shock wave. Since the ejecta mass is larger than the swept-up mass in this early stage, the shock front expands with nearly constant velocity.

2. Sedov-Taylor phase (also called adiabatic phase): Once the swept-up mass becomes larger than the ejecta-mass the expansion velocity slows down and the supernova remnant enters the second phase. The shock radius is described by the self-similar adiabatic blast-wave solution $R_{\mathrm{sh}} \propto t^{2/5}$ that was found independently by Sedov and Taylor[1]. Since the shock wave created by the outermost, fastest moving ejecta slows down, the inner unshocked material will eventually catch up with the supernova blast wave (also called forward shock). If this collision happens with supersonic speed (relative to the sound speed inside the remnant), then a second shock wave (the so-called reverse shock) will form on the inner edge of the compressed outer layers. The reverse shock then propagates inward to the origin while reheating the ejected gas.

3. Pressure-driven phase (also called snowplough phase): In this phase radiative losses through line emission of heavy ions become important and the evolution of the remnant is now determined by conservation of momentum (instead of energy). In the inner region of the remnant the decreasing temperature leads to a compression in order to preserve pressure balance at the shock front with the ambient medium. Consequently, the shell turns into a dense "snowplough".

4. Merging phase: Once the expansion velocity of the supernova remnant becomes smaller than the speed of sound or the Alfvén velocity it will start to disperse in the interstellar medium.

When modelling the cosmic ray spectra produced by supernova remnant, only the first two phases are relevant, because we will assume that diffusive shock acceleration stops after the Sedov-Taylor phase, i.e. when the snowplough phase begins at. To calculate the snowplough time t_{SP}, we use the parametrisation from Cioffi *et al.* (1988), which was also reused by Morlino and Celli (2021):

$$t_{\mathrm{SP}} = 9.685 \cdot 10^7 \left(\frac{E_{\mathrm{SN}}}{10^{44}\ \mathrm{J}}\right)^{3/14} \left(\frac{n_{\mathrm{ISM}}}{\mathrm{m}^{-3}}\right)^{-4/7} \mathrm{yr}\,. \tag{3.1}$$

However, one should keep in mind that the Mach number at t_{SP} is still $\gtrsim 10$ and it is not entirely clear, why DSA does not continue thereafter. Possible reasons might be a fragmentation of the shell behind the shock or strong ion-neutral damping of MHD perturbations (meaning less efficient CR scattering) when the shock wave propagates in ordinary ISM during the late evolutionary stages (cf. Morlino and Celli, 2021, and references therein).

[1] Note that the exponent $2/5$ only holds for a uniform ambient medium. Below, we will encounter a generalized Sedov-Taylor solution for power-law density profiles.

A special class of self-similar solutions that describe the temporal evolution of supernova remnants from the beginning of the ejecta-dominated phase until the end of the Sedov-Taylor phase is extensively discussed in Truelove and McKee (1999) (see also the erratum Truelove and McKee, 2000). Roughly speaking, a self-similar phenomenon reproduces itself in time and space, meaning that it looks similar on different scales. A prototypical example for this behaviour are fractal structures, like the Koch curve or the Mandelbrot set. To be more precise, a self-similar function $f(x)$ of one variable fulfils the scaling relation

$$f(\lambda x) = \lambda^a f(x) \tag{3.2}$$

for arbitrary λ and fixed a. For one-dimensional functions self-similarity corresponds to power-laws; a generalization to higher dimensional functions can be found in Barenblatt (2003).

In the following, we model the internal structure of the supernova remnant at $r < R_{\rm sh}$ as a spherically symmetric, blast wave with a linear velocity profile, which was introduced by Ostriker and McKee (1988) and is also similar to the initial conditions in Truelove and McKee (1999):

$$v(r,t) = \left(1 - \frac{1}{\sigma}\right)\frac{v_{\rm sh}(t)}{R_{\rm sh}(t)} r\,, \qquad r < R_{\rm sh}\,. \tag{3.3}$$

As pointed out in Ptuskin and Zirakashvili (2005), this is a good approximation for Sedov's solution and a very good description of the ejecta-dominated phase. The normalization is chosen such that $v(t, R_{\rm sh}(t)) = (1 - 1/\sigma)v_{\rm sh}(t)$. This is the velocity of the downstream plasma right behind the shock front as seen in the (observer's) reference frame, where the shock front moves with velocity $v_{\rm sh}$; in the shock rest frame the downstream velocity would be $v_2 = v_1/\sigma = v_{\rm sh}/\sigma$.

The initial density profile is a bit more complicated and consists of two contributions, namely (1) the ejecta profile $\rho_{\rm ej}$ that is characterized by a "structure function" $f(r/R_{\rm ej})$ and (2) the density $\rho_{\rm amb}$ of the ambient medium, which we assume to be a power-law with index s and normalization ρ_s:

$$\rho(r,t) = \begin{cases} \rho_{\rm ej}(r) = \frac{M_{\rm ej}}{R_{\rm ej}^3(t)}\, f\left(\frac{r}{R_{\rm ej}(t)}\right) & r \le R_{\rm ej}(t)\,, \\ \rho_{\rm amb}(r) = \rho_s r^{-s} & r > R_{\rm ej}(t)\,. \end{cases} \tag{3.4}$$

The dimensionless structure function again consists of two contributions, namely (1) an inner uniform core region from $r = 0$ to $r = R_{\rm core}$ and (2) an outer power-law envelope region with exponent k from $r = R_{\rm core}$ to $r = R_{\rm ej}$:

$$f(w) = \begin{cases} f_0, & 0 \le w \le w_{\rm core}\,, \\ f_0 (w/w_{\rm core})^{-k} & w_{\rm core} \le w \le 1\,. \end{cases} \tag{3.5}$$

Here we introduced the dimensionless radii $w = r/R_{\rm ej}$ and $w_{\rm core} = R_{\rm core}/R_{\rm ej}$. The ejecta radius in equation (3.4) is defined as $R_{\rm ej}(t) := v_{\rm ej} t$, where $v_{\rm ej}$ is the initial maximum ejecta velocity, i.e. the gas velocity at the outermost surface of the ejecta at the beginning of the free-expansion phase. For the hypothetical situation where there is no ambient medium that could decelerate the expanding material, the radius of the outermost ejecta surface will be exactly $R_{\rm ej}(t)$. On the other hand, the core radius $R_{\rm core}(t)$ appearing in the structure function (3.5) is introduced to define the boundary between the inner uniform core region and an outer power-law envelope region. Again, the time dependency can be understood in terms of a constant core velocity, i.e. $R_{\rm core}(t) := v_{\rm core} t$.

As discussed in Truelove and McKee (1999), a power-law ejecta envelope with index $k \ge 3$ requires the presence of a core in order for $M_{\rm ej}$ to be finite. Similarly, $s < 3$ is required so that the swept-up ambient mass $M_{\rm ej}$ remains finite. This can be understood from the general definition of

the integrated mass $M(R)$ for a spherically symmetric density profile,

$$M(R,t) = \int_0^R 4\pi r'^2 \rho(r',t)\,\mathrm{d}r' \,, \tag{3.6}$$

which corresponds to the sum of all mass shells up to a certain radius R. By making the simplifying assumption that ρ is time-independent, we define the ejecta mass M_{ej} and the mass M_{swep} of ambient material the has been swept-up until a certain time t as

$$M_{\mathrm{ej}} \coloneqq M(R_{\mathrm{ej}})\,, \quad M_{\mathrm{swep}}(t) \coloneqq M(R_{\mathrm{sh}}(t))\,. \tag{3.7}$$

Consequently, the above constraints for k and s come from the requirement that $r^2\rho(r)$ should be locally integrable around $r = 0$.

For the ambient density profile we only consider two cases in this thesis, namely $s = 0$ and $s = 2$. The first case corresponds to the explosion of a thermonuclear supernova of type Ia within a uniform medium, so one just sets $\rho_s = \rho_{\mathrm{ISM}} = m\, n_{\mathrm{ISM}}$, where $m = m_{\mathrm{p}}(1 + 4f_{\mathrm{He}})/(1 + f_{\mathrm{He}})$ is the mean molecular weight of the interstellar medium when elements heavier than helium are neglected, as shown in equation (1.4). The second case corresponds to the density profile of a circumstellar wind with constant velocity v_{wind} (in the following we will always assume $v_{\mathrm{wind}} = 10\ \mathrm{km\,s^{-1}}$). This can be seen as follows: From the continuity equation in spherical coordinates one gets the mass-loss rate

$$\dot{M} = 4\pi r^2 \rho(r) v_{\mathrm{wind}} \quad \Longleftrightarrow \quad \rho(r) = \frac{\dot{M}}{4\pi v_{\mathrm{wind}}}\, r^{-2}\,, \tag{3.8}$$

which implies $\rho_s = \dot{M}/(4\pi v_{\mathrm{wind}})$ and $s = 2$. Indeed, it is expected that the progenitor star of a core collapse supernova (e.g. type II) is a red supergiant with a strong, slow and dust-driven wind causing high-mass loss rates of up to $10^{-4}\ \mathrm{M_\odot\,yr^{-1}}$. However, in rare cases the progenitor can also be a blue supergiant, as mentioned before. In summary, we use the following parameters for modelling the density profile of the ejected material, $\rho_{\mathrm{ej}}(r) \propto r^{-k}$, and of the ambient medium, $\rho_{\mathrm{amb}}(r) \propto r^{-s}$:

$$k = \begin{cases} 7 & \text{for type Ia SNe}\,, \\ 9 & \text{for type II SNe}\,, \end{cases} \qquad s = \begin{cases} 0 & \text{for type Ia SNe}\,, \\ 2 & \text{for type II SNe}\,. \end{cases} \tag{3.9}$$

In accordance with Cardillo *et al.* (2015) we choose the parameter combinations $s = 0$, $k = 7$ and $s = 2$, $k = 9$. They can be motivated by matching measurements of the shock radii and velocities for Cassiopeia A, the remnant of a core-collapse supernova that took place ∼350 years ago (see Vink, 2020, chap. 5.6 and references therein).

As pointed out in Truelove and McKee (1999), the initial conditions of the supernova remnant evolution introduce the three independent dimensional parameters, namely the ejecta mass M_{ej}, the normalization ρ_s of the ambient density profile and the kinetic energy E_{SN} of the ejecta. A simple dimensional analysis shows that they can be combined in a unique way to form characteristic scales of length, time, and mass:

$$M_{\mathrm{ch}} = M_{\mathrm{ej}}\,, \tag{3.10}$$

$$R_{\mathrm{ch}} = (M_{\mathrm{ej}}/\rho_s)^{1/(3-s)}\,, \tag{3.11}$$

$$t_{\mathrm{ch}} = E_{\mathrm{SN}}^{-1/2}\, M_{\mathrm{ej}}^{(5-s)/(6-2s)}\, \rho_s^{-1/(3-s)}\,. \tag{3.12}$$

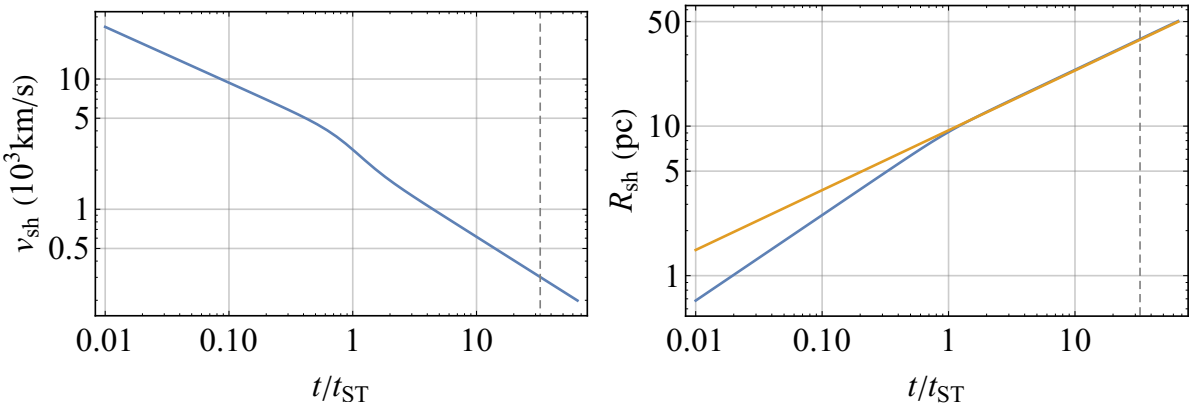

Figure 3.1: Evolution of the shock front of type Ia supernova remnant. Left: shock velocity $v_{sh}(t)$. Right: shock radius $R_{sh}(t)$ (blue line). Note that after $t = t_{ST}$ the function converges to the Sedov-Taylor solution $R_{sh} \propto t^{2/(5-s)}$ (orange line), where the normalization was chosen arbitrarily to make both lines coincide. The grey dashed line marks the beginning of the snowplough phase at $t_{SP} \approx 50$ kyr (equation 3.1).

Tang and Chevalier (2017) proposed a simple analytical expression for the shock radius $R_{sh}(t)$ that is motivated by dimensional analysis and the asymptotic behaviour of $R_{sh}(t)$. For $k > 5$ they obtain the following expression for the forward shock using two dimensionless quantities ζ and ξ that depend on the density profile:

$$R_{sh}(t) = R_{ch}\left(\left(\zeta\left(\frac{t}{t_{ch}}\right)^{(k-3/(k-s))}\right)^{-a} + \left(\xi\left(\frac{t}{t_{ch}}\right)^{2}\right)^{-a/(5-s)}\right)^{-1/a} . \tag{3.13}$$

We now introduce the modified quantities $\tilde{\zeta} := \zeta^{(k-s)/(k-3)}$ and $\tilde{\xi} := \sqrt{\xi}$ to slightly simplify the notation and derive an expression for the shock velocity:

$$R_{sh}(t) = R_{ch}\left(\left(\tilde{\zeta}\frac{t}{t_{ch}}\right)^{-a\lambda_{ED}} + \left(\tilde{\xi}\frac{t}{t_{ch}}\right)^{-a\lambda_{ST}}\right)^{-1/a} , \tag{3.14}$$

$$v_{sh}(t) = \frac{\mathrm{d}R_{sh}(t)}{\mathrm{d}t} = \frac{R_{ch}}{t_{ch}}\left(\frac{R_{sh}(t)}{R_{ch}}\right)^{1+a}\left(\lambda_{ED}\tilde{\zeta}\left(\tilde{\zeta}\frac{t}{t_{ch}}\right)^{-a\lambda_{ED}-1} + \lambda_{ST}\tilde{\xi}\left(\tilde{\xi}\frac{t}{t_{ch}}\right)^{-a\lambda_{ST}-1}\right). \tag{3.15}$$

The value for a can be inferred from table 3.1 below and the exponent λ is given by

$$\lambda = \begin{cases} \frac{k-3}{k-s} & \text{in the ED phase}, \\ \frac{2}{5-s} & \text{in the ST phase}. \end{cases} \tag{3.16}$$

Plots of the shock radius and velocity for the parameters of a type Ia supernova are shown in figure 3.1.

We now have a look at the limiting cases for short and long timescales, which were imposed a priori in Tang and Chevalier (2017) in orderto obtain an explicit solution for the shock radius. For this purpose, it is important to note that for the parameters in table 3.1 we always have $\lambda_{ED} > \lambda_{ST}$. Hence, at early times the first term in parenthesis in equation (3.14) will dominate and vice versa for late times. In particular, for $t \to 0$ the evolution of the forward shock is described by the so-called self-similar driven wave (SSDW) solution with $R_{sh}(t) \propto t^{(k-3)/(k-s)}$ that was first introduced by Chevalier (1982) and is typical for an ejecta envelope with a steep ($k > 5$) density profile, which is the case we are interested in. On the other hand, when $t \to \infty$ the shock radius

Table 3.1: Parameters for the three different types of supernovae in our model: kinetic energy of ejecta E_{SN}; ejecta mass M_{ej}; mass loss rate $\dot{M}$ of progenitor star; rate of supernova events ν_{SN} (for a Milky Way like spiral galaxy); power-law indices k and s of ejecta and ambient density profile; exponents λ_{ED} and λ_{ST} determining the shock evolution during ED and ST phase; dimensionless normalization constants ξ and ζ used for $R_{\mathrm{sh}}(t)$; time t_{trans} and radius R_{trans} at transition between ED and ST phase. Most of the parameters were directly copied from Tang and Chevalier (2017).

	Ia	II	II*
E_{SN} (J)	10^{44}	10^{44}	$5 \cdot 10^{44}$
M_{ej} ($\mathrm{M}_\odot$)	1	5	1
$\dot{M}$ ($\mathrm{M}_\odot\,\mathrm{yr}^{-1}$)	-	10^{-5}	10^{-4}
v_{wind} ($\mathrm{km\,s}^{-1}$)	-	10	10
ν_{SN} (yr^{-1})	1/100	1/50	0.015/50
k	7	9	9
s	0	2	2
λ_{ED}	4/7	6/7	6/7
λ_{ST}	2/5	2/3	2/3
a	20.3	5.16	5.16
ξ	2.026	$3/(2\pi)$	$3/(2\pi)$
ζ	1.06	0.97	0.97
$t_{\mathrm{tran}}/t_{\mathrm{ch}}$	1.62	0.32	0.32
$R_{\mathrm{tran}}/R_{\mathrm{ch}}$	1.35	0.32	0.32

approaches the Sedov-Taylor solution, $R_{\mathrm{sh}}(t) \propto t^{2/(5-s)}$. Moreover, if the exponent $a \to \infty$, then equation (3.14) represents an instantaneous transition form ED to ST phase (similar to the piecewise definition of $R_{\mathrm{sh}}(t)$ in Truelove and McKee, 1999), whereas for $a \to 0$ this transition happens infinitely slowly. This can be quantified by defining the transition time t_{trans} and radius $R_{\mathrm{trans}} = R_{\mathrm{sh}}(t_{\mathrm{trans}})$ as the time when the two terms on the right-hand side of equation (3.14) are equal. A straightforward computation leads to the identity

$$\lambda_{\mathrm{ED}} - \lambda_{\mathrm{ST}} = \frac{(k-5)(3-s)}{(5-s)(k-s)}\,, \tag{3.17}$$

which yields

$$t_{\mathrm{ST}} \equiv t_{\mathrm{tran}} = t_{\mathrm{ch}} \left(\tilde{\xi}^{\lambda_{\mathrm{ST}}} \tilde{\zeta}^{-\lambda_{\mathrm{ED}}}\right)^{\frac{1}{\lambda_{\mathrm{ED}}-\lambda_{\mathrm{ST}}}} = t_{\mathrm{ch}} \left(\frac{\xi}{\zeta^{5-s}}\right)^{(k-s)/[(k-5)(3-s)]}\,, \tag{3.18}$$

$$R_{\mathrm{tran}} = R_{\mathrm{sh}}(t_{\mathrm{trans}}) = R_{\mathrm{ch}} \frac{\zeta}{2^{1/\alpha}} \left(\frac{t_{\mathrm{tran}}}{t_{\mathrm{ch}}}\right)^{(k-3)/(k-s)} = R_{\mathrm{ch}} \frac{\zeta}{2^{1/\alpha}} \left(\frac{\xi}{\zeta^{5-s}}\right)^{(k-3)/[(k-5)(3-s)]}\,. \tag{3.19}$$

In the following, we will use the term "Sedov-Taylor time" rather than "transition time", since the former is more common in the scientific literature. It was also emphasized in equation 3.18 that both terms stand for the same quantity.

3.3 Cosmic ray spectrum at the shock front

In our discussion about diffusive shock acceleration in chapter 2 it was assumed that the CR distribution function is isotropic in momentum (in the fluid rest frame) and essentially one-dimensional in its spatial coordinates. Since we consider a spherically symmetric supernova

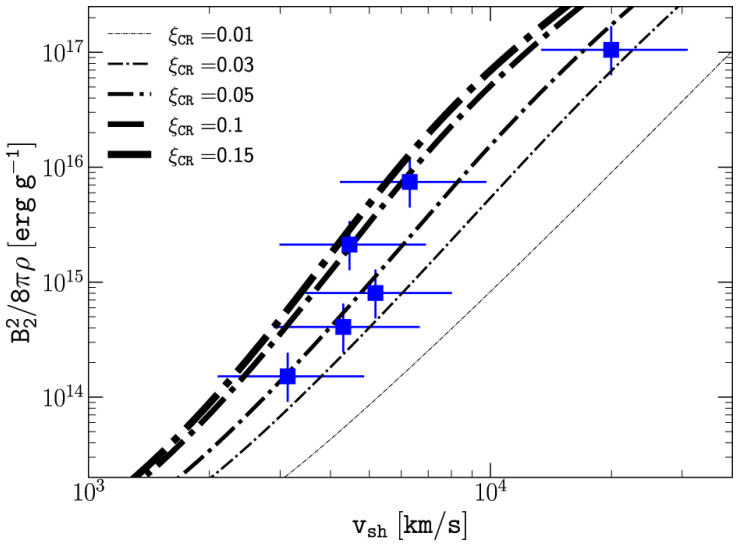

Figure 3.2: Downstream magnetization (magnetic energy per unit mass, expressed in CGS units) as a function of shock velocity v_{sh}. The black dotted-dashed lines correspond to calculations that use different values for the CR efficiency ξ_{CR}. In general, the data points seem to be better described when the acceleration efficiency is around 5%–10% (from Cristofari *et al.*, 2022).

remnant, it is natural to write the CR distribution function as $f(r, p, t)$, where r is the radial distance from the remnant centre and p is the particle's momentum in the rest frame of the ambient ISM (upstream rest frame). Note that the momentum is essentially the same in the upstream, downstream and shock rest frame, because the shock is non-relativistic, but the particle is highly relativistic. Therefore, we will from now on simply refer to p as the particle momentum without any further (unnecessary) specifications concerning the reference frame. In chapter 2 we saw that (to first order) particles accelerated at the shock have a power-law spectrum

$$f_{sh}(p,t) \coloneqq f(R_{sh}(t), p, t) = A(t)(p/m_p c)^{-\alpha}\,\Theta(p - p_{inj}(t))\,\exp(-p/p_{max}(t))\,, \tag{3.20}$$

so we neglect the spectral curvature that may arise if there is a strong precursor and particles of different p feel different compression ratios. The lower cut-off at the injection momentum $p_{inj}(t)$ is modelled with a Heaviside function, which could also be adopted for the upper cut-off (like in Ptuskin and Zirakashvili, 2005). However, here we use an upper cut-off at some maximum momentum p_{max} (like in Morlino and Celli, 2021), which is not naturally embedded in standard DSA, but introduced for physical reasons, as already mentioned in section 2.5. We also noted that a maximum momentum and the exponential spectral cut-off naturally arise if the stationary CR transport equation is solved by imposing a boundary condition at some finite location upstream (cf. Caprioli *et al.*, 2009).

Besides the two spectral cut-offs, we also include the time dependence of $p_{inj}(t)$ and $p_{max}(t)$ a priori. The normalization function $A(t)$ can be determined by demanding that the total CR energy is either $\sim 10\%$ of the kinetic energy stored in the ejecta material[2] or a fraction ξ_{CR} of the ram pressure at the shock. Here, we choose the second approach and therefore set

$$P_{CR}(R_{sh}) \stackrel{!}{=} \xi_{CR}\, P_{ram} = \xi_{CR}\, \rho_{amb}\, v_{sh}^2\,, \tag{3.21}$$

where ρ_{amb} is the mass density of the ambient gas (cf. equation (3.4)) and ξ_{CR} is also called "acceleration efficiency". This choice for the spectral normalization has the advantage that ξ_{CR}

[2]This was part of the "energy argument" in section 1.4.1 supporting the paradigm that supernova remnants are the main source of Galactic cosmic rays.

can roughly be inferred from observations of SNRs, as shown in figure 3.2. Besides that, the total CR energy of the final spectrum can then be calculated as a consistency check.

By inserting equation (C.13) for the CR pressure from appendix C (which is exact for ultra-relativistic particles) into equation 3.21 and using the simple cut-off $\Theta(p_{\max}(t) - p)$ instead of the exponential factor in equation (3.20), one obtains

$$\xi_{\mathrm{CR}}\,\rho_{\mathrm{amb}}\,v_{\mathrm{sh}}^2 = P_{\mathrm{CR}}(R_{\mathrm{sh}}) = \frac{4\pi}{3}\int_0^\infty f_{\mathrm{sh}}(p)\,p^3\,v(p)\,\mathrm{d}p = \frac{4\pi}{3}\int_{p_{\mathrm{inj}}(t)}^{p_{\max}(t)} A(t)\left(\frac{p}{m_{\mathrm{p}}c}\right)^{-\alpha} p^3\,v(p)\,\mathrm{d}p \tag{3.22}$$

$$\implies \quad A(t) = \frac{3\xi_{\mathrm{CR}}\rho_{\mathrm{amb}}v_{\mathrm{sh}}^2}{4\pi c(m_{\mathrm{p}}c)^4\,\Lambda(\alpha,t)}\,, \tag{3.23}$$

where we introduced the auxiliary function

$$\Lambda(\alpha,t) := \int_{p_{\mathrm{inj}}(t)/(m_{\mathrm{p}}c)}^{p(t)/(m_{\mathrm{p}}c)} \frac{x^{4-\alpha}}{\sqrt{1+x^2}}\,\mathrm{d}x\ . \tag{3.24}$$

This normalization is frequently quoted in the literature, but strictly speaking only sensible for a cut-off modelled by a step function. Instead, we use the following more consistent equation for an exponential cut-off (the derivation is analogous):

$$\Lambda(\alpha,t) = \int_{p_{\mathrm{inj}}(t)/(m_{\mathrm{p}}c)}^{\infty} \frac{x^{4-\alpha}}{\sqrt{1+x^2}}\,\exp\left(-\frac{x}{p_{\max}(t)/(m_{\mathrm{p}}c)}\right)\mathrm{d}x\ . \tag{3.25}$$

It turns out that Λ only weakly depends on the integral boundaries $p_{\mathrm{inj}}(t)$ and $p_{\max}(t)$, so they affect the spectral shape more than the normalization. As discussed in section **??**, it was expected that non-linear effects of diffusive shock acceleration should result in a concave spectrum, which is flatter than p^{-4}. Although this is not compatible with the measured slope of the CR spectrum detected in the Earth's neighbourhood, it was still used in the earlier papers on cosmic ray acceleration in SNRs. One example is Ptuskin and Zirakashvili (2005), where the parametrization $f_{\mathrm{sh}}(p) \propto p^{-4+a}$ with $0 < a < 0.5$ was used for the distribution of ultra-relativistic particles at the shock. However, state-of-the-art PIC simulations strongly suggest a steeper spectrum at the shock, so we adopt $f_{\mathrm{sh}}(p) \propto p^{-4.3}$.

3.4 Magnetic field amplification

An important ingredient in our CR model is the description of $p_{\mathrm{max},0}(t)$, which is defined as the maximum proton momentum, which can be achieved through acceleration at the shock at a certain time. There are several possibilities to model $p_{\mathrm{max},0}(t)$. A particularly simple description, that will be used in the following and was proposed by Celli *et al.* (2019); Morlino and Celli (2021) assumes that $p_{\mathrm{max},0}(t)$ increases linearly from the beginning of the SNR evolution up to the Sedov-Taylor time (or the transition time, as it was called in section 3.2), where the maximum momentum p_{M} is reached. After that, the decreasing strength of the shock wave leads

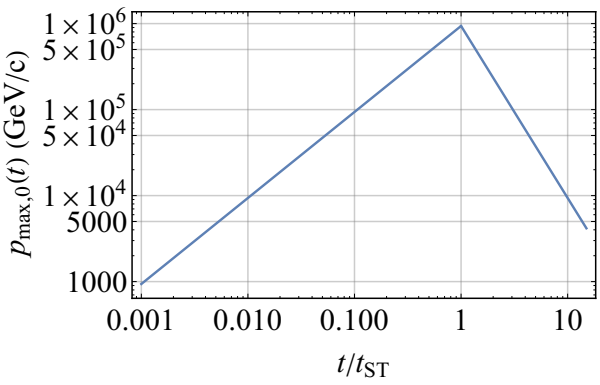

Figure 3.3: Parametrization for the maximum proton momentum at the shock $p_{\mathrm{max},0}(t)$ according to equation (3.26). This is one of the key ingredients of the whole CR model!

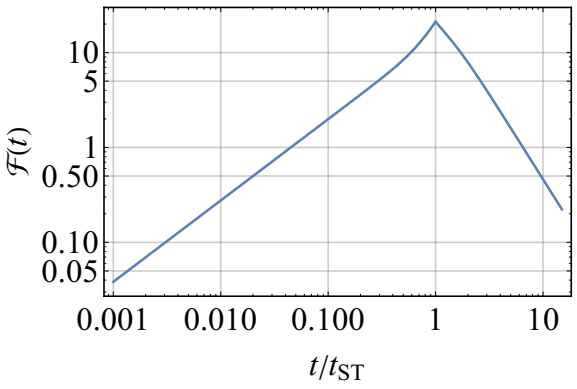

Figure 3.4: Power spectrum $\mathcal{F}(t)$ per unit logarithmic bandwidth for the perturbed component $\delta B_1(t)$ of the upstream magnetic field according to equation (3.36).

to less effective particle acceleration and hence to a decline of $p_{\mathrm{max},0}(t)$, which is modelled by a power-law with index δ. Hence, we have (see figure 3.3)

$$p_{\mathrm{max},0}(t) = \begin{cases} p_{\mathrm{M}}\,(t/t_{\mathrm{ST}}) & \text{if } t \leq t_{\mathrm{ST}}\,, \\ p_{\mathrm{M}}\,(t/t_{\mathrm{ST}})^{-\delta} & \text{if } t > t_{\mathrm{ST}}\,. \end{cases} \tag{3.26}$$

The momentum-dependent escape time $t_{\mathrm{esc}}(p)$ can be obtained through the following argument. Before the transition time is reached, no escape is possible, because the maximum momentum of particles that can still be confined at the shock (and therefore inside the SNR) increases monotonically. Since every CR particle has a momentum $p \leq p_{\mathrm{M}}$, after t_{ST} there will be a time $t_{\mathrm{esc}} \geq t_{\mathrm{ST}}$, where

$$p > p_{\mathrm{max},0}(t_{\mathrm{esc}}) = p_{\mathrm{M}}\,(t_{\mathrm{esc}}/t_{\mathrm{ST}})^{-\delta}\,. \tag{3.27}$$

This condition can be written explicitly in terms of the escape time, yielding

$$t_{\mathrm{esc}}(p) = \begin{cases} t_{\mathrm{SP}} & \text{if } p \leq p_{\mathrm{max},0}(t_{\mathrm{SP}})\,, \\ t_{\mathrm{ST}}\,(p/p_{\mathrm{M}})^{-1/\delta} & \text{if } p > p_{\mathrm{max},0}(t_{\mathrm{SP}})\,. \end{cases} \tag{3.28}$$

The case distinction is made, because it is assumed that the lowest energy particles escape at latest when the snowplough phase begins at t_{SP} and particle acceleration stops (as mentioned before, particles are only accelerated during the first two phases of the SNR evolution).

Another way to obtain the maximum permissible proton momentum as a function of time was proposed by Cristofari *et al.* (2020, 2021) and relies on the microphysics of plasma waves that enable efficient CR scattering, which is required for DSA. Since we will not directly use this approach in this Master's thesis, we will only discuss the basic ideas very briefly; detailed explanations can be found e.g. in Schure and Bell (2013) or in the review Schure *et al.* (2012). The preferred instabilities responsible for the generation of plasma waves are caused by CRs that either escape upstream or are reflected back into the inflowing gas when the shock is supercritical, which is always the case for high-Mach number shocks of supernova remnants. On the one hand, streaming instabilities can produce resonant plasma modes, whose wavelengths coincide with the Larmor radius r_{L} of a CR proton with given momentum. As a consequence, CRs can efficiently scatter at those waves, allowing for diffusive confinement at the shock and therefore efficient particle acceleration. This resonance condition is visualized quite intuitively in figure 3.5.

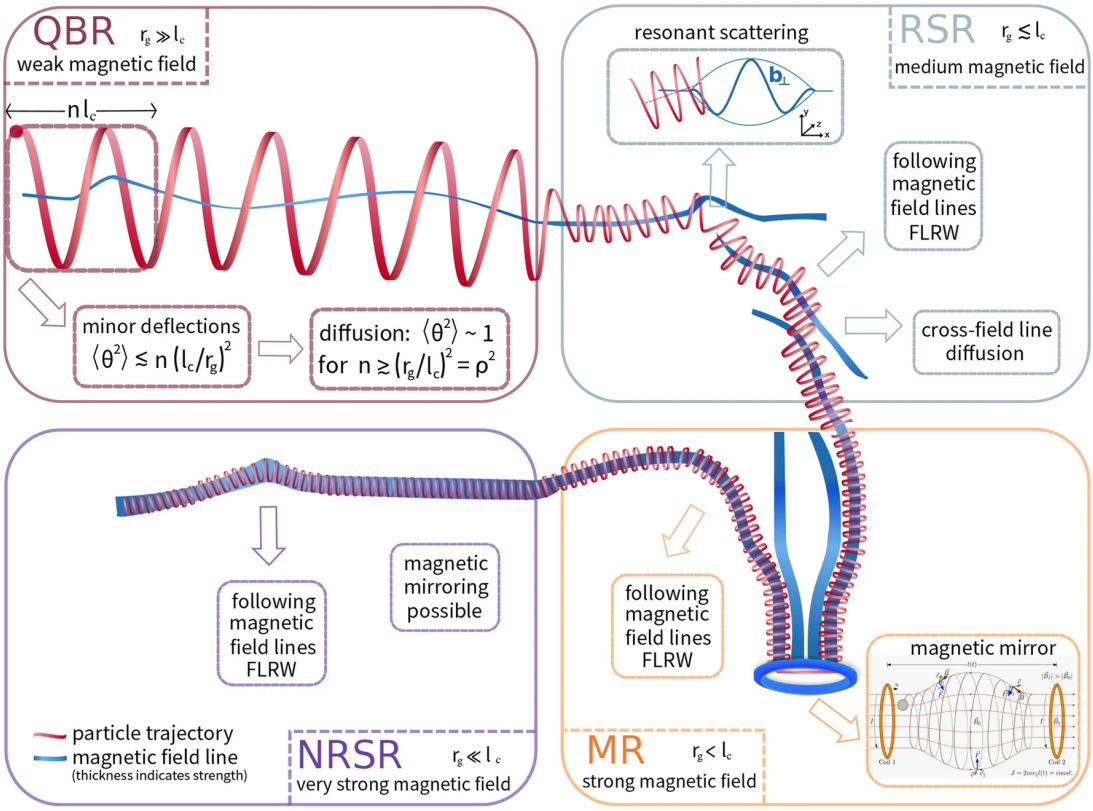

Figure 3.5: Schematic picture of a charged particle travelling through different magnetic field configurations. This figure was taken from Reichherzer *et al.* (2022) and contains much more information than is required in this section. The main point is the following: if the charged particle has a large Larmor radius compared to magnetic field irregularities (top left), then it will just spiral around the filed lines and propagate quasi-ballistically. However, if the Larmor radius becomes comparable to the magnetic field perturbations, the particle will gradually change its pitch-angle, which results in resonant scattering. This is a pictorial explanation for the resonance condition $k_{\max} = 1/r_{\mathrm{L}}$ mentioned in the text.

However, Bell (2004) found that non-resonant hybrid modes grow much faster, with the caveat that the fastest growing mode has a wave number $k_{\max}$ much smaller than $1/r_{\mathrm{L}}$. Nevertheless, cosmic ray scattering becomes possible thanks to the growth of eddies that saturate when the resonance condition $k_{\max} \approx 1/r_{\mathrm{L}}$ is reached. Typically, saturation is reached after a few (~ 5) e-folds of growth, which translates into the following condition for the maximum momentum:

$$\left(\frac{p_{\max,0}(t)}{m_{\mathrm{p}}c}\right)^{\alpha-3} = \frac{3eR_{\mathrm{sh}}(t)}{10m_{\mathrm{p}}c}\frac{\sqrt{\mu_0\rho}}{c}\frac{\xi_{\mathrm{CR}}v_{\mathrm{sh}}(t)^2}{(\alpha-3)\Lambda(\alpha,t)}. \tag{3.29}$$

Without question this approach is more physical, since it is based on a consistent treatment of the Bell instability and no free parameter p_{M} describing the maximum achievable proton momentum has to be introduced by hand. However, the resulting expression for $p_{\max,0}$ is more complicated than the simple power-law (3.26) from above, so the escape time cannot be obtained by an explicit inversion and other strategies have to be used, which might be explored in future work. Another complication arises, because the fast growing Bell instability cannot be excited if the shock speed drops below a critical value, $v_{\mathrm{sh}} < v_{\mathrm{sh}}^*$, which is derived from the condition that saturation pressure of the resonantly amplified upstream magnetic field equals that of the Bell instability, i.e. $P_{\mathrm{B_1,res}} = P_{\mathrm{B_1,Bell}}$. As shown in Diesing and Caprioli (2021), the critical velocity

can be expressed through the Alfvén speed,

$$v_{\mathrm{sh}}^{*} = \sqrt{\frac{c\, v_A}{6}} \approx 570\ \mathrm{km\,s^{-1}}\,, \tag{3.30}$$

where the numerical result holds for typical values of B_{ISM} and n_{ISM}. Consequently, $p_{\mathrm{max},0}(t)$ has to be calculated from the resonant streaming instability once the shock speed has dropped below v_{sh}^{*}, which will typically happen before the snowplough phase is reached (cf. figure 3.1).

After clarifying the treatment of the maximum proton momentum at the shock $p_{\mathrm{max},0}(t)$ in equation (3.26), we now discuss how the amplified magnetic fields upstream and downstream are calculated. Since we follow exactly the detailed treatment in Morlino and Celli (2021), only the main points will be repeated here. First of all, the time $t_{\mathrm{acc}}(p)$ that is needed to accelerate a proton to a given momentum p via DSA is given by (see Vink, 2020, chap. 11.2 for a detailed derivation)

$$t_{\mathrm{acc}} \approx \frac{8 D_1}{v_{\mathrm{sh}}^2}\,. \tag{3.31}$$

The upstream diffusion coefficient D_1 resulting from pitch-angle scattering of CRs at magnetic turbulences is (see Blasi, 2013, for a derivation from pitch-angle scattering)

$$D_1(p,t) = \frac{D_{\mathrm{B}}(p)}{\mathcal{F}(t)}\,. \tag{3.32}$$

The so-called Bohm diffusion coefficient, which we already encountered in section 1.4, is defined as

$$D_{\mathrm{B}} \coloneqq \frac{1}{3} r_{\mathrm{L}} c\,. \tag{3.33}$$

This is the minimum possible value for the CR diffusion coefficient, because the scattering mean free path is assumed to be equal to the CR Larmor radius, which requires that the magnetic field is disordered on this length-scale. For even smaller irregularities in the magnetic field, CR scattering becomes inefficient (see figure 3.5). $\mathcal{F}(t)$ is the magnetic logarithmic power spectrum, which is usually defined as a function of wave number k:

$$\left(\frac{\delta B(k)}{B_0}\right)^2 = \int \frac{\mathcal{F}(k')}{k'}\,\mathrm{d}k' = \int \mathcal{F}(k')\,\mathrm{d}\ln(k')\,. \tag{3.34}$$

Hence, $\mathcal{F}(k)$ is the energy density of the turbulent magnetic field component δB normalized by that of the ordered field B_0 per unit logarithmic bandwidth. This can be understood as a function of time by evaluating $\mathcal{F}$ at the resonant wave number $k_{\mathrm{res}}(t) = 1/r_{\mathrm{L}}(p_{\mathrm{max},0}(t))$, where CR scattering is most efficient.

By assuming that $p_{\mathrm{max},0}(t)$ is determined by the age-limited condition that t_{acc} corresponds to the momentary age of the SNR, an explicit expression for $\mathcal{F}(t)$ can be obtained as follows:

$$\mathcal{F}(t) = \frac{D_B}{D_1} = \frac{r_{\mathrm{L}} c}{3}\left(\frac{t v_{\mathrm{sh}}^2}{8}\right)^{-1} = \frac{p_{\mathrm{max},0}(t) c}{3 e B_0}\frac{8}{t v_{\mathrm{sh}}(t)^2} = \frac{8}{3 e c B_0 t}\left(\frac{v_{\mathrm{sh}}(t)}{c}\right)^{-2} p_{\mathrm{max},0}(t)\,. \tag{3.35}$$

Inserting equation (3.26) for $p_{\mathrm{max},0}(t)$ yields (see figure 3.4)

$$\mathcal{F}(t) = \frac{8\, p_{\mathrm{M}}}{3\, e B_0\, c\, t_{\mathrm{ST}}} \begin{cases} \left(\frac{v_{\mathrm{sh}}}{c}\right)^{-2} & t < t_{\mathrm{ST}}\,, \\ \left(\frac{v_{\mathrm{sh}}}{c}\right)^{-2} \left(\frac{t}{t_{\mathrm{ST}}}\right)^{-\delta-1} & t \geq t_{\mathrm{ST}}\,. \end{cases} \tag{3.36}$$

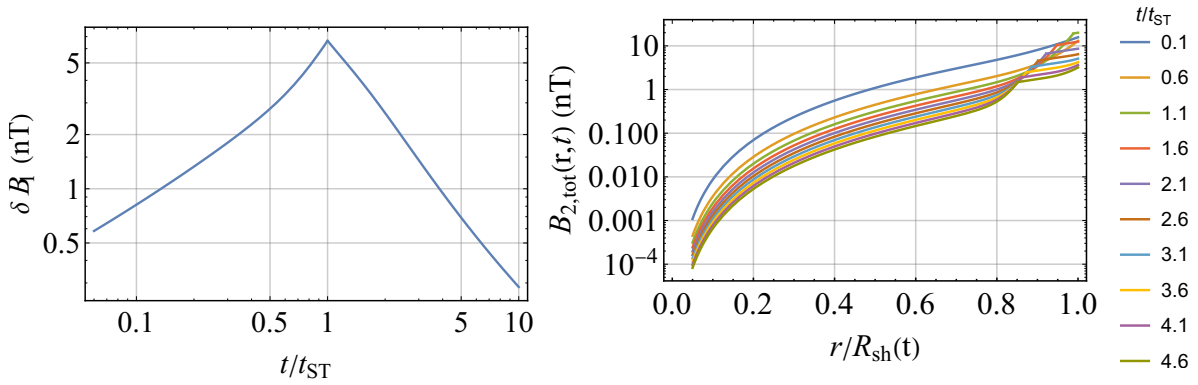

Figure 3.6: Amplified magnetic flux density of the supernova remnant. Left: amplified, perturbed component of the upstream magnetic field δB_1 (cf. equation 3.39). Right: total amplified downstream magnetic field $B_{2,\mathrm{tot}}$ (cf. equation 3.44).

After these preparations we come to the magnetic flux density. The total magnetic field upstream of the shock can be written as the geometric sum of the ordered background field B_0 in the ISM (typically $B_0 \approx 0.3$ nT) and the self-generated magnetic field δB_1 caused by CR streaming instabilities immediately upstream of the shock:

$$B_{1,\mathrm{tot}}(t) = \sqrt{B_0^2 + \delta B_1^2(t)}\,. \tag{3.37}$$

In Morlino and Celli (2021) Bohm-like diffusion of CRs was assumed, meaning that the power spectrum is related to the magnetic field via

$$\mathcal{F}^{-1} = \left(\frac{B_0}{\delta B_1}\right) + \left(\frac{B_0}{\delta B_1}\right)^2. \tag{3.38}$$

This quadratic equation has one positive root, namely

$$\delta B_1(t) = \frac{B_0}{2}\left(\mathcal{F}(t) + \sqrt{4\mathcal{F}(t) + \mathcal{F}^2(t)}\right). \tag{3.39}$$

This allows us to calculate $\delta B_1(t)$ (and therefore also $B_{1,\mathrm{tot}}(t)$) from (3.36). The result is plotted in figure 3.39.

Calculating the downstream magnetic field is a bit more trickier, since several effects play a role, namely adiabatic losses and damping. The ordered component is diluted as

$$B_{2,0}^2(r,t) = \frac{B_0^2}{3}\left[\left(\frac{R_{\mathrm{sh}}(t)}{r}\right)^4 + 2\sigma^2 L^6(t_0,t)\left(\frac{R_{\mathrm{sh}}(t)}{r}\right)^2\right], \quad t_0 = t_0(r,t)\,, \tag{3.40}$$

whereas the turbulent component of the downstream field suffers adiabatic losses and non-linear damping (given by the exponential suppression):

$$\delta B_2^2(t) = \frac{\delta B_1^2}{3}\left[\left(\frac{R_{\mathrm{sh}}(t)}{r}\right)^4 + 2\sigma^2 L^6(t_0,t)\left(\frac{R_{\mathrm{sh}}(t)}{r}\right)^2\right] \mathrm{e}^{-(t-t_0)\Gamma_{\mathrm{nld}}}, \quad t_0 = t_0(r,t)\,. \tag{3.41}$$

The simplest approach towards the damping term is to assume that it is a constant, so $\Gamma_{\mathrm{nld}} = 1/(3 \cdot 10^3\ \mathrm{yr})$, but see also the more involved treatment of Ptuskin and Zirakashvili (2003). The adiabatic loss function $L(t_0,t)$ and the time $t_0(r,t)$, when a plasma element was shocked, will

be properly introduced in the next section. Additionally, turbulent magnetic field amplification downstream of the shock is included through a very elementary ansatz, where the magnetic energy density is assumed to be a fixed fraction ξ_B of the shock kinetic energy:

$$\frac{\delta B_{2,\mathrm{turb}}^2(t)}{2\mu_0} = \xi_\mathrm{B} \frac{\rho_\mathrm{amb} v_\mathrm{sh}^2(t)}{2} \,. \tag{3.42}$$

The resulting turbulently amplified field is calculated by including damping, whereas compression is neglected ($\sigma = 1$):

$$B_{2,\mathrm{turb}}^2 = \frac{\delta B_{1,\mathrm{turb}}^2}{3} \left[\left(\frac{R_\mathrm{sh}(t)}{r} \right)^4 + 2L^6(t_0, t) \left(\frac{R_\mathrm{sh}(t)}{r} \right)^2 \right] \mathrm{e}^{-(t-t_0)\Gamma_\mathrm{nld}} \,, \quad t_0 = t_0(r,t) \,. \tag{3.43}$$

Finally, the total magnetic field strength is the geometric sum of the ordered, the self-generated and the turbulent components, resulting into

$$\begin{aligned} B_{2,\mathrm{tot}}^2(r,t) &= B_{2,0}^2 + \delta B_2^2 + B_{2,\mathrm{turb}}^2 \\ &= \left[\left(\frac{R_\mathrm{sh}(t)}{r} \right)^4 + 2\sigma^2 L^6(t_0, t) \left(\frac{R_\mathrm{sh}(t)}{r} \right)^2 \right] \frac{1}{3} \left(B_0^2 + \delta B_1^2(t)\, \mathrm{e}^{-(t-t_0)\Gamma_\mathrm{nld}} \right) \\ &+ \left[\left(\frac{R_\mathrm{sh}(t)}{r} \right)^4 + 2L^6(t_0, t) \left(\frac{R_\mathrm{sh}(t)}{r} \right)^2 \right] \frac{\delta B_{2,\mathrm{turb}}^2}{3} \mathrm{e}^{-(t-t_0)\Gamma_\mathrm{nld}} \,. \end{aligned} \tag{3.44}$$

In figure 3.6 the total downstream magnetic field is plotted as function of radius for different fixed values of t.

3.5 Energy loss mechanisms

In this section we discuss three energy loss mechanisms that are important for cosmic rays trapped inside a SNR, namely synchrotron, inverse Compton and adiabatic losses. Other processes, like ionization losses or bremsstrahlung will not be treated here, because they are much less significant. For an extensive overview and numerical values of typical loss timescales we refer to Longair (2011, chap. 16.2).

We begin with radiative losses from (1) synchrotron radiation that is emitted by high-energy charged particles gyrating in a magnetic field and (2) inverse Compton scattering of cosmic rays with photons from the interstellar radiation field, where the photon gains energy that is lost by the cosmic ray particle. Here, we solely focus on CR electrons, as will be explained below. The pitch angle-averaged energy loss of both types of radiation can be written most generally as:

$$\frac{\mathrm{d}E}{\mathrm{d}t} = -\frac{4}{3}\sigma_T c u \gamma^2 \left(\frac{v}{c} \right)^2 = -\frac{2}{3\mu_0}\sigma_T c B^2 \left(\frac{E}{m_\mathrm{e} c^2} \right)^2 \left(\frac{v}{c} \right)^2 , \tag{3.45}$$

where u is the energy density of either the magnetic field or the radiation field. $E = \gamma m_\mathrm{e} c^2$ is the total relativistic energy (rest mass plus kinetic energy) of an electron with charge $q = -e$, mass m_e and Lorentz factor $\gamma := (1 - v^2/c^2)^{-1/2}$. The Thomson cross section is defined as

$$\sigma_T = \frac{8\pi}{3} \left(\frac{e^2}{4\pi\varepsilon_0 m_\mathrm{e} c^2} \right)^2 .$$

In the following we adopt the approach in Morlino and Celli (2021) and use the ultra-relativistic approximation ($v \approx c$) of equation (3.45):

$$\frac{\mathrm{d}E}{\mathrm{d}t} = -\frac{4}{3}\sigma_T c u \gamma^2 = -\frac{32\pi}{9}\left(\frac{e^2}{4\pi\varepsilon_0 m_\mathrm{e} c^2}\right)^2 c u \gamma^2 \tag{3.46}$$

$$\Longrightarrow \quad \left(\frac{\mathrm{d}E}{\mathrm{d}t}\right)_\mathrm{syn} = -\frac{2}{3\mu_0}\sigma_T c B^2 \gamma^2 \,. \tag{3.47}$$

In the first line the general mass dependence $\mathrm{d}E/\mathrm{d}t \propto m^{-2}$ is explicitly shown. One sees immediately, that energy losses are significantly stronger for electrons than for protons. In the second line we set $u = u_B = B^2/(2\mu_0)$ in order to express the synchrotron power through the magnetic flux density, which has a typical ISM value of $B \approx 0.3$ nT. As discussed in the previous section, the downstream magnetic field B_2 in a SNR is expected to be significantly amplified.

On the other hand, the interstellar radiation field is strongly dependent on the position within a galaxy and consists of several different sources, like the CMB, starlight, dust emission or non-thermal radio synchrotron emission (for details see e.g. Draine, 2011, chap. 12). Here we consider an ISRF consisting of the CMB and an infrared, an optical and an ultraviolet component:

$$u_\mathrm{rad} = u_\mathrm{CMB} + u_\mathrm{IR} + u_\mathrm{opt} + u_\mathrm{UV} = (0.26 + 0.02 + 0.2 + 0.43)\ \mathrm{MeV\,m^{-3}} \,. \tag{3.48}$$

The numerical values are from Morlino and Celli (2021), who considered an arbitrary source distance of 4 kpc from the galactic centre. Since synchrotron and inverse Compton loss rates are described by the same formula (3.46), it is convenient to define a so-called equivalent magnetic field B_eq for a given radiation field u_rad via $B_\mathrm{eq} := \sqrt{2\mu_0 u_\mathrm{rad}} \approx 0.61$ nT. Therefore, both types of radiative energy losses can be combined as

$$\left(\frac{\mathrm{d}E}{\mathrm{d}t}\right)_\mathrm{rad} = \left(\frac{\mathrm{d}E}{\mathrm{d}t}\right)_\mathrm{syn} + \left(\frac{\mathrm{d}E}{\mathrm{d}t}\right)_\mathrm{IC} = -\frac{2}{3\mu_0}\sigma_T c \left(\frac{E}{m_\mathrm{e} c^2}\right)^2 \left(B_\mathrm{2,tot}^2 + B_\mathrm{eq}^2\right) = -A_\mathrm{rad} E^2 B_\mathrm{eff}^2 \,. \tag{3.49}$$

In the last step we defined the constant $A_\mathrm{rad} := 2\sigma_T/(3\mu_0 m_\mathrm{e}^2 c^3)$ and the "effective magnetic field" $B_\mathrm{eff}^2(t) := B_\mathrm{2,tot}^2(t) + B_\mathrm{eq}^2$. This ordinary differential equation is quite handy and allows us to motivate the loss time as

$$\tau_\mathrm{loss} := \left|\frac{E}{\dot{E}}\right| = \left(A_\mathrm{rad} E\, B_\mathrm{eff}^2\right)^{-1} \,. \tag{3.50}$$

This definition is indeed plausible and natural, since for a time-independent magnetic flux density the differential equation $\dot{E} = -A_\mathrm{rad} E^2 B_\mathrm{eff}^2$ has the exact solution $E(t) = E(t_0)\,(1 + (t - t_0)/\tau)^{-1}$ with $\tau := (A_\mathrm{rad} B^2 E(t_0))^{-1}$, which is essentially the same time scale as above. More specifically, one obtains the total/synchrotron/IC loss time if one replaces $\dot{E}$ by $\dot{E}_\mathrm{rad}/\dot{E}_\mathrm{syn}/\dot{E}_\mathrm{IC}$ and if one inserts $B_\mathrm{eff}/B_\mathrm{2,tot}/B_\mathrm{eq}$ for B. Note that although the ISM magnetic flux density $B_\mathrm{ISM} \approx 0.3$ nT and the equivalent field of the ISRF $B_\mathrm{eq} = 0.61$ nT are comparable in magnitude, within a SNR the magnetic field is significantly amplified so that synchrotron losses will dominate over IC losses due to the shorter timescale. Hence, only in galactic environments with a high radiation field, like the central region, IC losses will be important.

As already emphasized, the radiative losses are only considered for electrons inside the SNR and ignored for protons, because the timescales differ by a factor $(m_\mathrm{p}/m_\mathrm{e})^2 \approx 3.4 \cdot 10^6$. However, both particle species equally suffer from adiabatic losses that originate from the work that has to be done against the expanding shell (see the detailed discussion in appendix E). Again, we

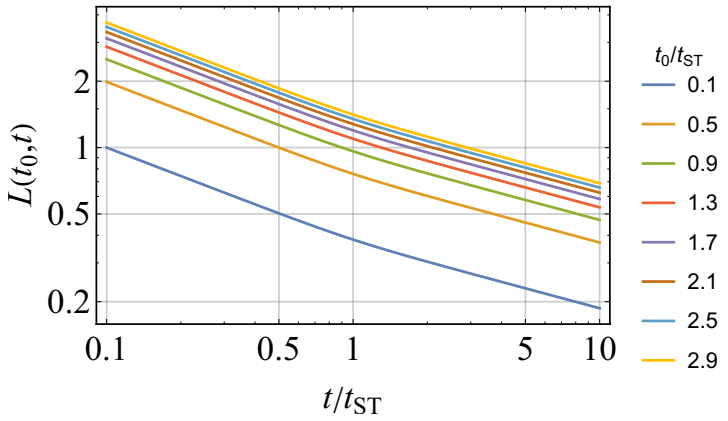

Figure 3.7: Adiabatic loss function $L(t_0, t)$ as calculated from the approximation (3.53). It is shown as a function of time t for different values of the shock crossing time t_0. Note that the required condition $L(t_0, t = t_0) = 1$ is fulfilled for all curves.

consider the ultra-relativistic limit, where the kinetic energy is close to the total energy E and can therefore be replaced in equation (E.6):

$$\frac{\mathrm{d}E}{\mathrm{d}t} = \frac{E}{L(t_0,t)} \frac{\mathrm{d}L(t_0,t)}{\mathrm{d}t}\,, \tag{3.51}$$

where the adiabatic loss function $L(t_0, t)$ is given by

$$L(t_0,t) := \left(\frac{\rho_2(t)}{\rho_2(t_0)}\right)^{1/3}. \tag{3.52}$$

However, the problem is that a model for the internal density structure at all times is needed in order to calculate $L(t_0, t)$, which can usually only be obtained from hydrodynamical simulations of the SNR – even if the initial conditions are as simple as in equation (3.4). Instead, we approximate the adiabatic loss function by just using the known shock radius as

$$L(t_0,t) \approx \left(\frac{R_{\mathrm{sh}}(t_0)}{R_{\mathrm{sh}}(t)}\right)^{1-1/\sigma}. \tag{3.53}$$

It will be demonstrated in the next section, that the right-hand side of equation (3.53), which is plotted in figure 3.7, naturally arises when the CR transport equation is solved without considering the diffusion term.

By combing adiabatic and radiative losses, we obtain the total energy loss-rate

$$\left(\frac{\mathrm{d}E}{\mathrm{d}t}\right)_{\mathrm{tot}} = \left(\frac{\mathrm{d}E}{\mathrm{d}t}\right)_{\mathrm{rad}} + \left(\frac{\mathrm{d}E}{\mathrm{d}t}\right)_{\mathrm{ad}} = -A_{\mathrm{rad}} E^2 B_{\mathrm{eff}}^2 + \frac{E}{L(t_0,t)} \frac{\mathrm{d}L(t_0,t)}{\mathrm{d}t}\,. \tag{3.54}$$

This differential equation can be solved by defining the auxiliary function $w(t) := E(t)/L(t_0, t)$ (see Reynolds, 1998). Differentiating after time yields

$$\frac{\mathrm{d}w}{\mathrm{d}t} = \frac{1}{L}\frac{\mathrm{d}E}{\mathrm{d}t} - \frac{E}{L^2}\frac{\mathrm{d}L}{\mathrm{d}t} = -\frac{A_{\mathrm{rad}} E^2 B_{\mathrm{eff}}^2}{L} + \frac{E}{L^2}\frac{\mathrm{d}L}{\mathrm{d}t} - \frac{E}{L^2}\frac{\mathrm{d}L}{\mathrm{d}t} = -A_{\mathrm{rad}} L B_{\mathrm{eff}}^2 w^2\,. \tag{3.55}$$

A straightforward integration of both sides leads to

$$\int_{t_0}^{t} -A_{\mathrm{rad}} L(t_0,t') B_{\mathrm{eff}}^2(t')\,\mathrm{d}t' = \int_{t_0}^{t} \frac{1}{w^2(t')} \frac{\mathrm{d}w(t')}{\mathrm{d}t'}\,\mathrm{d}t' \tag{3.56}$$

$$= -\int_{t_0}^{t} \frac{\mathrm{d}}{\mathrm{d}t}\left(\frac{1}{w(t')}\right)\mathrm{d}t' = \frac{1}{w(t_0)} - \frac{1}{w(t)} \tag{3.57}$$

$$\implies \quad w(t) = \left(\frac{1}{w(t_0)} + \int_{t_0}^{t} A_{\mathrm{rad}} L(t_0, t') B_{\mathrm{eff}}^2(t')\,\mathrm{d}t'\right)^{-1} . \tag{3.58}$$

Now we can re-substitute $w(t)$ and use the identity $w(t_0) = E_0$:

$$E(t) = \frac{L(t_0,t)E_0}{1 + A_{\mathrm{rad}}\,E_0 \int_{t_0}^{t} L(t_0,t')B_{\mathrm{eff}}^2(t')\,\mathrm{d}t'} = \frac{L(t_0,t)E_0}{1 + E_0\,I(t_0,t)}\,, \tag{3.59}$$

where the integral in the denominator was abbreviated as

$$I(t_0,t) \coloneqq A_{\mathrm{rad}} \int_{t_0}^{t} L(t_0,t')B_{\mathrm{eff}}^2(t')\,\mathrm{d}t' \ . \tag{3.60}$$

Although t_0 was introduced just as an arbitrary initial time (integration constant), from now on it will be associated with the time $t_0(r,t)$ when the plasma layer located at time t in position r was shocked – an important quantity that already appeared in the last section when the amplified downstream magnetic flux density was calculated.

Following Morlino and Celli (2021), we write the distribution function as a function of energy instead of momentum, which can be achieved by a simple variable substitution.[3] This choice is more convenient, because the total loss rate 3.54 is expressed in terms of energy. The interpretation of $t_0(r,t)$ as the time when a plasma element was shocked implies that

$$f(r,E,t)\big|_{t=t_0} = f(R_{\mathrm{sh}}(t_0), E_0, t_0) = f_{\mathrm{sh}}(E_0,t_0)\,. \tag{3.61}$$

From particle conservation in phase space one can then determine the electron spectrum at an arbitrary time t:

$$f(r,E,t)\,\mathrm{d}E\,\mathrm{d}V = \left(f(r,E,t)\,\mathrm{d}E\,\mathrm{d}V\right)\big|_{t=t_0} = f_{\mathrm{sh}}(E_0,t_0)\,\mathrm{d}E_0\,\mathrm{d}V_0\ . \tag{3.62}$$

By inverting equation (3.59) we find the "energy ratio" (under the condition that $L(t_0,t) - EI(t_0,t) > 0$)

$$E_0 = \frac{E}{L(t_0,t) - EI(t_0,t)} \quad \implies \quad \frac{\mathrm{d}E_0}{\mathrm{d}E} = \frac{L(t_0,t)}{(L(t_0,t) - EI(t_0,t))^2}\,. \tag{3.63}$$

Since both E and E_0 are positive, the fist equation implies that $L(t_0,t) - EI(t_0,t) > 0$. On the other hand, the "volume ratio" can be expressed in terms of the adiabatic loss function:

$$\frac{\mathrm{d}V_0}{\mathrm{d}V} = \frac{\rho}{\rho_0} = L(t_0,t)^3\,. \tag{3.64}$$

Therefore, the spectrum of confined electrons is

$$f_{\mathrm{conf}}(r,E,t) = f_{\mathrm{sh}}(E_0,t_0)\,\frac{\mathrm{d}E_0}{\mathrm{d}E}\,\frac{\mathrm{d}V_0}{\mathrm{d}V} \tag{3.65}$$

[3] See equation (C.17) in appendix C. However, here we just write the distribution function in energy space as $f(r,E,t)$ (without a tilde), because no confusion with $f(r,p,t)$ should arise.

$$= f_{\rm sh}\left(\frac{E}{L(t_0,t)-EI(t_0,t)},t_0\right)\frac{L(t_0,t)}{(L(t_0,t)-EI(t_0,t))^2}\,L(t_0,t)^3\,, \tag{3.66}$$

if $E < L(t_0,t)/I(t_0,t)$ and t_0 is again interpreted as the function $t_0(r,t)$. In the case of CR protons, where radiative losses are negligible and only adiabatic effects have to be considered, we simply set $I(t_0,t) = 0$ in the above equation, because $\dot{E}_{\rm rad} = 0$ if and only if $B_{\rm eff} = 0$, implying that $I(t_0,t) = 0$.

3.6 Contributions to the overall CR spectrum

In this section we bring together all ingredients that were discussed so far and describe how the final CR spectrum of a SNR, which will be released into the ISM, is obtained according to the analytical model of Morlino and Celli (2021). The total spectrum of cosmic rays that are injected into the ISM by a supernova remnant is the sum of two contributions:

1. Cosmic rays that are confined within the SNR due to strong scattering at self-generated MHD turbulence. They can only be released (i.e. escape upstream) if their momenta are high-enough to overcome this diffusion barrier, which happens at latest at the beginning of the snowplough phase (by assumption). However, since the shock is constantly decelerating after the Sedov-Taylor phase starts, not only its efficiency for particle acceleration declines, but also the threshold CR momentum where escape is possible. On the other hand, during confinement CRs will undergo a number of energy-loss mechanisms. In fact, adiabatic losses will affect both protons and electrons, whereas the latter ones also suffer significant radiative losses.

2. A flux consisting of high-energy particles that permanently escape from the precursor (with momenta around $p_{\rm max}(t)$), because they cannot be confined within the remnant. This "precursor contribution" makes up the high-energy tail of the final spectrum and is absolutely crucial for the supernova paradigm, because if all particles were confined within the remnant and would suffer significant losses one would require an extreme magnetic field amplification and efficiency in order to be able to accelerate CRs to PeV energies. This energy argument was emphasized in Cristofari *et al.* (2020, 2021), but the detailed microphysics of particle escape is still not fully understood (e.g. Bell *et al.*, 2013).

We first discuss the proton spectrum and then point out the differences with respect to electrons. By following Celli *et al.* (2019) we ignore diffusion for confined protons, which is a good approximation if the diffusion length is smaller than the SNR size, which is a necessary condition for confinement. The CR transport equation then simplifies to

$$\frac{\partial f_{\rm conf}}{\partial t} + u\frac{\partial f_{\rm conf}}{\partial r} = \frac{1}{r^2}\frac{\partial (r^2 u)}{\partial r}\frac{p}{3}\frac{\partial f_{\rm conf}}{\partial p} \tag{3.67}$$

and has the solution

$$f_{\rm conf}(r,p,t) = f_{\rm sh}\left(\left(\frac{R_{\rm sh}(t)}{R_{\rm sh}(t_0(r,t))}\right)^{1-1/\sigma} p, t_0(r,t)\right)\Theta(R_{\rm sh}(t)-r)\,\Theta\big(p_{\rm max,int}(r,t)-p\big)\,, \tag{3.68}$$

where the two Θ-functions ensure that only particles with $r < R_{\rm sh}(t)$ and $p < p_{\rm max,int}(r,t)$ contribute to the confined spectrum. The maximum internal momentum $p_{\rm max,int}(r,t)$ is obtained

from the maximum momentum at time $t_0(r,t)$ (when the plasma layer at time t and position r was shocked) diminished by adiabatic losses that occurred between t_0 and t:

$$p_{\mathrm{max,int}}(r,t) = p_{\mathrm{max}}(t_0(r,t))\left(\frac{R_{\mathrm{sh}}(t)}{R_{\mathrm{sh}}(t_0(r,t))}\right)^{-(1-1/\sigma)} = p_{\mathrm{max}}(t_0(r,t))L(t_0(r,t),t)\,. \tag{3.69}$$

In the last step we used the approximation for the adiabatic loss function that is motivated by the solution of the simplified transport equation (3.67) and was already introduced in equation (3.53). The distribution function f_{sh} at the shock front can be obtained explicitly by combining equations (3.20) and (3.25):

$$f_{\mathrm{sh}}(p,t) = \frac{3\xi_{\mathrm{CR}}\rho_{\mathrm{amb}}v_{\mathrm{sh}}^2}{4\pi c(m_{\mathrm{p}}c)^4\Lambda(\alpha,t)}\left(\frac{p}{m_{\mathrm{p}}c}\right)^{-\alpha}\exp\left(-\frac{p}{p_{\mathrm{max},0}(t)}\right)\Theta(p-p_{\mathrm{inj}})\,. \tag{3.70}$$

The second contribution to the total CR spectrum, namely from particles escaping upstream at the shock precursor region, results from the steady-state solution of the CR transport equation in plane-shock approximation and with a spatially constant diffusion coefficient $D(p,t)$:

$$f_{\mathrm{prec}}(r,p,t) = f_{\mathrm{sh}}(p,t)\,\exp\left(-\frac{v_{\mathrm{sh}}(t)}{D_1(p,t)}(r-R_{\mathrm{sh}}(t))\right) \qquad \text{at } r \geq R_{\mathrm{sh}}(t)\,. \tag{3.71}$$

This was already obtained in equation (2.14), where the integral in the exponent is of course trivial. Amato and Blasi (2005) present a solution (in implicit form) for the more general case, where neither the fluid velocity field $u(x)$ nor the diffusion coefficient $D(x,p,t)$ are independent of position. However, it is also demonstrated that even for this more general case the distribution function can be approximated in a similar way as above. Another convenient approximation is to replace the exponential factor by a delta distribution (cf. Celli *et al.*, 2019):

$$f_{\mathrm{prec}}(r,p,t) \approx f_{\mathrm{sh}}(p,t)\,\delta_{\mathrm{D}}\left(-\frac{v_{\mathrm{sh}}(t)}{D_1(p,t)}(r-R_{\mathrm{sh}}(t))\right) \tag{3.72}$$

$$= f_{\mathrm{sh}}(p,t)\,\frac{D_1(p,t)}{v_{\mathrm{sh}}(t)}\,\delta_{\mathrm{D}}(r-R_{\mathrm{sh}}(t))\,. \tag{3.73}$$

Physically, this can be interpreted as the momentary distribution function of cosmic rays, which are accelerated at the shock and concentrated in a precursor around $r = R_{\mathrm{sh}}(t)$ with thickness $l_{\mathrm{diff}} = D_1(p,t)/v_{\mathrm{sh}}(t)$ (diffusion length). Finally, the total momentum space density $N(p)$ of cosmic rays that are injected into the ISM by a supernova remnant is the sum of both contributions, namely (1) an escape flux of high-energy particles with released at the precursor and (2) confined particles that are released after the escape time (3.28) from a spherical volume with radius $R_{\mathrm{esc}}(p) \coloneqq R_{\mathrm{sh}}(t_{\mathrm{esc}}(p))$:

$$\begin{aligned} N(p) = N_{\mathrm{conf}}(p) + N_{\mathrm{prec}}(p) &= \int_0^{R_{\mathrm{esc}}(p)} \left(f_{\mathrm{conf}}(r,p,t_{\mathrm{esc}}(p)) + f_{\mathrm{prec}}(r,p,t_{\mathrm{esc}}(p))\right) 4\pi r^2\,\mathrm{d}r \\ &\approx \int_0^{R_{\mathrm{esc}}(p)} f_{\mathrm{conf}}(r,p,t_{\mathrm{esc}}(p))\,4\pi r^2\,\mathrm{d}r + 4\pi R_{\mathrm{esc}}^2(p)\,\frac{D_1(p,t_{\mathrm{esc}}(p))}{v_{\mathrm{sh}}(t_{\mathrm{esc}}(p))}\,f_{\mathrm{sh}}(p,t_{\mathrm{esc}}(p))\,. \end{aligned} \tag{3.74}$$

We now come to the differences between electron and proton spectrum. As already mentioned, electrons suffer stronger energy losses, especially through synchrotron emission, while the energy

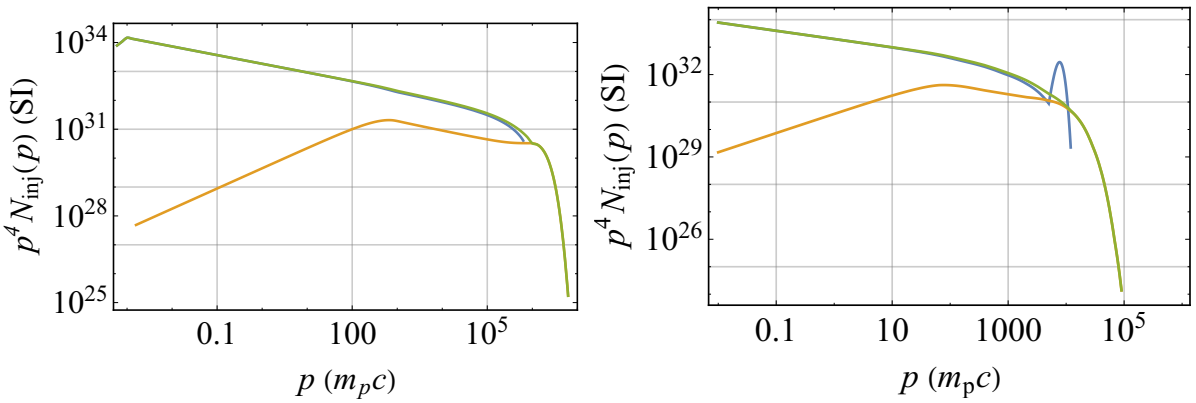

Figure 3.8: Final spectra of CR protons (left) and electrons (right) that are released into the ISM by a supernova of type Ia (the bump in the electron spectrum is a numerical artefact). Note that three lines with different colours are used to distinguish the individual components of the spectra: (1) the high-energy precursor contribution is orange and (2) the cosmic rays, which have been trapped in the remnant's inside and are finally released after suffering energy losses, are represented by the blue line. Last but not least, (3) the total spectrum, which is the sum of both contributions, is shown in green

decrease of confined protons is almost purely adiabatically due to the remnant's expansion. Moreover, the spectral cut-off for electrons, where the power-law turns into a rapid decline, occurs at lower energies than for protons. This is expected from equation (3.54), since they cool faster than protons with the same initial energy. Despite these considerable differences near the cut-off at the highest energies, it should not be forgotten that the spectral shape of electrons and protons resembles a universal power-law ranging from the injection energy up to a few TeV, which is indeed expected from DSA.

Apart from that, we also have to take the different normalization of the electron spectrum into account. The simplest approach is to introduce the electron-to-proton ratio as a free parameter $K_{\rm ep}$. If we were merely interested in the qualitative shape of the CR spectra of electrons and protons, we could simply set $K_{\rm ep} = 1$ and ignore this aspect completely. However, since the proposed CR model should be implemented in large-scale simulation, the energy content actually matters. We therefore choose the following simple approach for the electron spectrum at the shock front:

$$f_{\rm e,sh}(p,t) = K_{\rm ep}\,\frac{3\xi_{\rm CR}\rho_{\rm amb}v_{\rm sh}^2}{4\pi c(m_{\rm p}c)^4\Lambda(\alpha,t)}\left(\frac{p}{m_{\rm p}c}\right)^{-\alpha}\exp\left(-\frac{p}{p_{\rm max,e}(t)}\right)\Theta(p-p_{\rm inj})\,. \tag{3.75}$$

As pointed out in Zirakashvili and Aharonian (2007) the exact analytical solution for the electron distribution accelerated at a non-relativistic stationary shock behaves as $f_{\rm e,sh}(p) \propto p^{-\alpha}$ and $f_{\rm e,sh}(p) \propto p^{1/2}\,\exp\left(-p^2/p_{\rm max,e}^2\right)$ at low and high energies, respectively, where in the latter case the super exponential cut-off of course dominates over the positive (!) power-law slope. Although both solutions can be combined through an analytical interpolation, we will use the simpler distribution function from above. For an implementation of the more involved approach in a spectral CR model of SNRs see Cristofari *et al.* (2021). For a model, where the normalization $K_{\rm ep}$ depends on the shock velocity see (Morlino and Celli, 2021). Qualitatively, equation (3.75) looks very similar to the proton spectrum (3.70) with two exceptions, namely (1) the constant ratio $K_{\rm ep}$ and (2) the different maximum momentum $p_{\rm max,e}$ that defines the cut-off and is defined as

$$p_{\rm max,e}(t) = \min\left[p_{\rm max,0}(t), E_{\rm max,e}(t)/c\right], \tag{3.76}$$

where $p_{\mathrm{max},0}(t)$ is the time-limited maximum momentum at the shock (cf. equation 3.26) and $E_{\mathrm{max,e}}(t)$ is the loss-limited maximum electron energy, which can be obtained as follows.

If the energy loss rate in the upstream region is written as $(\mathrm{d}E(t)/\mathrm{d}t)_{\mathrm{loss},1}$ and the particle resides there for a duration $\tau_{\mathrm{res},1}$, then the amount of energy, which the particle looses upstream during this timespan, is simply the product $\tau_{\mathrm{res},1}(\mathrm{d}E(t)/\mathrm{d}t)_{\mathrm{loss},1}$. An analogous consideration holds for the downstream region. On the other hand, the particle also gains energy at a rate $(\mathrm{d}E(t)/\mathrm{d}t)_{\mathrm{acc}}$ both upstream and downstream (i.e. over a time span $\tau_{\mathrm{res},1}+\tau_{\mathrm{res},2}$). The particle cannot be accelerated further once the energy gain balances the losses. Mathematically, this condition reads (Blasi, 2010):

$$(\tau_{\mathrm{res},1}+\tau_{\mathrm{res},2})\left(\frac{\mathrm{d}E}{\mathrm{d}t}\right)_{\mathrm{acc}} = \tau_{\mathrm{res},1}\left(\frac{\mathrm{d}E}{\mathrm{d}t}\right)_{\mathrm{loss},1} + \tau_{\mathrm{res},2}\left(\frac{\mathrm{d}E}{\mathrm{d}t}\right)_{\mathrm{loss},2} \quad | \cdot E^{-1} \tag{3.77}$$

$$\Longrightarrow \quad (\tau_{\mathrm{res},1}+\tau_{\mathrm{res},2})\tau_{\mathrm{acc}}^{-1} = \tau_{\mathrm{res},1}\tau_{\mathrm{loss},1}^{-1} + \tau_{\mathrm{res},2}\tau_{\mathrm{loss},2}^{-1} \tag{3.78}$$

$$\Longleftrightarrow \quad \tau_{\mathrm{acc}} = \frac{\tau_{\mathrm{res},1}+\tau_{\mathrm{res},2}}{\tau_{\mathrm{res},1}/\tau_{\mathrm{loss},1}+\tau_{\mathrm{res},2}/\tau_{\mathrm{loss},2}}\,. \tag{3.79}$$

In the first step both sides of the equation were divided by the particle energy E and in the second step we used the definition (3.50) of the loss time (the acceleration time is defined analogously). One can now insert the acceleration time $t_{\mathrm{acc}} = 8D_1(p,t)/u_{\mathrm{sh}}^2$ and the loss times

$$\tau_{\mathrm{loss},1} = \left(A_{\mathrm{rad}}E(B_{1,\mathrm{tot}}^2+B_{\mathrm{eq}}^2)\right)^{-1}, \quad \tau_{\mathrm{loss},2} = \left(A_{\mathrm{rad}}E(B_{2,\mathrm{tot}}^2+B_{\mathrm{eq}}^2)\right)^{-1}. \tag{3.80}$$

in order to obtain the maximum loss-limited energy $E_{\mathrm{max,e}}(t)$. As shown in Morlino and Celli (2021), the final result is

$$\frac{E_{\mathrm{max,e}}(t)}{m_{\mathrm{e}}c^2} = \sqrt{\frac{(\sigma-1)r_{\mathrm{B}}}{\sigma\left[r_{\mathrm{B}}(1+\sigma_{\mathrm{eq}}^2)+\sigma(r_{\mathrm{B}}^2+\sigma_{\mathrm{eq}}^2)\right]}\,\frac{3ecB_0\mu_0\mathcal{F}(t)}{2\sigma_{\mathrm{T}}B_{1,\mathrm{tot}}^2(t)}}\,\frac{v_{\mathrm{sh}}(t)}{c}\,. \tag{3.81}$$

Now we have all ingredients needed for the electron distribution function at the shock as given by equation (3.75). With this and the known expressions for $L(t_0,t)$ and $t_0(r,t)$ the spectrum of confined particles (equation 3.66) can be computed. In addition, the electron precursor spectrum has the same functional form as in the case of protons. Therefore, the total electron spectrum can also be obtained from equation (3.74) after making the aforementioned modifications and replacing the escape time by $t_{\mathrm{esc,e}}$, which is given by

$$t_{\mathrm{esc,e}}(E) = \min\left[t_{\mathrm{SP}}, \max\left[t_{\mathrm{esc},0}, t_{\mathrm{esc}}(E/c)\right]\right]\,. \tag{3.82}$$

Hence, the expression for the electron escape time is slightly more complicated than for protons, because several things have to be taken into account. First of all, acceleration stops at latest at the beginning of the snowplough phase (first bracket). Secondly, various loss mechanisms might delay the time $t_{\mathrm{esc},0}$, when the first electrons start escaping from the SNR or, in other words, when the maximum permitted electron energy $E_{\mathrm{max,e}}(t)$ begins to exceed the maximum energy $p_{\mathrm{max},0}(t)c$ of particles accelerated and confined at the shock:

$$E_{\mathrm{max,e}}(t_*) = p_{\mathrm{max},0}(t_*)c \quad \text{for } t_* = t_{\mathrm{esc},0}\,. \tag{3.83}$$

This explains the second bracket in the definition above.

The final CR spectra for electrons and protons are shown in figure 3.8 for the case of a type Ia supernova. One clearly sees that they resemble a power-law with slope α for a large range of

Table 3.2: Additional free model parameters with brief descriptions; see the main text for further details.

parameter	value	meaning
n_{ISM} (m^{-3})	10^5	mean number density of ISM
B_{ISM} (nT)	0.3	background magnetic field in the ISM
B_{eq} (nT)	0.61	magnetic field with energy density equivalent to the ISRF
ξ_{CR}	0.1	proton acceleration efficiency
α	4.3	power-law slope of CR distribution at the shock
δ	2	power-law index to model time dependence of $p_{\mathrm{max},0}(t)$
σ	4	compression ratio of the shock
p_{inj} ($m_{\mathrm{p}}c$)	10^{-3}	injection momentum
p_{M} ($m_{\mathrm{p}}c$)	10^6	maximum proton momentum at Sedov-Taylor time
K_{ep}	1	normalization constant for the electron spectrum at the shock

energies, which is only modified near the exponential cut-off. Note that for both electrons and protons the highest-energy particles all come from the precursor contribution (orange line), which demonstrates what has been claimed at the beginning of this section: without taking upstream particle escape properly into account, it would be a severe theoretical challenge to explain how supernova remnants can act as pevatrons.

Furthermore, the total kinetic energy of cosmic rays was calculated for the proton spectrum, which is given by (see appendix C and the next section for details concerning the choice of p_{inj}):

$$E_{\mathrm{tot,CR}} = \int_{p_{\mathrm{inj}}}^{\infty} 4\pi p^2 \, N(p) \left(\sqrt{(pc)^2 + (m_{\mathrm{p}}c^2)^2} - m_{\mathrm{p}}c^2 \right) \mathrm{d}p \ . \tag{3.84}$$

We obtained a value of $E_{\mathrm{tot,CR}} \approx 0.2\, E_{\mathrm{SN}}$, which is not bad compared to the standard estimate $E_{\mathrm{tot,CR}} = 0.1\, E_{\mathrm{SN}}$. However, in the above integral we used the exact expression for the relativistic kinetic energy and not the approximation $E = pc$, which would lead to completely wrong results. However, we have often employed the ultra-relativistic limit so far; see e.g. the treatment of energy losses in equation (3.54). Therefore, the calculated CR energy should not be considered as a completely self-consistent outcome of the model; instead it serves as consistency check. Besides that, the cosmic ray module in *OpenGadget3* fully relies on the assumption $E = pc$, which is wrong for proton momenta below 1 GeV/c. We will come back to this issue in chapter 4.

3.7 Constraining the model parameters

At the end of this chapter we reflect on some additional model parameters (besides those in table 3.1) and how they might be constrained or at least chosen reasonably. The benchmark values and short descriptions can be found in table 3.2. First of all, mean properties of the ISM, like particle density, magnetic field strength or energy density of the ISRF are exclusively motivated by typical observed values in the Milky Way. Of course, they are not constant throughout the galaxy, which could be taken into account by calculating several CR spectra for different (but still reasonable) sets of parameters and then using the available information in a cosmological simulation (e.g. concerning the local gas density or magnetic field) to decide which spectrum should be seeded at a given location.

Other parameters, like p_{M} and δ in equation (3.26) are simply adopted from the specific model by Morlino and Celli (2021) (in their work they also studied how changes in these two parameters

affect the final CR spectrum). We already commented that a downside of this simple recipe for $p_{\mathrm{max},0}(t)$ is that the additional free parameter $p_{\mathrm{M}} = 1$ PeV has to be introduced, whose value is just motivated by the expectation that SNRs are pevatrons. This could be remedied with the more physical (but also more complex) prescription by Cristofari *et al.* (2021), which is consistent with the development of non-resonant Bell instabilities.

The slope α is mainly motivated by results of recent particle-in-cell simulations of astrophysical shock waves indicating that the injected spectrum is steeper than the standard prediction $\alpha = 4$ from DSA (cf. Diesing and Caprioli, 2021). For the compression ratio σ we choose the standard value for strong shocks in a gas with adiabatic index $\gamma = 5/3$, but it should be kept in mind that the presence of highly relativistic particles will affect the value of γ; especially near the shock. The electron-to-proton ratio K_{ep} is set equal to one, because it is also implemented in *OpenGadget3*, where the default setting is $K_{\mathrm{ep}} = 10^{-2}$. Hence, the electron spectrum will not be rescaled until it is imported in a cosmological simulation.

Last but not least, we briefly touch upon a highly interesting model parameter that has been neglected so far, namely the injection momentum p_{inj}, which defines the lower boundary where the cosmic ray spectrum starts. As already mentioned in chapter 2, it is one of the fundamental problems of DSA to consistently describe how particles from the thermal pool can be injected into the acceleration process ("injection problem"). A standard assumption is that a small fraction of thermal particles from the tail of the Maxwellian[4] velocity distribution reach high enough energies to be able to take part in DSA. This is called "thermal leakage injection" and is usually parametrized as $p_{\mathrm{inj}} = \xi_{\mathrm{inj}} p_{\mathrm{th}}$, where $p_{\mathrm{th}} = \sqrt{2 m_{\mathrm{p}} k_B T_2}$ is the downstream thermal momentum (cf. Caprioli and Spitkovsky, 2014). Usually, the coefficient lies in the range $\xi_{\mathrm{inj}} = 3$–4, because this yields $\xi_{\mathrm{CR}} = P_{\mathrm{CR}}/(\rho_{\mathrm{amb}} v_{\mathrm{sh}}^2) \approx 0.1$, which is the criterion we required in equation (3.21). Alternatively, the injection momentum can also be written as a function of the shock velocity, i.e. $p_{\mathrm{inj}} = \xi_{\mathrm{inj}} m_{\mathrm{p}} v_{\mathrm{sh}}$ (cf. Caprioli *et al.*, 2015).

[4] One should be cautious, because the shocks of supernova remnants are collisionless, so it is not a priori clear whether the shock-heated particles even have a Maxwellian velocity distribution.

4 Numerical implementation

By following the steps described in the previous chapter, one can calculate the final CR momentum space distributions $N(p)$ for CR protons and electrons that are released into the ISM by a supernova remnant. Of course, the many parameters of our model are by no means "engraved in stone" and for realistic simulations a certain variation from supernova to supernova is indeed expected. The most prominent examples are the remnant's kinetic energy and the ejecta mass, which strongly affect the maximum achievable proton energy and therefore the remnant's possibility to act as a Pevatron, which was investigated by Cristofari (2021). As mentioned before, Cristofari *et al.* (2021) proposed a crude approach to illustrate the variety in parameter space, namely to generate, for the time being, spectra for the three benchmark cases in table 3.1, which were called Ia, II and II*. This was indeed done in this Master's project. The logical next steps would be to (1) refine the CR model even more by generating dozens of spectra, each for a slightly different set of parameters and (2) include environmental properties of a given SPH particle, like ambient ISM density, background magnetic field or local radiation field, to make reasonable choices on which spectra should be seeded at a given time and location.

Since there is always room for model refinements, the question arises if this is worth the effort or just an uninteresting over-complication of the "standard approach", where supernova remnants are treated as sub-grid CR sources that inject simple power-law spectra with (exponential) cut-offs at a minimum and maximum momentum and a normalization such that the integrated CR energy is $0.1\, E_{\mathrm{SN}} = 10^{43}$ J. On the one hand, the calculated spectra, that were shown in the last chapter, closely resemble a power-law over a large momentum range. In fact, only at the highest momenta close to the exponential cut-off, subtle spectral features become noticeable. Hence, a first guess would be that large-scale simulations with our CR model only differ quantitatively from results in the scientific literature, but not qualitatively. On the other hand, the model introduced in this thesis is largely based on first principles, so it is much more difficult to "cheat" by simply shifting the cut-offs or changing the spectrum's normalization in order to obtain the desired simulation output. This was nicely illustrated by calculating the total CR energies of the final spectra, which were close to the expected $0.1\, E_{\mathrm{SN}}$, although this was not introduced by hand! So from this point of view, one could argue that state-of-the-art simulations used to investigate CR feedback on galaxies should incorporate the most realistic SNR spectra, that can currently be constructed. Hence, we are left with the question how much sense it makes to implement a CR model, which is still strongly simplified compared to reality, but quite sophisticated compared to usual numerical approaches, in a cosmological simulation code. Unfortunately, this cannot be answered in this Master's thesis, since test runs of galaxies using the proposed recipe for CRs from SNRs, were not successful yet. However, the corresponding bug will be fixed in the near future to shed more light on this issue. In the remainder of this chapter, we will therefore present all preliminary results and describe some numerical aspects of this thesis project. A completed test run of a Milky-Way-like galaxy with the pre-existing supernova seeding of *OpenGadget3* will also be shown in order to illustrate the further procedure.

4.1 Cosmic ray model in *OpenGadget3*

The cosmological SPH N-body code *OpenGadget3* is a derivative of *GADGET-2* (GAlaxies with Dark matter and Gas intEracT), as described by Springel (2005), and contains by now many modules describing sub-grid physics, like star formation, supernova feedback, magnetic seeding, chemical reaction networks, AGNs and, last but not least, cosmic rays. For a detailed description of the current cosmic ray model in *OpenGadget3* and accompanying simulations of an idealized galaxy cluster merger, we refer to Böss *et al.* (2023). At its heart lies *CRESCENDO* (Cosmic Ray Evolution with SpeCtral Electrons aND prOtons), which is an on-the-fly Fokker–Planck solver to evolve the distribution functions of CR protons and electrons within every resolution element of the simulation. As in the previous chapter, the CR distribution function is assumed to be isotropic in momentum, so its temporal evolution can be described by

$$\frac{\mathrm{D}f(\mathbf{x},p,t)}{\mathrm{D}t} = \left(\frac{1}{3}\boldsymbol{\nabla}\cdot\mathbf{u}\right) p\frac{\partial f(\mathbf{x},p,t)}{\partial p} + \frac{1}{p^2}\frac{\partial}{\partial p}\left(p^2\sum_l b_l f(\mathbf{x},p,t)\right) + Q(\mathbf{x},p,t)\,, \tag{4.1}$$

where the left-hand side represents the advective time derivative of the distribution function $f(\mathbf{x},p,t)$ (in its Lagrangian form) and the terms on the right-hand side represent (1) momentum advection related to adiabatic compression/expansion, (2) continuous energy loss processes (like synchrotron and inverse Compton losses of electrons) and (3) CR injection through sources (like supernova remnants). Other effects, like spatial transport (including diffusion), momentum diffusion and catastrophic losses are not yet included in *CRESCENDO*.

The basic idea is to assign two distribution functions to each SPH gas particle (one for protons and one for electrons) and then evolve them over time according to the (simplified) transport equation above. Numerically, a distribution function is represented as a piecewise power-law in momentum space

$$f(p) = f_j\left(\frac{p}{p_j}\right)^{-\alpha_j}, \quad j = 1,\ldots,N_{\mathrm{bins}}\,, \tag{4.2}$$

where N_{bins} is the number of bins (this is a parameter that has to be specified before a simulation is started). In the test simulations that were carried out for this Master's thesis we typically set $N_{\mathrm{bins}} = 12$ for protons and $N_{\mathrm{bins}} = 48$ for electrons. In logarithmic momentum space all bins have the same width and typically range from $p_{\mathrm{min}} = 0.1\,m_i c$ to $p_{\mathrm{max}} = 10^5\,m_i c$, where m_i is either proton or electron mass. The lower momentum boundary is fixed and open, which enables particles to transition from relativistic energies to the thermal background if they loose enough energy through cooling. On the other hand, the upper boundary is closed and must therefore be able to move, which requires updating p_{max} in every time step. This approach is motivated by allowing particles to gain additional energy (beyond the initial boundary) and avoiding an artificial pile-up in the last momentum bin.

The norms f_j and slopes α_j are updated in each time step by calculating both the total number N_j (not to be confused with momentum space density $N(p)$) and energy E_j of cosmic rays for each bin, which is the so-called "two-moment approach". For this, the corresponding integrals are solved (see also appendix C):

$$N_j = \frac{1}{\rho}\int_{p_j}^{p_{j+1}} 4\pi p^2 f(p)\,\mathrm{d}p = \frac{4\pi f_j p_j^3}{\rho}\frac{\left(\left(\frac{p_{j+1}}{p_j}\right)^{3-\alpha_j} - 1\right)}{3-\alpha_j}\,, \tag{4.3}$$

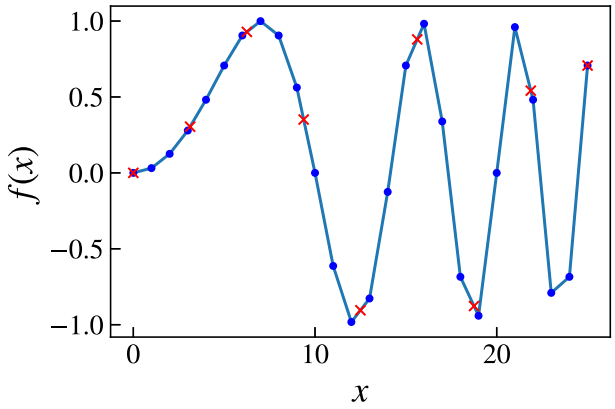

Figure 4.1: Testcase for the discretization routine, which is applied to the oscillating function $f(x) = \sin\left(\pi(0.1 \cdot x)^2\right)$. The blue points are 26 tabulated data pairs $\{x_j, f(x_j)\}_{j=1,\ldots,26}$ belonging to the test function, which are connected through straight lines (a simple linear interpolation). The red crosses are the new pairs $\{x_k, f(x_k)\}_{k=1,\ldots,10}$ corresponding to a decomposition of the x-range into 10 equal-width bins. As expected, the crosses lie on the interpolation curve.

$$E_j = \frac{1}{\rho} \int_{p_j}^{p_{j+1}} 4\pi c p^3 f(p)\, \mathrm{d}p = \frac{4\pi c f_j p_j^4}{\rho} \frac{\left(\left(\frac{p_{j+1}}{p_j}\right)^{4-\alpha_j} - 1\right)}{4 - \alpha_j} \,. \tag{4.4}$$

The integrals are divided by the density ρ of the SPH particle, because CR energies and numbers are expressed per unit mass in *OpenGadget3* due to the Lagrangian reference frame in which the equations are discretized. Their simple analytical solution is then used for updating norms and slopes. Therefore, in *CRESCENDO* the spectrum is described by the four parameters f_j, α_j, N_j and E_j, where each of them is numerically represented by a one-dimensional array with length N_{bins}. By contrast, the array of momentum boundaries p_j must of course have length $N_{\mathrm{bin}} + 1$.

A caveat is that in all calculations the assumption $E = E_{\mathrm{kin}} = pc$ is used, which leads to a simple solution of the energy integral, but only holds in the ultra-relativistic limit. For example, a particle with mass m and momentum $p = 0.1\, mc$ has a speed of only $0.01\, c$, which is hardly relativistic. As a consequence, in *CRESCENDO* the thermal pool of gas particles and the high-energy cosmic rays are not connected through a "bridge" of suprathermal, mildly relativistic particles, but treated as two separate fluids. All these limitations should be kept in mind for the test simulation shown below.

Although Böss *et al.* (2023) mainly focussed on shock waves as sources of CRs, *OpenGadget3* also contains a simplified recipe for CR seeding by supernova remnants, which is coupled to the star formation model (see below). Whenever a supernova explodes, a simple power-law spectrum with slope $\alpha = 4.4$ and initial cut-offs at p_{min} and p_{max} (with the same values as above) is injected. The normalization of the spectrum is chosen such that the total CR proton energy equals the standard value of $0.1\, E_{\mathrm{SN}}$. Since the more advanced spectra have not been successfully included yet in a large-scale simulation, we will show results from a test run of a Milky-Way-like galaxy that was carried out by using this simpler model.

4.2 Sub-grid implementation of CR spectra

Roughly speaking, the numerical aspect of this thesis consists of two parts. Firstly, an implementation of the model described in chapter 3 is run in order to produce spectra for CR protons and electrons for different types of supernovae. Secondly, those spectra are then saved in data

files, which have to be processed by the newly developed module for improved CR seeding in *OpenGadget3*.

First of all, a given CR spectrum is calculated by running a notebook that is heavily based on the template kindly provided by Giovanni Morlino and used by Morlino and Celli (2021). More precisely, for a given supernova type (and the corresponding set of parameters) the momentum space distribution $N(p)$ is calculated for a discrete set of momenta and then interpolated with cubic splines between successive data points. The interpolating function can then be used to generate an arbitrarily fine discretization of $N(p)$, i.e data pairs of the form

$$\left\{ \lg\left(\frac{p_j}{m_i c}\right),\ \lg\left(\frac{N(p_j)}{(m_i c)^{-3}}\right) \right\}_{j=1,\dots,N_{\mathrm{dat}}} . \tag{4.5}$$

Note that N_{dat} is the given number of data points for which the condition $N_{\mathrm{dat}} > N_{\mathrm{bins}}$ should hold (for test runs $N_{\mathrm{dat}} \gtrsim 100$ is already sufficient). For convenience, $m_i c$ is selected as momentum unit, so that the logarithms of p_j and $N(p_j)$ can be expressed as dimensionless quantities. Again, m_i either stands for the proton or electron mass, depending on the type of spectrum that shall be computed.

Without doubt, this first numerical part of the thesis involves a large amount of theory and a combination of different approaches from the literature. The second part is more technical in nature and consists of modifications of the *OpenGadget3* source code. The new module for CR seeding mainly consists of two small routines, namely one that reads the columns from the text file and saves them in arrays and a second one that converts the input data into a form that can be processed by *CRESCENDO*. For this, a routine is required that accepts the tabulated data and the given momentum boundaries as input and returns a more coarsely discretized spectrum, whose number of momentum bins corresponds to the simulation settings. The new spectrum is obtained from the input data through a simple linear interpolation of the data points in log-log space. This works, because the input values from the text file are already logarithmic quantities and the piecewise power-law becomes a piecewise linear function in log-log space. This linear interpolation was tested for a oscillating function, where the result can easily be checked for consistency (see figure 4.1). The new discretization consists of the pairs

$$\left\{ \lg\left(\frac{p_k}{m_i c}\right),\ \lg\left(\frac{N(p_k)}{(m_i c)^{-3}}\right) \right\}_{k=1,\dots,N_{\mathrm{bins}}} . \tag{4.6}$$

and is used to calculate CR numbers N_k and energies E_k that are needed by *CRESCENDO* to evolve the CR spectrum.

Although both routines seemed to work fine at the time of writing this thesis, no successful galaxy simulation could be done due to some programming error that must have occurred during the integration of the new module in *CRESCENDO*. We will therefore explain some further numerical aspects in the remainder of this section and show a test simulation in the next chapter, that still contains the old CR seeding model.

One prominent issue, that always arises when quantitative results are desired at the end of a simulation, is the correct usage of physical units. In most scientific articles on CR spectra of supernovae only the shape and cut-offs are discussed, but not the actual normalization. However, this aspect is crucial for our implementation, because we need to know the correct energy content of cosmic rays. Besides that, the quantity we obtain from our CR model is not the distribution function $f(\mathbf{x}, p, t)$, but the time-independent momentum space density $N(p)$ that was calculated through a spatial integration over $f(\mathbf{x}, p, t)$ up to the escape radius according to equation (3.74). These quantities have units

$$[f(\mathbf{x}, p, t)] = [x]^{-3}\,[p]^{-3}\,, \quad [N(p)] = [p]^{-3}\,, \tag{4.7}$$

and therefore the integrals (4.3) and (4.4) can be rewritten by replacing $f(p)$ by $N(p)$ and dividing through the SPH particle's mass instead of its density. If one would be interested in the CR number density $n(\mathbf{x})$, the following simple assumption could be made: If the supernova releases a CR spectrum into the ISM that is described by $N(p)$, then those particles propagate freely, but diffusively and without adiabatic losses so that they distribute over the SPH particle's volume. When this happens sufficiently fast, i.e. during one time step, all cosmic rays will be distributed uniformly over the entire volume so dividing $N(p)$ by this volume leads to a first approximation of $f(p)$. Integrating this over momentum yields the constant CR density n. However, assuming a Galactic diffusion coefficient of (cf. Celli *et al.*, 2019)

$$D(p) = 10^{24}\left(\frac{pc}{10\ \mathrm{GeV}}\right)^{1/3}\ \mathrm{m^2\ s^{-1}}\,, \tag{4.8}$$

a 1 PeV particle released during the early stages of SNR evolution would diffuse over a length $l_{\mathrm{diff}} = \sqrt{2Dt} \approx 740$ pc for a propagation time of 50 kyr (the typical timescale after which the snowplough phase starts). Since this length scale is already ten times larger than the minimum hydrodynamical smoothing length in the galaxy simulation shown in the next chapter, one should be cautious with this simplistic approach.

At the end of this section we also note that once the new CR module is running, it can easily be extended to include a reasonable variety of different supernovae, which we briefly touched upon in the introduction to this chapter. For example, one could tabulate 10 type II SNe with slightly different parameters and store them in one text file. Then one of those spectra could be picked for seeding based on either a random approach or on the local galactic environment of the supernova event. Moreover, it was so far only attempted to couple the CR seeding to the simple star formation model by Springel and Hernquist (2003) that only includes core-collapse SNe and will briefly be described in the next section. However, *OpenGadget3* also has a more advanced model, as proposed by Tornatore *et al.* (2007), which also takes Ia SNe into account and would therefore be more suitable to the variety of tabulated CR spectra.

4.3 Coupling supernova seeding to star formation in *OpenGadget3*

In this section we will briefly and qualitatively describe the simplest star formation model available in *OpenGadget3*, which is an implementation of the well-known Springel-Hernquist model (see Springel and Hernquist, 2003, for an extensive description and simulations of small-scale, isolated galaxies). This is insofar important for this Master's thesis, as the model incorporates supernova feedback to which the CR module can be linked.[1] The basic idea is to describe global properties of a multiphase interstellar medium with a sub-resolution model that only uses spatially averaged properties of the ISM, namely the mass density and the internal energy per unit mass. Baryonic matter is assumed to consist of three components, namely stars, a hot phase of the ISM and cold molecular clouds that enable star formation. In *OpenGadget3* there indeed exist separate particle types for stars and gas, but the distinction between a hot and cold phase is made implicitly through a "cold fraction" and a "hot gas temperature" that are attributed to every gas particle.

The temporal evolution of these quantities is described by a set of coupled ordinary differential equations. More precisely, the density of cold molecular clouds decreases, because (1) gas is

[1] Strictly speaking, CR seeding from supernova remnants is coupled to magnetic dipole seeding from SNe (cf. Beck *et al.*, 2013), which itself is coupled to the Springel-Hernquist model. However, this is merely a numerical aspect that is not significant for the further content of this thesis.

converted into stars on a characteristic timescale, which is effectively the only free parameter of the whole model, and (2) some cold gas is reheated by supernova feedback and returns to the hot phase, whose density therefore increases by the same amount. Moreover, radiative energy losses of the hot gas turn it into cold clouds, which is described by a cooling function. For the onset of this thermal instability, which is necessary for creating clouds and continuing star formation, the hot gas has to exceed a certain threshold density. This criterion is observationally motivated (see references in Springel and Hernquist, 2003) and physically plausible, because the cooling power is proportional to the squared density. Last but not least, the fraction of hot gas not only increases through cloud evaporation triggered by supernova heating, but also through enrichment with supernova ejecta. The latter contribution is proportional to the fraction of newly formed stars that can undergo core-collapse supernovae, meaning that their masses lie above 8 $M_\odot$, which depends of course on the chosen initial mass function. Moreover, the stellar mass density decreases accordingly, since exploding stars are assumed to be completely destroyed and turned into hot gas; compact stellar remnants, like black holes or neutron stars, are not taken into account. In reality there is a delay between star formation and core-collapse supernovae that corresponds to the main-sequence lifetime of massive stars, which is $\lesssim 25$ Myr. However, this delay is neglected in the Springel-Hernquist model and supernovae appear "promptly" instead. This approximation is fine if self-regulation is established quickly enough, meaning that star formation is "quiescent". In the code itself for each time step an effective supernova rate is calculated in order to determine how many stars explode. If this rate drops below 1, a stochastic criterion decides if a supernova will occur or not.

At the end we also note that the Springel-Hernquist model naturally leads to an overproduction of stars in cosmological simulations, because cooling becomes very efficient in dense, low-mass haloes, which leads to an overproduction of stars and a rapid depletion of the gas reservoir (overcooling problem). To avoid this, galactic winds associated with star formation (and possibly with cosmic rays, as noted in the introduction of this thesis) are included in the model.

5 Test simulations and results

Unfortunately, the cosmic ray model proposed in chapter 3 could not be successfully implemented in *OpenGadget3* at the time when this thesis was written, which was already mentioned before. Therefore, this last chapter is a collection of simulation results, that were already obtained, and some comments on future work.

5.1 Test environment for CR seeding

In order to test the implementation of the CR seeding model, we set up a very simple environment with periodic boundary conditions, namely a box consisting of $20 \times 20 \times 20$ gas particles that are distributed on a grid with zero initial velocities. The density is chosen such that it is close to the threshold required for star formation, whereas the initial gas temperature corresponds to typical values of the hot ISM. The selected box length of 5 kpc leads to gas particle masses that are close to those in the galaxy simulation of the next section, so both simulations have a similar mass resolution. In order to increase the central gas density we place eight additional gas particles around the particle in the middle of the box. This initial setup is shown in figure 5.1

In order to demonstrate the behaviour of this test bed, we switch on the simple sub-grid model for CR injection by supernovae, which is just a power-law with slope $\alpha = 4.4$ and was already described in section 4.1. As one can see in figure 5.2, the regular grid gets destroyed over time, while the number of star particles and the CR pressure of gas particles increases. This shall merely serve as a proof of concept, but the more advanced CR seeding does not produce any CR pressure yet due to an error in the implementation. However, we are optimistic that this issue will be fixed in the near future so that the simulation of a Milky-Way-like galaxy shown in the next section can be repeated with the improved model. A significant advantage of this test bed is that one can check very quickly if the simulation produces the desired output, because it already finishes after around 10 minutes. In contrast, the galaxy simulation runs at least a few days.

5.2 Simulation of a galaxy with simple power-law seeding

In this section we show results from the simulation of a Milky-Way-like galaxy consisting of $\sim 3 \cdot 10^6$ particles (gas, dark matter, stars and one central black hole) with a total mass of 10^{12} $M_\odot$. The initial conditions were kindly provided by Ulrich Steinwandel and the settings in *OpenGadget3* were adjusted by Ludwig Böss. The simulation includes a lot of sub-grid physics, like cooling, star formation, galactic winds, magnetic field seeding and metal enrichment. Most importantly, the CR module *CRESCENDO* is active, including the simple power-law injection of cosmic rays by supernovae (cf. section 4.1). The simulation output is stored in snapshot files (using the *Gadget* file format) that are analysed with *Smac* and *g3read* (see appendix B for a detailed summary of used software and corresponding citations).

The galaxy is evolved over a total timespan of roughly 2 Gyr, which is shown in figure 5.4. Each map was created with *Smac* and shows a certain physical quantity, namely:

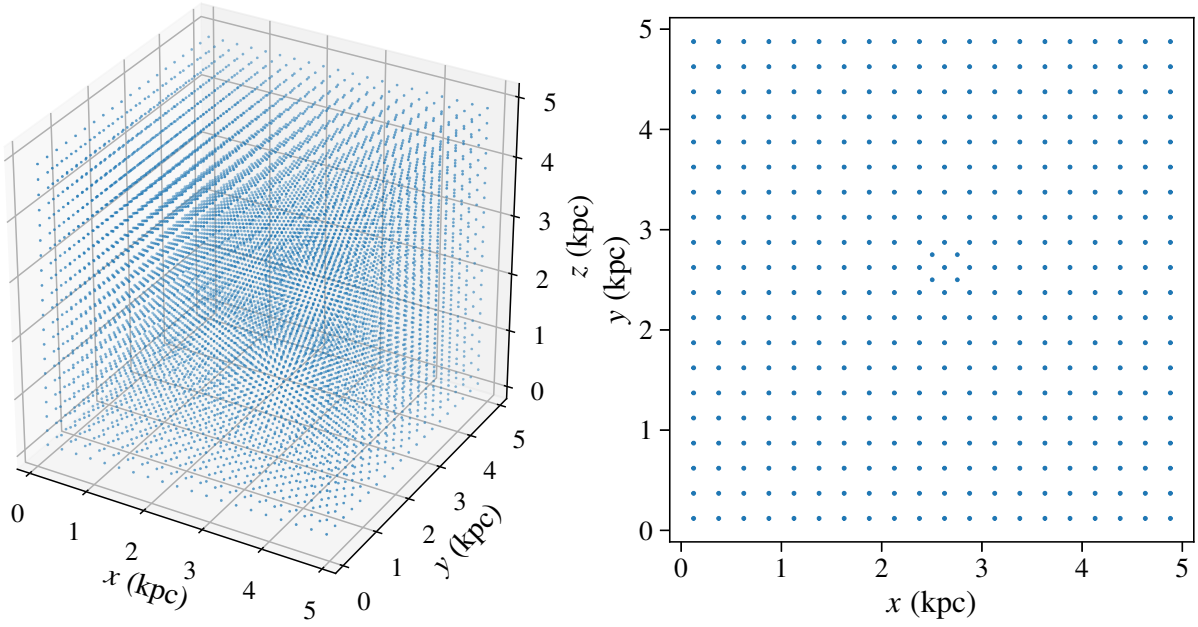

Figure 5.1: The simple initial conditions used for testing the implementation of CR seeding by supernovae consists of a box with $20 \times 20 \times 20$ gas particles at rest and a central over-density that is reached by inserting 8 additional particles. Left: Box with the initial particle distribution. Right: 2D projection with clearly visible central over-density.

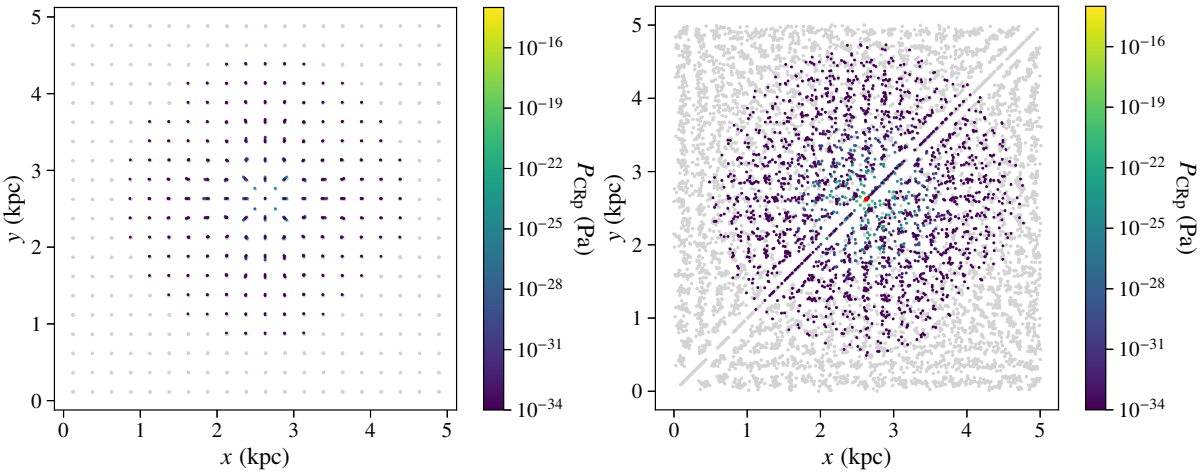

Figure 5.2: Time development of gas particle distribution (light grey dots) in our test bed. The initial regular grid (left) gets distorted over time (right), while the CR proton pressure increases (see colour bar). The eye-catching red dot in the centre is a newly formed star particle.

- Surface mass density of the gas Σ_e, which is called "electron density" in *Smac* (cf. figure 5.7)
- Magnitude of the magnetic flux density $\langle|\mathbf{B}|\rangle$ averaged along the line of sight (cf. figure 5.5)
- Temperature T averaged along the line of sight, which is called "mass-weighted" in *Smac* (cf. figure 5.8)
- Pressure of CR protons P_{CRp} (cf. figure 5.9)
- Pressure of CR electrons P_{CRe} (cf. figure 5.10)

The galaxy has a diameter of about 15 kpc (cf. figures 5.7 and 5.8), which is only half the size of the Milky Way. Therefore, this simulation should not be regarded as replica of our own galaxy; instead it serves as an advanced testcase for investigating the collective effects of sub-grid physics. The density and temperature maps reveal that the morphology changes significantly over time: The galaxy starts as a barred spiral, then develops a ring-like structure and finally reaches a quite homogenous appearance with a central bar. On the other hand, the maps of the magnetic field show how it grows in strength and spatial extent over time. At the end of the simulation the entire magnetic field is distributed over a volume far larger than that of the gas (see the size comparison in figure 5.4). The magnetic dipole seeding by supernovae is nicely illustrated by the clumpy structure in the early snapshots. During this time, the maps of CR proton and electron pressure also show local peaks that are related to the spatially discrete seeding by SNRs.

We also divided the galaxy into 25 concentric rings (radial bins), calculated the pressures of different ISM components in each of them and plotted the result in figure 5.3. The CR proton and electron pressure are directly stored in the snapshot file by the *CRESCENDO* module. As expected, the proton pressure exceeds that of electrons, which is mainly caused by the different normalizations of the distribution functions (in *OpenGadget3* we have a typical electron-proton ratio of $K_{\mathrm{ep}} = 10^{-2}$). The other three pressures are calculated from the simulation output. In particular, the thermal pressure $P_{\mathrm{th}} = (\gamma - 1)\rho u$ is obtained from the mass density ρ and the internal energy u per unit mass, where we further assumed a monatomic ideal gas with adiabatic index $\gamma = 5/3$. The magnetic pressure is calculated with the same formula as the energy density, namely $P_{\mathrm{mag}} = B^2/(2\mu_0)$. The turbulent pressure is given by $P_{\mathrm{turb}} = \rho v_{\mathrm{rms}}^2/2$, where v_{rms} is the root-mean-square velocity for gas particles within the hydrodynamical smoothing kernel. In figure 5.3 one clearly sees that an equilibrium amongst thermal, magnetic and turbulent pressure is reached at the end of the simulation for inner regions of the galaxy. Equivalently speaking, an equipartition of energy has taken place, which we touched upon in the introduction. However, this does not hold for the cosmic ray pressure any more, because *OpenGadget3* lacks the corresponding sub-grid physics describing realistic CR feedback.

We conclude this chapter with some remarks on what else could be done with the outcome of a galaxy simulation. Of course, the first thing would be to check if the improved CR spectra of supernova remnants lead to comparable results and if there are relevant quantitative differences (e.g. concerning the CR pressure). Moreover, one could compute maps of the synchrotron and γ-ray emission, where the former is caused by relativistic electrons, whereas the latter originates from hadronic interactions of CR protons with gas particles. This would indeed be very interesting, because the electromagnetic radiation can be directly associated with the emitting source, which is generally not possible for cosmic rays due to their diffusive spatial propagation (except at the highest energies). Additionally, galaxies and galaxy clusters are well-observed in the radio and γ-ray band, where the data quality is permanently increasing thanks to various observatories, like the Fermi Gamma-Ray Space Telescope, INTEGRAL (International

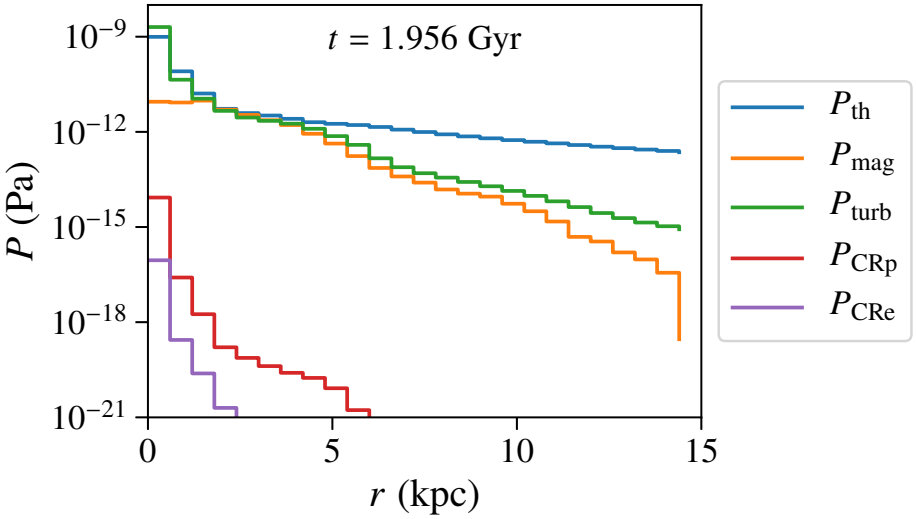

Figure 5.3: Radial profile for different pressures in the last snapshot of the galaxy simulation. Note that within the inner galactic region an equipartition amongst thermal, magnetic and turbulent pressure is reached.

Gamma-Ray Astrophysics Laboratory), HAWC (High-Altitude Water Cherenkov Observatory), LHAASO (Large High Altitude Air Shower Observatory), CTA (Cherenkov Telescope Array) for high energies or MeerKAT, SKAO (Square Kilometre Array Observatory), ngVLA (Next Generation Very Large Array) for the radio band.

Therefore, a good consistency test for the improved CR model would be to check if the simulated synchrotron and γ-ray emission is still compatible with observations or if some significant tensions arise. For example, until today it has not been possible to identify a single galaxy cluster that shows γ-ray emission from CR protons, whereas the synchrotron radiation of CR electrons is well-known. In fact, γ-ray observatories were only able to provide upper limits for the expected γ-ray fluxes, which are already quite low. From a theoretical point of view, it is hard to explain how electrons can be accelerated to energies high enough such that their synchrotron emission is observable, while protons are not accelerated efficiently enough in the same environment to cause detectable γ-rays. The current explanations and observational data concerning this "missing γ-ray problem" are summarized in Wittor (2021). For us the question remains if a large scale cluster simulation with an "advanced" model for sub-galactic CR sources is still able to produce a γ-ray luminosity in accordance with observational constraints or if those limits are hopelessly exceeded. However, reliable insights can of course only be expected if the whole simulation framework is sensible, which includes a proper treatment of CR diffusion and a realistic model for γ-ray emission. Last, but not least, supernova remnants are not the only relevant sub-galactic CR sources and a model for CR injection by AGN is most certainly also needed. Besides that, there are also large-scale shock waves from cluster mergers during hierarchical structure formation that act as particle accelerators and are already incorporated in *CRESCENDO*.

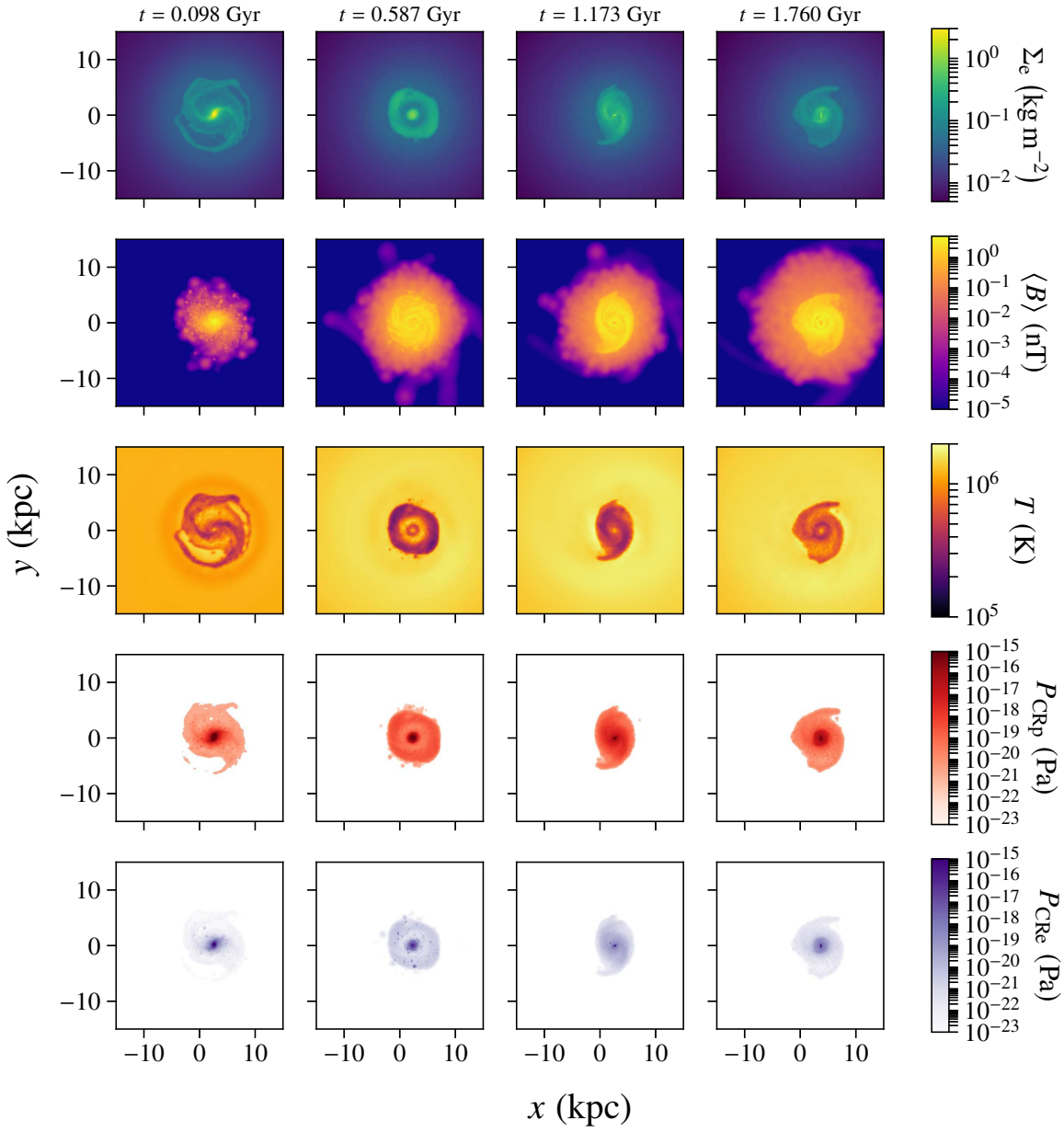

Figure 5.4: 4 snapshots show the temporal evolution of different quantities in the simulated galaxy. Note that the galaxy tends to move to the right over time, because the centre of mass does not remain located exactly at the origin.

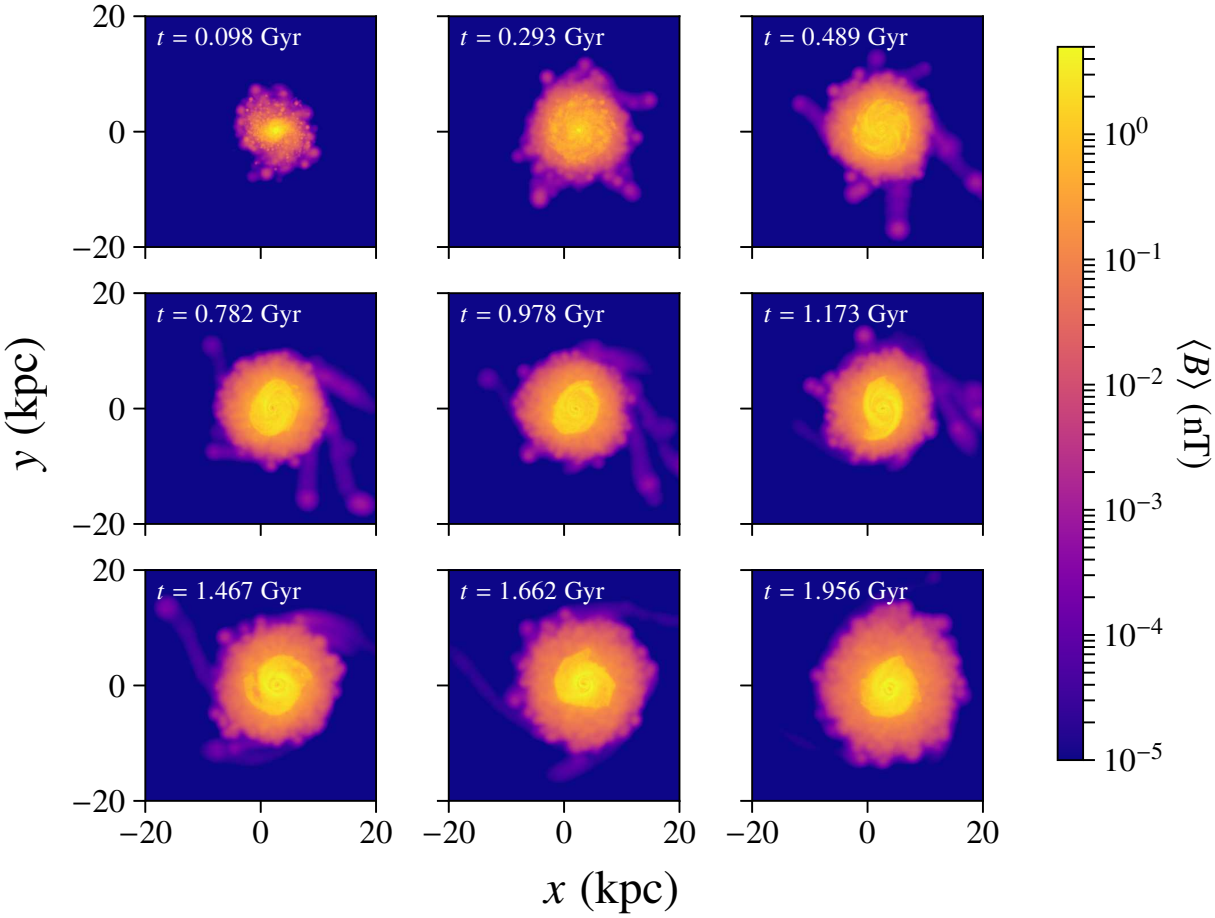

Figure 5.5: Average magnitude of magnetic flux density $\langle|\mathbf{B}|\rangle$ along the line of sight (head-on projection).

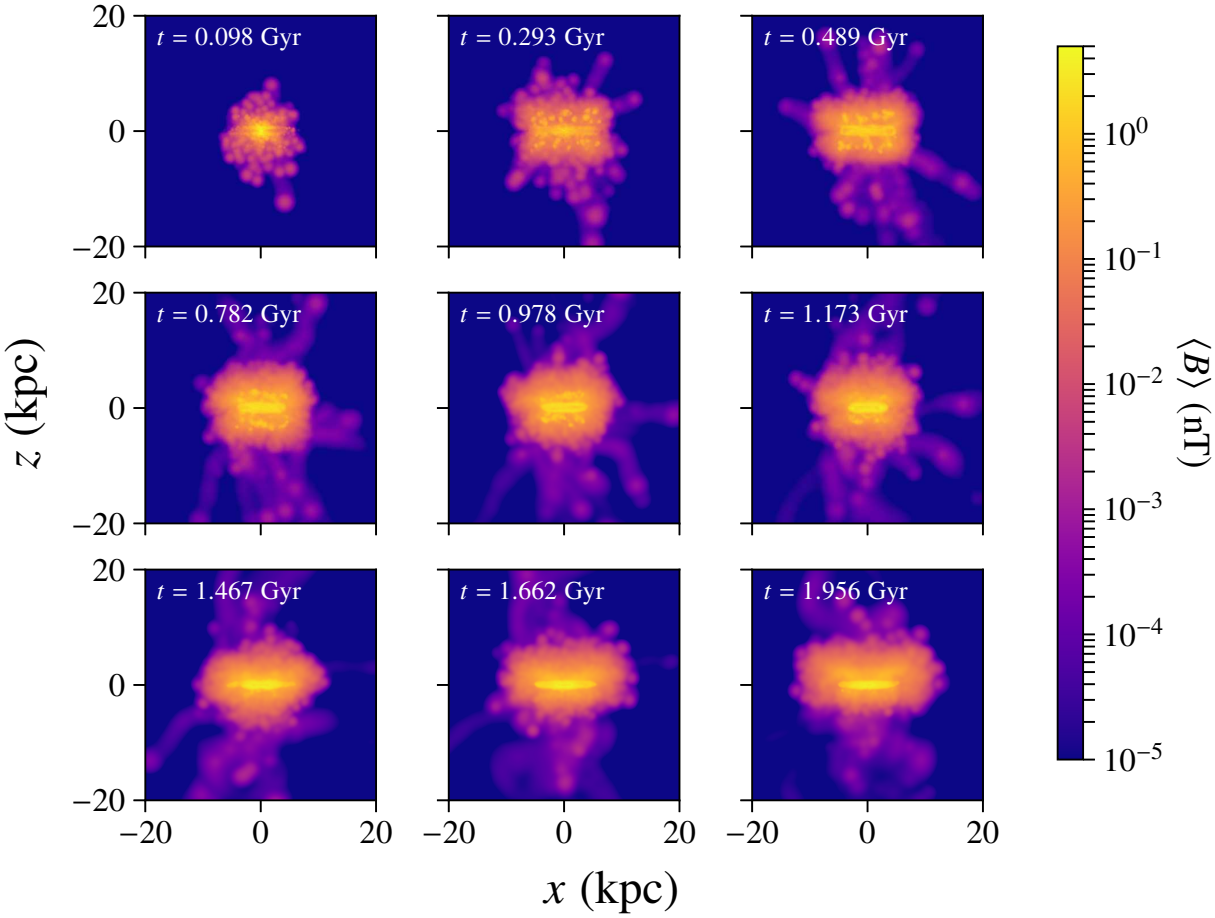

Figure 5.6: Average magnitude of magnetic flux density $\langle|\mathbf{B}|\rangle$ along the line of sight (edge-on projection).

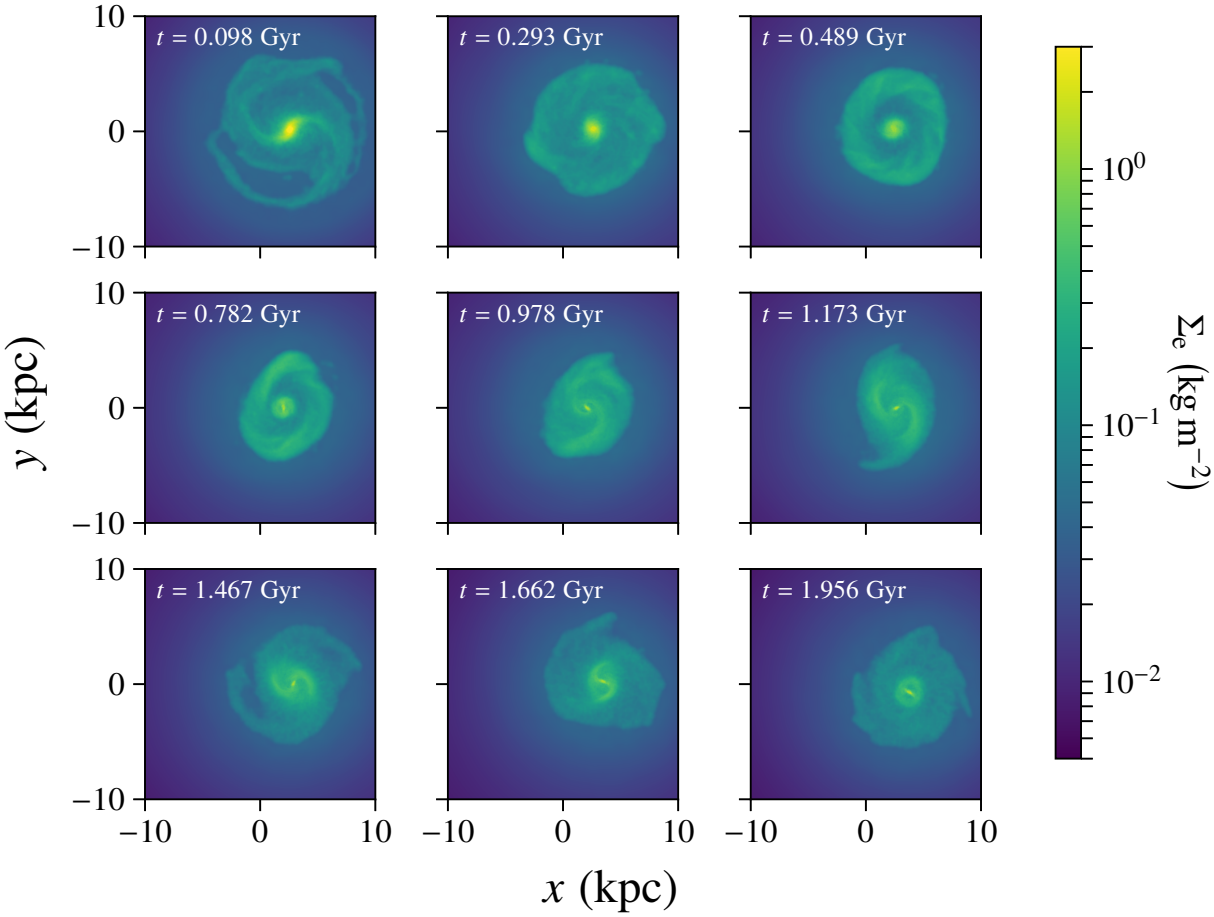

Figure 5.7: Surface mass density.

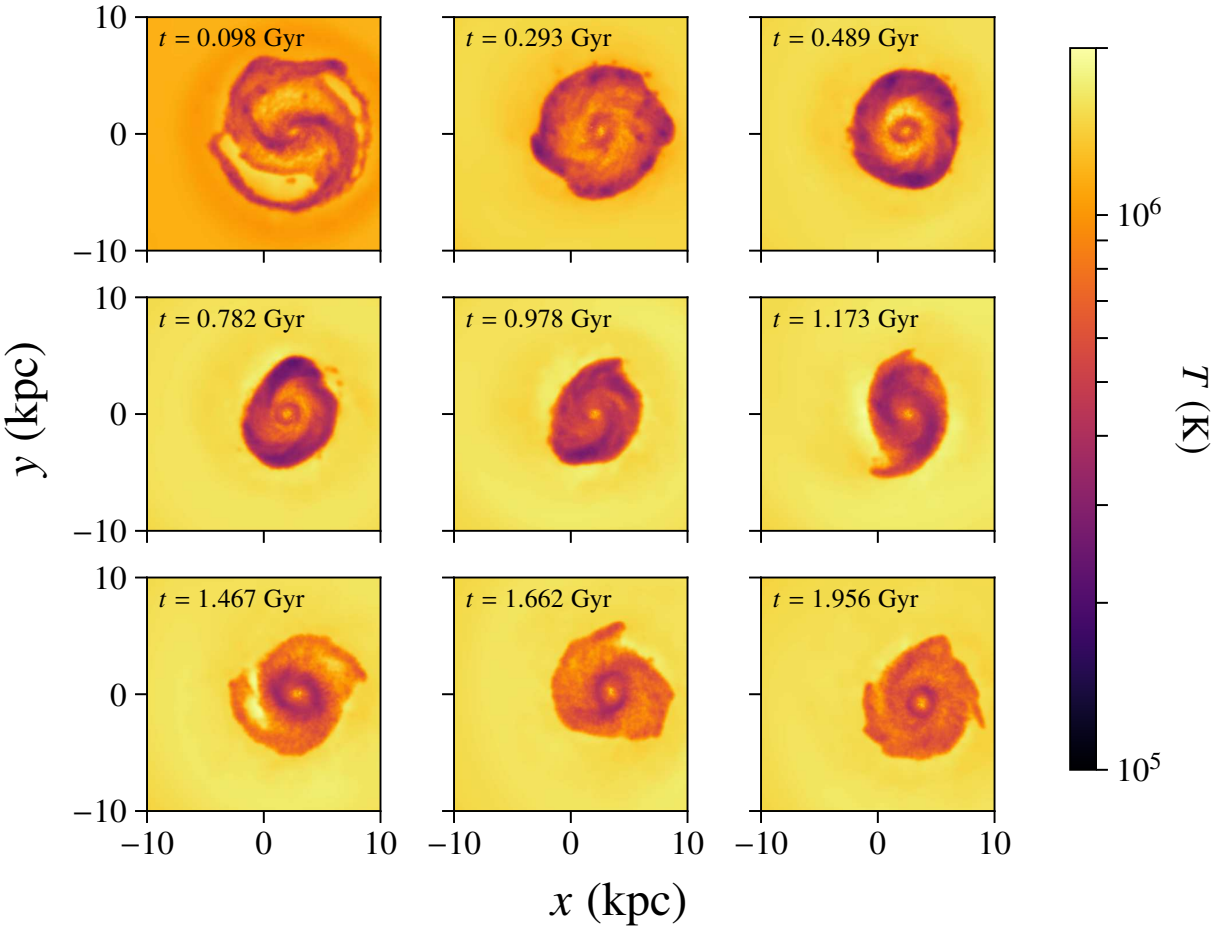

Figure 5.8: Gas temperature averaged along the line of sight.

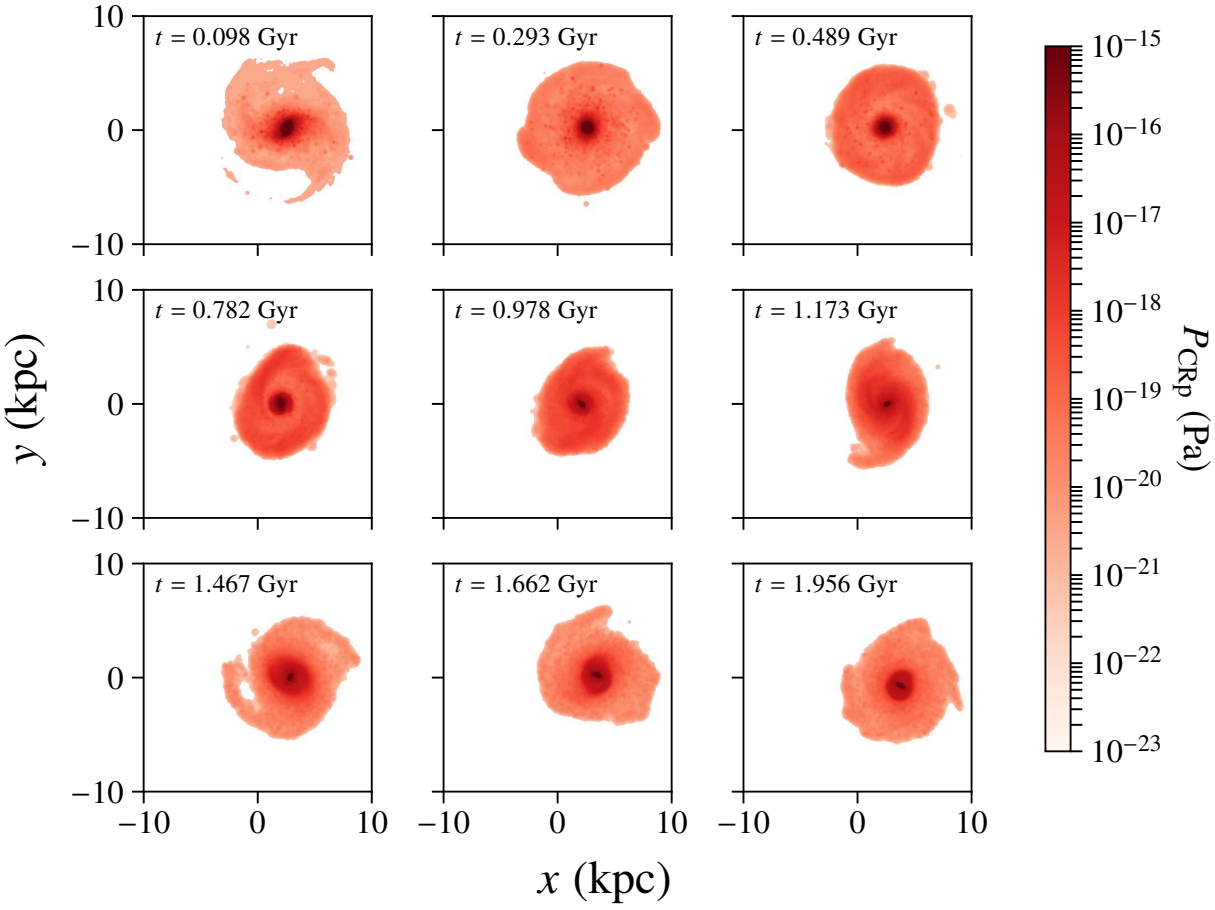

Figure 5.9: Cosmic ray proton pressure.

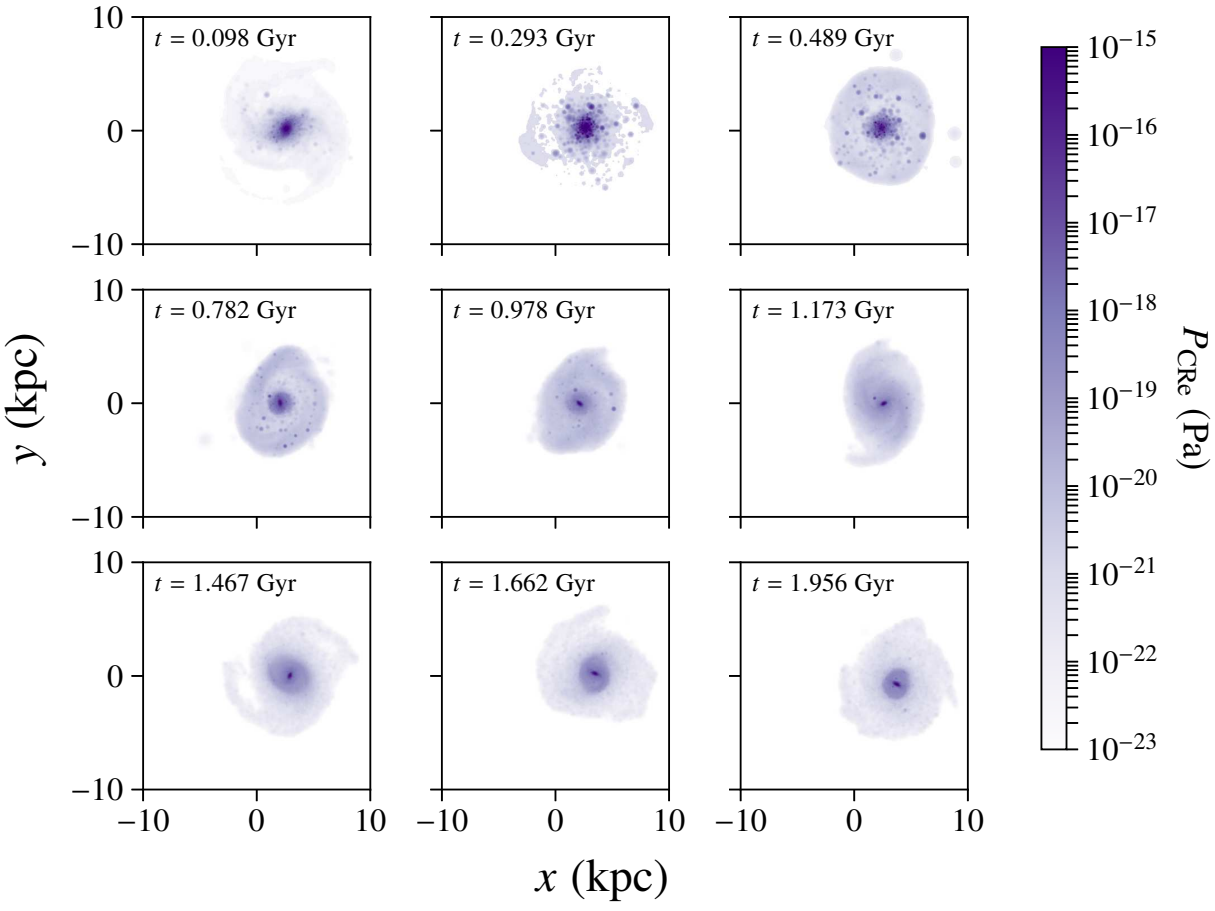

Figure 5.10: Cosmic ray electron pressure. Note the clumpy structure in the early snapshots due to spatially discrete seeding by SNRs.

6 Conclusions

The main purpose of this Master's thesis was to develop a sub-grid model for CR seeding by supernova remnants. This goal was partially reached, because spectra for different supernova types could be successfully calculated and the early test simulations also seemed promising. Running a Milky-Way-like galaxy with the improved CR model introduced in chapter 3 will be an important goal for the near future. In this last chapter we will therefore look back on the most important aspects of this Master's thesis.

In the introduction we emphasized that cosmic-ray astrophysics is a very active research topic; partly, because their feedback plays a non-negligible role for the evolution of galaxies and partly because the accelerating sources themselves are exciting laboratories for extreme physical processes. It was shown that supernova remnants are most likely *the* source of Galactic cosmic rays due to their large energy output (compared to every other plausible source), but also because observations of non-thermal radio and γ-ray emission have firmly shown that protons and electrons are accelerated to high energies in the shocks of historical SNRs. We also emphasized that it is still debated if SNRs can act as pevatrons and are therefore able to accelerate protons up to the "knee" in the CR energy spectrum.

Then we discussed some elements of diffusive shock acceleration in the test-particle limit and carefully explained where the power-law spectrum comes from. The CR distribution function at the shock front is also a central part of the proposed CR model discussed in chapter 3. Further ingredients are descriptions of the shock radius and velocity, a recipe for particle escape from the remnant, a treatment of magnetic field amplification and the inclusion of various energy-loss processes. We tried to combine different approaches from the available literature, but largely followed the steps in Morlino and Celli (2021). It should also be noted that some very important papers on CR models of SNRs or realistic choices of the spectral slope have appeared quite recently, so this Master's thesis could not have been written five years ago (at least in this form). The same holds of course for the simulations that were carried out with *OpenGadget3*: they could only be done thanks to the combined efforts of numerous people who were involved in the development of this mighty simulation code over the past decade.

An important lesson from the CR model is that the inclusion of magnetic field amplification and the distinction between escaping and trapped particles is absolutely necessary in order to reach the high energies that are required for an explanation of the Galactic cosmic ray spectrum. Other effects that were included are of course also important in the sense that together they make our sub-grid recipe more "realistic". Despite the improvements compared to usual prescriptions for CR seeding in cosmological simulations, there are still a lot of inconsistencies. The most severe ones might be (1) the assumption of a remnant that stays spherically symmetric at least until the snowplough phase, (2) ad-hoc simplifications concerning the evolution of the maximum particle energy at the shock and (3) the inconsistent usage of ultra-relativistic approximations (like $E = pc$) even for low momenta. Therefore, there is still plenty of room for further improvements.

A List of abbreviations

The following table contains the most frequently used abbreviations in the text (most of them are pretty common).

abbreviation	meaning
AGN	active galactic nucleus
CMB	cosmic microwave background
CR	cosmic ray
DSA	diffusive shock acceleration
ED	ejecta-dominated (first phase of SNR evolution)
IC	inverse Compton (scattering)
ICM	intracluster medium
ISM	interstellar medium
ISRF	interstellar radiation field
NLDSA	non-linear diffusive shock acceleration
SN	supernova
SNR	supernova remnant
SP	snowplough phase (third phase of SNR evolution)
SPH	smoothed particle hydrodynamics
ST	Sedov-Taylor (second phase of SNR evolution)
UHECR	ultra-high-energy cosmic ray
UV	ultraviolet

B Used software

The cosmic ray spectra and some of the plots were made by using a *Mathematica* notebook (Wolfram Research Inc., 2021), which is based on a template that was kindly provided by Giovanni Morlino (see Morlino and Celli, 2021). Simulations of galaxies were run with the cosmological SPH N-body code *OpenGadget3*, which is written in C/C++ and based on the *Gadget-2* code by Volker Springel (cf. Springel, 2005). Cosmic ray seeding from supernovae was included in the module *CRESCENDO* by Böss *et al.* (2023). The snapshot files of the simulations were analyzed and visualized with *Smac* (Dolag *et al.*, 2005) and *Python3*. More specifically, the *Python* packages *Astropy* (Astropy Collaboration, 2022), *numpy* (Harris *et al.*, 2020), *matplotlib* (Hunter, 2007) and *g3read*[1] were used.

[1] https://github.com/aragagnin/g3read

C The distribution function and its moments

In this chapter we briefly summarize some properties of the distribution function and its moments. We define the distribution function as the particle number density in six-dimensional phase space:

$$f(\mathbf{x}, \mathbf{p}, t) \coloneqq \frac{\mathrm{d}N}{\mathrm{d}\mathcal{V}_x \, \mathrm{d}\mathcal{V}_p} \,. \tag{C.1}$$

This quantity is widely used in kinetic theory and has the advantage that it is Lorentz-invariant. Although this cannot be seen directly from the definition above, it follows from the relativistic transformation laws for volumes in physical and in momentum space (e.g. Misner *et al.*, 1973, chap. 22.6; Thorne and Blandford, 2017, chap. 3.2.2). The basic argument is that when on goes from the rest frame of the particles (primed) to some laboratory frame (unprimed) the volume transforms as $\mathrm{d}\mathcal{V}_x = \mathrm{d}\mathcal{V}_{x'}/\gamma$, because one side is Lorentz contracted. Similarly, one can show that the volume in momentum space transforms as $\mathrm{d}\mathcal{V}_p = \gamma \, \mathrm{d}\mathcal{V}_{p'}$. Hence, for the product we find $\mathrm{d}\mathcal{V}_x \, \mathrm{d}\mathcal{V}_p = \mathrm{d}\mathcal{V}_{x'} \, \mathrm{d}\mathcal{V}_{p'}$, meaning that it is Lorentz invariant. Since the number of particles belonging to our selected set is also frame-independent, $f(\mathbf{x}, \mathbf{p}, t)$ itself is Lorentz invariant.

We now come to the different moments of the distribution function. Its first moment is relativistic number-flux four-vector $\vec{J}$, defined as

$$\vec{J}(t, \mathbf{x}) \equiv c \int f \vec{p} \, \frac{\mathrm{d}\mathcal{V}_p}{E} = \int f \vec{p} \, \frac{\mathrm{d}\mathcal{V}_p}{p^0} \,, \tag{C.2}$$

$$J^0(t, \mathbf{x}) = \int f p^0 \, \frac{\mathrm{d}\mathcal{V}_p}{p^0} = \int f \, \mathrm{d}\mathcal{V}_p = n(t, \mathbf{x}) \,, \tag{C.3}$$

$$\mathbf{J}(t, \mathbf{x}) = c \int f \mathbf{p} \, \frac{\mathrm{d}\mathcal{V}_p}{E} = \frac{1}{c} \int f \mathbf{v} \, \mathrm{d}\mathcal{V}_p = \frac{1}{c} n(t, \mathbf{x}) \langle \mathbf{v} \rangle = \frac{\mathbf{j}}{c} \quad \xrightarrow{v \ll c} \quad \mathbf{J} \equiv \int f \vec{p} \, \frac{\mathrm{d}\mathcal{V}_p}{m} \,. \tag{C.4}$$

Here we used the identity $E\mathbf{v} = \mathbf{p}c^2$ for the relativistic momentum $\mathbf{p}$ and the total energy E. In the second and third line we performed a 3+1 split and wrote the temporal and spatial component of $\vec{J}$ separately. One sees that $J^0(t, \mathbf{x})$ is equal to the number density, whereas $\mathbf{J}(t, \mathbf{x})$ is proportional to the number flux (see also the familiar non-relativistic limits).

The second moment of the distribution function is the stress-energy tensor $\mathbf{T}$:

$$\mathbf{T}(t, \mathbf{x}) = c^2 \int f \vec{p} \otimes \vec{p} \, \frac{\mathrm{d}\mathcal{V}_p}{E} \quad \xrightarrow{v \ll c} \quad \mathbf{T} = \int f \vec{p} \otimes \vec{p} \, \frac{\mathrm{d}\mathcal{V}_p}{m} \,, \tag{C.5}$$

$$u(t, \mathbf{x}) \equiv T^{00} = c^2 \int f p^0 p^0 \, \frac{\mathrm{d}\mathcal{V}_p}{E} = \int f E^2 \, \frac{\mathrm{d}\mathcal{V}_p}{E} = \int f E \, \mathrm{d}\mathcal{V}_p \,, \tag{C.6}$$

$$\mathbf{S}(t, \mathbf{x}) \equiv c T^{0j} = c^3 \int f p^0 p^j \, \frac{\mathrm{d}\mathcal{V}_p}{E} = c^2 \int f p^j \, \mathrm{d}\mathcal{V}_p \,, \tag{C.7}$$

$$\mathbf{G}(t, \mathbf{x}) \equiv T^{jk} = \int f p^j p^k c \, \frac{\mathrm{d}\mathcal{V}_p}{p^0} = \int f v^j p^k \, \mathrm{d}\mathcal{V}_p \,. \tag{C.8}$$

Again, by looking at the components separately one sees that T^{00} is the mass-energy density, T^{0j} is the momentum density or, equivalently, the energy flux and T^{jk} is the stress tensor.

So far, everything was kept quite general, but now we focus on the special case of an isotropic distribution function $f = f(\mathbf{x}, p, t)$, which is most relevant for this thesis. More specifically, in the particles' mean rest frame at some event in spacetime (i.e. the frame in which the particle flux $\mathbf{J}$ vanishes) and for a distribution function f that is isotropic in this reference frame, meaning that it only depends on $|\mathbf{p}|$, we can easily work out the relativistic particle density n, mass-energy density u and pressure P (for a detailed discussion see e.g. Bartelmann, 2021, chap. 3.1; Thorne and Blandford, 2017, chap. 3):

$$n = J^0 = \int f \, \mathrm{d}\mathcal{V}_p = 4\pi \int_0^\infty f(p)\, p^2 \, \mathrm{d}p \ , \tag{C.9}$$

$$u \equiv T^{00} = \int f\, E \, \mathrm{d}\mathcal{V}_p = 4\pi \int_0^\infty f(p)\, E(p)\, p^2 \, \mathrm{d}p \ , \tag{C.10}$$

$$P \equiv \frac{1}{3}\sum_{j=1}^{3} T_{jj} = \frac{1}{3}\int f\, p^2 c^2 \, \frac{\mathrm{d}\mathcal{V}_p}{E(p)} = \frac{4\pi}{3}\int_0^\infty f\, p^4 c^2 \, \frac{\mathrm{d}p}{E(p)} = \frac{4\pi}{3}\int_0^\infty f(p)\, p^3\, v(p)\, \mathrm{d}p \ , \tag{C.11}$$

where $E = pc^2/v$ was used in the last step. In the ultra-relativistic limit $v \longrightarrow c$, the energy-density and pressure simplify to

$$u = 4\pi \int_0^\infty f(p)\, p^3 c \, \mathrm{d}p \ , \tag{C.12}$$

$$P = \frac{4\pi}{3} \int_0^\infty f(p)\, p^3 c \, \mathrm{d}p \ , \tag{C.13}$$

which coincides with the well-known relation $u = 3P$ of a photon gas. Both these equations will be used extensively throughout the main text of this thesis.

For the calculation of the CR spectra in supernova remnants we obtain a different quantity, namely the momentum density N, defined by integrating the distribution function over the spatial volume:

$$N(p) = \int f \, \mathrm{d}\mathcal{V}_x = 4\pi \int_0^\infty f(r, p, t)\, r^2 \, \mathrm{d}r \tag{C.14}$$

Last but not least, we show how the distribution function $f(p)$ can be expressed as a function of energy $\tilde{f}(E)$ instead of momentum in the relativistic limit $E = pc$ (these are really different functions with different arguments and units!). We just require that we have to obtain the same number density, no matter if we integrate over momentum or energy:

$$n(\mathbf{x}, t) = \int \tilde{f}(\mathbf{x}, E, t)\, \mathrm{d}E \overset{!}{=} \int f(\mathbf{x}, p, t)\, \mathrm{d}^3 p = 4\pi \int f(\mathbf{x}, p, t) p^2 \, \mathrm{d}p \tag{C.15}$$

$$= 4\pi \int f(\mathbf{x}, E/c, t)(E/c)^2 \, \frac{\mathrm{d}E}{c} \, . \tag{C.16}$$

This implies that

$$\tilde{f}(\mathbf{x}, E, t) = \frac{4\pi E^2}{c^3} f(\mathbf{x}, E/c, t) \,. \tag{C.17}$$

Similarly, the distribution function can also be expressed in terms of the Lorentz factor γ:

$$\int \hat{f}(\mathbf{x}, \gamma, t) \,\mathrm{d}\gamma \stackrel{!}{=} 4\pi \int f(\mathbf{x}, p, t) p^2 \,\mathrm{d}p \tag{C.18}$$

$$= 4\pi \int f(\mathbf{x}, \gamma m_\mathrm{e} c, t)(\gamma m_\mathrm{e} c)^2 \,\mathrm{d}(\gamma m_\mathrm{e} c) \tag{C.19}$$

$$= 4\pi \int f(\mathbf{x}, \gamma m_\mathrm{e} c, t)\gamma^2 (m_\mathrm{e} c)^3 \,\mathrm{d}\gamma \tag{C.20}$$

$$\implies \quad \hat{f}(\mathbf{x}, \gamma, t) = 4\pi\gamma^2 (m_\mathrm{e} c)^3 f(\mathbf{x}, \gamma m_\mathrm{e} c, t) \,. \tag{C.21}$$

D Derivation of the time $t_0(r,t)$

In section 3.2 we introduced the linear velocity profile for matter inside the SNR (cf. equation 3.3). We now do not treat r as an independent variable any longer, but consider it as a function of time instead. By following the approach in Morlino and Celli (2021) we rewrite the profile as a differential equation for $r(t)$:

$$\frac{\mathrm{d}r(t)}{\mathrm{d}t} = v(t) = \left(1 - \frac{1}{\sigma}\right)\frac{v_{\mathrm{sh}}(t)}{R_{\mathrm{sh}}(t)} r(t)\,, \qquad r < R_{\mathrm{sh}}\,. \tag{D.1}$$

By inserting equations (3.14) and (3.15), we can write the right-hand side explicitly as

$$\frac{1}{r}\frac{\mathrm{d}r}{\mathrm{d}t} = \left(1 - \frac{1}{\sigma}\right)\frac{1}{R_{\mathrm{sh}}(t)}\frac{R_{\mathrm{ch}}}{t_{\mathrm{ch}}}\left(\frac{R_{\mathrm{sh}}(t)}{R_{\mathrm{ch}}}\right)^{1+a}\left(\lambda_{\mathrm{ED}}\tilde{\zeta}\left(\tilde{\zeta}\frac{t}{t_{\mathrm{ch}}}\right)^{-a\lambda_{\mathrm{ED}}-1} + \lambda_{\mathrm{ST}}\tilde{\xi}\left(\tilde{\xi}\frac{t}{t_{\mathrm{ch}}}\right)^{-a\lambda_{\mathrm{ST}}-1}\right) \tag{D.2}$$

$$= \left(1 - \frac{1}{\sigma}\right)\frac{1}{t_{\mathrm{ch}}}\left(\frac{R_{\mathrm{sh}}(t)}{R_{\mathrm{ch}}}\right)^{a}\left(\lambda_{\mathrm{ED}}\tilde{\zeta}\left(\tilde{\zeta}\frac{t}{t_{\mathrm{ch}}}\right)^{-a\lambda_{\mathrm{ED}}-1} + \lambda_{\mathrm{ST}}\tilde{\xi}\left(\tilde{\xi}\frac{t}{t_{\mathrm{ch}}}\right)^{-a\lambda_{\mathrm{ST}}-1}\right) \tag{D.3}$$

$$= \left(1 - \frac{1}{\sigma}\right)\frac{1}{t_{\mathrm{ch}}}\frac{\lambda_{\mathrm{ED}}\tilde{\zeta}\left(\tilde{\zeta}\frac{t}{t_{\mathrm{ch}}}\right)^{-a\lambda_{\mathrm{ED}}-1} + \lambda_{\mathrm{ST}}\tilde{\xi}\left(\tilde{\xi}\frac{t}{t_{\mathrm{ch}}}\right)^{-a\lambda_{\mathrm{ST}}-1}}{\left(\tilde{\zeta}\frac{t}{t_{\mathrm{ch}}}\right)^{-a\lambda_{\mathrm{ED}}} + \left(\tilde{\xi}\frac{t}{t_{\mathrm{ch}}}\right)^{-a\lambda_{\mathrm{ST}}}}\,. \tag{D.4}$$

We then integrate both sides over time (between t_0 and t). For the left-hand side we find

$$\int_{t_0}^{t}\frac{1}{r}\frac{\mathrm{d}r}{\mathrm{d}s}\,\mathrm{d}s = \int_{t_0}^{t}\frac{\mathrm{d}\ln(r)}{\mathrm{d}s}\,\mathrm{d}s = \ln\left(\frac{r(t)}{r(t_0)}\right). \tag{D.5}$$

For the right-hand side we introduce the variable substitution $t_* = t/t_{\mathrm{ch}}$ and obtain

$$\int_{t_0}^{t}\left(1 - \frac{1}{\sigma}\right)\frac{1}{t_{\mathrm{ch}}}\frac{\lambda_{\mathrm{ED}}\tilde{\zeta}\left(\tilde{\zeta}\frac{s}{t_{\mathrm{ch}}}\right)^{-a\lambda_{\mathrm{ED}}-1} + \lambda_{\mathrm{ST}}\tilde{\xi}\left(\tilde{\xi}\frac{s}{t_{\mathrm{ch}}}\right)^{-a\lambda_{\mathrm{ST}}-1}}{\left(\tilde{\zeta}\frac{s}{t_{\mathrm{ch}}}\right)^{-a\lambda_{\mathrm{ED}}} + \left(\tilde{\xi}\frac{s}{t_{\mathrm{ch}}}\right)^{-a\lambda_{\mathrm{ST}}}}\,\mathrm{d}s \tag{D.6}$$

$$= \int_{t_0/t_{\mathrm{ch}}}^{t/t_{\mathrm{ch}}}\left(1 - \frac{1}{\sigma}\right)\frac{\lambda_{\mathrm{ED}}\tilde{\zeta}\left(\tilde{\zeta}t_*\right)^{-a\lambda_{\mathrm{ED}}-1} + \lambda_{\mathrm{ST}}\tilde{\xi}\left(\tilde{\xi}t_*\right)^{-a\lambda_{\mathrm{ST}}-1}}{\left(\tilde{\zeta}t_*\right)^{-a\lambda_{\mathrm{ED}}} + \left(\tilde{\xi}t_*\right)^{-a\lambda_{\mathrm{ST}}}}\,\mathrm{d}t_* \tag{D.7}$$

$$= -\frac{1}{a}\left(1 - \frac{1}{\sigma}\right)\ln\left(\left(\tilde{\zeta}t_*\right)^{-a\lambda_{\mathrm{ED}}} + \left(\tilde{\xi}t_*\right)^{-a\lambda_{\mathrm{ST}}}\right)\Bigg|_{t_0/t_{\mathrm{ch}}}^{t/t_{\mathrm{ch}}} \tag{D.8}$$

$$= -\frac{1}{a}\left(1 - \frac{1}{\sigma}\right)\ln\left(\frac{\left(\tilde{\zeta}t/t_{\mathrm{ch}}\right)^{-a\lambda_{\mathrm{ED}}} + \left(\tilde{\xi}t/t_{\mathrm{ch}}\right)^{-a\lambda_{\mathrm{ST}}}}{\left(\tilde{\zeta}t_0/t_{\mathrm{ch}}\right)^{-a\lambda_{\mathrm{ED}}} + \left(\tilde{\xi}t_0/t_{\mathrm{ch}}\right)^{-a\lambda_{\mathrm{ST}}}}\right). \tag{D.9}$$

Finally, we get the following implicit equation for the time $t_0(r,t)$ when a plasma element at a given radius r and time t was shocked:

$$\frac{\sigma a}{\sigma - 1}\ln\left(\frac{r(t)}{r(t_0)}\right) = \ln\left(\frac{\left(\tilde{\zeta}t_0/t_{\mathrm{ch}}\right)^{-a\lambda_{\mathrm{ED}}} + \left(\tilde{\xi}t_0/t_{\mathrm{ch}}\right)^{-a\lambda_{\mathrm{ST}}}}{\left(\tilde{\zeta}t/t_{\mathrm{ch}}\right)^{-a\lambda_{\mathrm{ED}}} + \left(\tilde{\xi}t/t_{\mathrm{ch}}\right)^{-a\lambda_{\mathrm{ST}}}}\right). \tag{D.10}$$

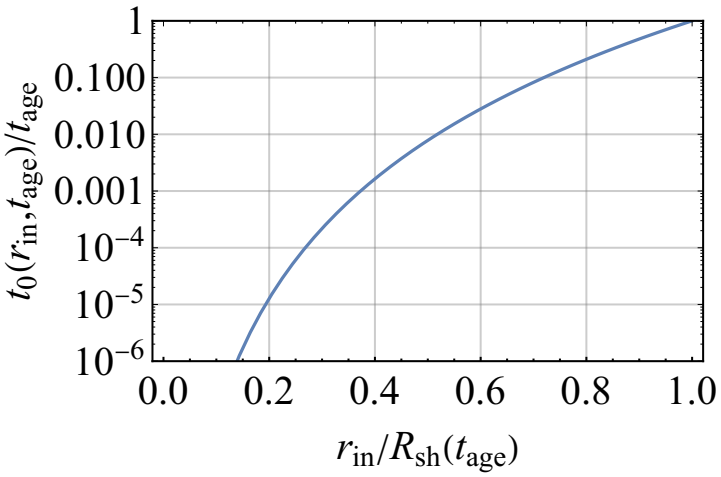

Figure D.1: Plot of $t_0(r_{\rm in}, t_{\rm age})$ for a fixed time $t_{\rm age} = 100$ yr (the momentary SNR age) as a function of the internal radius $r_{\rm in} \leq R_{\rm sh}(t_{\rm age})$. As expected $t_0(r_{\rm in}, t_{\rm age})$ is monotonically increasing with radius and satisfies the condition $t_0(R_{\rm sh}(t_{\rm age}), t_{\rm age}) = t_{\rm age}$.

Although the logarithm could be removed by a simple exponentiation, the above form turns out to be numerically more reliable when using standard root-finding routines to calculate $t_0(r,t)$. The dependence on radius of $t_0(r,t)$ is shown in figure D.1.

E Adiabatic energy losses

In this chapter we will derive the equation for adiabatic energy losses, that was used in chapter 3. They arise if high energy particles confined within an expanding volume do work at the cost of the internal energy of the gas. In order to derive the loss equation, we start from the first law of thermodynamics,

$$\mathrm{d}U = \delta W + \delta Q + \delta E_N = -p\,\mathrm{d}V + T\,\mathrm{d}S + \mu\,\mathrm{d}N \tag{E.1}$$

where δW, δQ δE_N denote the 1-forms (in the usual weird thermodynamical notation) of mechanical work, heat exchange and energy increase by adding particles. Since we consider an adiabatic process ($\delta Q = 0$) with a fixed number of particles ($\mathrm{d}N = 0$), the first law reduces to

$$\mathrm{d}U = -P\,\mathrm{d}V = -nk_\mathrm{B}T\,\mathrm{d}V = -\frac{1}{3}E_\mathrm{kin}n\,\mathrm{d}V \tag{E.2}$$

Here we used (1) the ideal-gas law $P = nk_\mathrm{B}T$, which holds for any classical system of non-interacting particles (regardless of whether they are relativistic or non-relativistic) and (2) the equipartition theorem for the mean kinetic energy per particle, $E_\mathrm{kin} = 3k_\mathrm{B}T$. Alternatively, one could continue the derivation by using the equation of state for a relativistic gas, namely $U = 3nVk_\mathrm{B}T$ and $U = 3PV$.

Note that the internal energy can be written as

$$\mathrm{d}U = N\,\mathrm{d}E_\mathrm{kin} = nV\,\mathrm{d}E_\mathrm{kin}\ , \tag{E.3}$$

which directly follows from its definition. By combining those equations (E.2) and (E.3) one gets

$$\mathrm{d}E_\mathrm{kin} = -\frac{1}{3}\frac{E_\mathrm{kin}}{V}\,\mathrm{d}V \quad\Longrightarrow\quad \frac{\mathrm{d}E_\mathrm{kin}}{\mathrm{d}t} = -\frac{1}{3}\frac{E_\mathrm{kin}}{V}\frac{\mathrm{d}V}{\mathrm{d}t}\ . \tag{E.4}$$

The time derivative of the volume can be written in terms of the velocity field's divergence:

$$\frac{\mathrm{d}V}{\mathrm{d}t} = (\boldsymbol{\nabla}\cdot\mathbf{v})V = -\frac{1}{\rho}\frac{\mathrm{d}\rho}{\mathrm{d}t}V \tag{E.5}$$

In the last step we used the continuity equation in Lagrangian form. Finally, we get

$$\frac{1}{E_\mathrm{kin}}\frac{\mathrm{d}E_\mathrm{kin}}{\mathrm{d}t} = \frac{1}{3}\frac{1}{\rho}\frac{\mathrm{d}\rho}{\mathrm{d}t} = \frac{1}{\rho^{1/3}}\frac{\mathrm{d}\rho^{1/3}}{\mathrm{d}t} = \frac{1}{(\rho/\rho_0)^{1/3}}\frac{\mathrm{d}(\rho/\rho_0)^{1/3}}{\mathrm{d}t} = \frac{1}{L(t_0,t)}\frac{\mathrm{d}L(t_0,t)}{\mathrm{d}t} \tag{E.6}$$

Here, we inserted the constant $\rho_0 \coloneqq \rho(t_0)$ at an fixed, arbitrary time t_0 and defined the adiabatic loss function $L(t_0,t)$ as

$$L(t_0,t) \coloneqq \left(\frac{\rho(t)}{\rho(t_0)}\right)^{1/3} \tag{E.7}$$

Note that the above equation can be rewritten in terms of logarithmic derivatives and then integrated from t_0 to t:

$$\frac{\mathrm{d}\ln(E_\mathrm{kin}(t))}{\mathrm{d}t} = \frac{\mathrm{d}\ln(L(t_0,t))}{\mathrm{d}t} \tag{E.8}$$

$$\iff \quad \ln\left(\frac{E_{\text{kin}}(t)}{E_{\text{kin}}(t_0)}\right) = \ln\left(\frac{L(t_0,t)}{L(t_0,t_0)}\right) = \ln(L(t_0,t)) \tag{E.9}$$

$$\iff \quad E_{\text{kin}}(t) = E_{\text{kin}}(t_0)L(t_0,t) \tag{E.10}$$

At the end of this section, we briefly derive the average kinetic energy per particle for a relativistic gas. More precisely, we derive the general equipartition theorem for a classical system of particles described by a Hamiltonian H and with phase space coordinates x_i by following Pathria and Beale (2022, chap. 3). The idea is to calculate the expectation value $\langle x_i \frac{\partial H}{\partial x_j} \rangle$ in the canonical ensemble (which could similarly be done in the microcanonical ensemble):

$$\left\langle x_i \frac{\partial H}{\partial x_j} \right\rangle = Z^{-1} \int_\Gamma x_i \frac{\partial H}{\partial x_j} \, \mathrm{e}^{-H/(k_\mathrm{B}T)} \, \mathrm{d}\Gamma \tag{E.11}$$

$$= -k_\mathrm{B}T \, Z^{-1} \int_\Gamma x_i \frac{\partial}{\partial x_j} \mathrm{e}^{-H/(k_\mathrm{B}T)} \, \mathrm{d}\Gamma \tag{E.12}$$

$$= -k_\mathrm{B}T \, Z^{-1} x_i \, \mathrm{e}^{-H/(k_\mathrm{B}T)} \Big|_{\partial\Gamma} + k_\mathrm{B}T \, Z^{-1} \int_\Gamma \frac{\partial x_i}{\partial x_j} \mathrm{e}^{-H/(k_\mathrm{B}T)} \, \mathrm{d}\Gamma \tag{E.13}$$

$$= k_\mathrm{B}T \, Z^{-1} \int_\Gamma \delta_{ij} \mathrm{e}^{-H/(k_\mathrm{B}T)} \, \mathrm{d}\Gamma = k_\mathrm{B}T\delta_{ij} \, . \tag{E.14}$$

Here $Z \coloneqq \int_\Gamma \exp(-H/(k_\mathrm{B}T)) \, \mathrm{d}\Gamma$ is the partition function and the boundary term vanishes, because the Hamiltonian becomes infinite when the generalized coordinates have "extreme values". For example, extreme values in momentum space are $\pm\infty$, so the kinetic energy diverges. In physical space, boundary values correspond to walls confining the system, which is formally described by an infinite potential. From the equipartition theorem above one finds the expectation value for $\mathbf{p} \cdot \mathbf{v}$:

$$\langle \mathbf{p} \cdot \mathbf{v} \rangle = \left\langle \sum_{i=1}^{3} p_i \dot{q}_i \right\rangle = \sum_{i=1}^{3} \left\langle p_i \frac{\partial H}{\partial p_i} \right\rangle = 3k_\mathrm{B}T \, . \tag{E.15}$$

In general, the product on the left-hand side is $\mathbf{p} \cdot \mathbf{v} = \gamma m v^2$, so by using $\lim_{v/c \to 1} \mathbf{p} \cdot \mathbf{v} = \gamma m c^2$ and $\lim_{v/c \to 0} \mathbf{p} \cdot \mathbf{v} = m v^2$ one finds for the non-relativistic and the ultra-relativistic kinetic energy

$$v \ll c: \quad \left\langle E_{\text{kin, non-rel.}} \right\rangle = \left\langle \frac{1}{2} m v^2 \right\rangle \approx \frac{1}{2} \langle \mathbf{p} \cdot \mathbf{v} \rangle = \frac{3}{2} k_\mathrm{B}T \, , \tag{E.16}$$

$$v \approx c: \quad \left\langle E_{\text{kin, ultra-rel.}} \right\rangle = \left\langle (\gamma - 1) m c^2 \right\rangle \approx \left\langle \gamma m c^2 \right\rangle \approx \langle \mathbf{p} \cdot \mathbf{v} \rangle = 3k_\mathrm{B}T \, . \tag{E.17}$$

Bibliography

Amato, E., and P. Blasi (2005). *A general solution to non-linear particle acceleration at non-relativistic shock waves*. MNRAS **364**, L76.

Astropy Collaboration, (2022). *The Astropy Project: Sustaining and Growing a Community-oriented Open-source Project and the Latest Major Release (v5.0) of the Core Package*. ApJ **935** (2), 167.

Axford, W. I., E. Leer, and G. Skadron (1977). "The Acceleration of Cosmic Rays by Shock Waves." In: *Proceedings of the 15th International Cosmic Ray Conference*. Volume 11. p. 132.

Barenblatt, G. I. (2003). *Scaling* (Cambridge University Press, Cambridge).

Bartelmann, M. (2021). *Theoretical Astrophysics: An Introduction* (Heidelberg University Publishing, Heidelberg).

Beck, A. M., K. Dolag, H. Lesch, and P. P. Kronberg (2013). *Strong magnetic fields and large rotation measures in protogalaxies from supernova seeding*. MNRAS **435**, 3575.

Bell, A. R. (1978a). *The acceleration of cosmic rays in shock fronts - I*. MNRAS **182**, 147.

Bell, A. R. (1978b). *The acceleration of cosmic rays in shock fronts - II*. MNRAS **182**, 443.

Bell, A. R. (2004). *Turbulent amplification of magnetic field and diffusive shock acceleration of cosmic rays*. MNRAS **353**, 550.

Bell, A. R. (2013). *Cosmic ray acceleration*. Astroparticle Physics **43**, 56.

Bell, A. R., K. M. Schure, B. Reville, and G. Giacinti (2013). *Cosmic-ray acceleration and escape from supernova remnants*. MNRAS **431**, 415.

Blandford, R., and D. Eichler (1987). *Particle acceleration at astrophysical shocks: A theory of cosmic ray origin*. Phys. Rep. **154**, 1.

Blandford, R. D., and J. P. Ostriker (1978). *Particle acceleration by astrophysical shocks*. ApJ **221**, L29.

Blasi, P. (2010). *Shock acceleration of electrons in the presence of synchrotron losses – I. Test-particle theory*. MNRAS **402**, 2807.

Blasi, P. (2013). *The origin of galactic cosmic rays*. A&ARv **21**, 70.

Böss, L. M., U. P. Steinwandel, K. Dolag, and H. Lesch (2023). *CRESCENDO: an on-the-fly Fokker-Planck solver for spectral cosmic rays in cosmological simulations*. MNRAS **519**, 548.

Bykov, A. M., D. C. Ellison, A. Marcowith, and S. M. Osipov (2018). *Cosmic Ray Production in Supernovae*. Space Sci. Rev. **214**, 41.

Caprioli, D. (2015). *"Espresso" Acceleration of Ultra-high-energy Cosmic Rays*. ApJ **811**, L38.

Caprioli, D., P. Blasi, and E. Amato (2009). *On the escape of particles from cosmic ray modified shocks*. MNRAS **396**, 2065.

Caprioli, D., A.-R. Pop, and A. Spitkovsky (2015). *Simulations and Theory of Ion Injection at Non-relativistic Collisionless Shocks*. ApJ **798**, L28.

Caprioli, D., and A. Spitkovsky (2014). *Simulations of Ion Acceleration at Non-relativistic Shocks. I. Acceleration Efficiency*. ApJ **783**, 91.

Cardillo, M., E. Amato, and P. Blasi (2015). *On the cosmic ray spectrum from type II supernovae expanding*

in their red giant presupernova wind. Astroparticle Physics **69**, 1.

Casse, M., and J. A. Paul (1982). *On the stellar origin of the Ne-22 excess in cosmic rays*. ApJ **258**, 860.

Celli, S., G. Morlino, S. Gabici, and F. A. Aharonian (2019). *Exploring particle escape in supernova remnants through gamma rays*. MNRAS **490**, 4317.

Chevalier, R. A. (1982). *Self-similar solutions for the interaction of stellar ejecta with an external medium*. ApJ **258**, 790.

Cioffi, D. F., C. F. McKee, and E. Bertschinger (1988). *Dynamics of Radiative Supernova Remnants*. ApJ **334**, 252.

Cristofari, P. (2021). *The Hunt for Pevatrons: The Case of Supernova Remnants*. Universe **7**, 324.

Cristofari, P., P. Blasi, and E. Amato (2020). *The low rate of Galactic pevatrons*. Astroparticle Physics **123**, 102492.

Cristofari, P., P. Blasi, and D. Caprioli (2021). *Cosmic ray protons and electrons from supernova remnants*. A&A **650**, A62.

Cristofari, P., P. Blasi, and D. Caprioli (2022). *Microphysics of Diffusive Shock Acceleration: Impact on the Spectrum of Accelerated Particles*. ApJ **930**, 28.

Diesing, R., and D. Caprioli (2021). *Steep Cosmic-Ray Spectra with Revised Diffusive Shock Acceleration*. ApJ **922**, 1.

Dolag, K., F. K. Hansen, M. Roncarelli, and L. Moscardini (2005). *The imprints of local superclusters on the Sunyaev-Zel'dovich signals and their detectability with Planck*. MNRAS **363** (1), 29.

Draine, B. T. (2011). *Physics of the Interstellar and Intergalactic Medium* (Princeton University Press, Princeton).

Drury, L. O. (1983). *An introduction to the theory of diffusive shock acceleration of energetic particles in tenuous plasmas*. Reports on Progress in Physics **46**, 973.

Drury, L. O. (2018). *Cosmic Ray Origin(s) revisited*. Nuclear and Particle Physics Proceedings **297-299**, 6.

Evoli, C. (2020). "The cosmic-ray energy spectrum." .

Fang, K., M. Kerr, R. Blandford, H. Fleischhack, and E. Charles (2022). *Evidence for PeV Proton Acceleration from Fermi-LAT Observations of SNR G106.3 + 2.7*. Phys. Rev. Lett. **129**, 071101.

Fermi, E. (1949). *On the Origin of the Cosmic Radiation*. Physical Review **75**, 1169.

Fermi, E. (1954). *Galactic Magnetic Fields and the Origin of Cosmic Radiation*. ApJ **119**, 1.

Harris, C. R., K. J. Millman, S. J. van der Walt, *et al.* (2020). *Array programming with NumPy*. Nature **585** (7825), 357.

Hess, V. F. (1912). *Über Beobachtungen der durchdringenden Strahlung bei sieben Freiballonfahrten*. Physik. Zeitschr. **13**, 1084.

Hunter, J. D. (2007). *Matplotlib: A 2D graphics environment*. Computing in Science & Engineering **9** (3), 90.

Jones, F. C. (1994). *A Theoretical Review of Diffusive Shock Acceleration*. ApJS **90**, 561.

Jones, F. C., and D. C. Ellison (1991). *The plasma physics of shock acceleration*. Space Sci. Rev. **58** (1), 259.

Krymskii, G. F. (1977). *A regular mechanism for the acceleration of charged particles on the front of a shock wave*. Soviet Physics Doklady **22**, 327.

Longair, M. S. (2011). *High Energy Astrophysics*. 3rd edition (Cambridge University Press, New York).

Maguire, K. (2017). "Type Ia Supernovae." In: *Handbook of Supernovae*. Edited by A. W. Alsabti and

P. Murdin. p. 293.

Misner, C. W., K. S. Thorne, and J. A. Wheeler (1973). *Gravitation* (W.H. Freeman and Company, San Francisco).

Morlino, G., and S. Celli (2021). *Cosmic ray electrons released by supernova remnants*. MNRAS **508**, 6142.

Ostriker, J. P., and C. F. McKee (1988). *Astrophysical blastwaves*. Reviews of Modern Physics **60**, 1.

Padmanabhan, T. (2001). *Theoretical Astrophysics - Volume 2, Stars and Stellar Systems*. Volume 2 (Cambridge University Press, New York).

Pathria, R. K., and P. D. Beale (2022). *Statistical Mechanics*. 4th edition (Academic Press, London).

Ptuskin, V. S., and V. N. Zirakashvili (2003). *Limits on diffusive shock acceleration in supernova remnants in the presence of cosmic-ray streaming instability and wave dissipation*. A&A **403**, 1.

Ptuskin, V. S., and V. N. Zirakashvili (2005). *On the spectrum of high-energy cosmic rays produced by supernova remnants in the presence of strong cosmic-ray streaming instability and wave dissipation*. A&A **429**, 755.

Reichherzer, P., L. Merten, J. Dörner, J. Becker Tjus, M. J. Pueschel, and E. G. Zweibel (2022). *Regimes of cosmic-ray diffusion in Galactic turbulence*. SN Applied Sciences **4**, 15.

Reynolds, S. P. (1998). *Models of Synchrotron X-Rays from Shell Supernova Remnants*. ApJ **493**, 375.

Ruszkowski, M., and C. Pfrommer (2023). *Cosmic ray feedback in galaxies and galaxy clusters – A pedagogical introduction and a topical review of the acceleration, transport, observables, and dynamical impact of cosmic rays*. arXiv e-prints , arXiv:2306.03141arXiv:2306.03141 [astro-ph.HE] .

Schlickeiser, R. (2002). *Cosmic Ray Astrophysics* (Springer-Verlag, Berlin, Heidelberg).

Schure, K. M., and A. R. Bell (2013). *Cosmic ray acceleration in young supernova remnants*. MNRAS **435**, 1174.

Schure, K. M., A. R. Bell, L. O'C. Drury, and A. M. Bykov (2012). *Diffusive Shock Acceleration and Magnetic Field Amplification*. Space Sci. Rev. **173**, 491.

Springel, V. (2005). *The cosmological simulation code GADGET-2*. MNRAS **364**, 1105.

Springel, V., and L. Hernquist (2003). *Cosmological smoothed particle hydrodynamics simulations: a hybrid multiphase model for star formation*. MNRAS **339**, 289.

Tang, X., and R. A. Chevalier (2017). *Shock evolution in non-radiative supernova remnants*. MNRAS **465**, 3793.

Thorne, K. S., and R. D. Blandford (2017). *Modern Classical Physics: Optics, Fluids, Plasmas, Elasticity, Relativity, and Statistical Physics* (Princeton University Press, Princeton).

Thoudam, S., J. P. Rachen, A. van Vliet, A. Achterberg, S. Buitink, H. Falcke, and J. R. Hörandel (2016). *Cosmic-ray energy spectrum and composition up to the ankle: the case for a second Galactic component*. A&A **595**, A33.

Tiesinga, E., P. J. Mohr, D. B. Newell, and B. N. Taylor (2021). *CODATA recommended values of the fundamental physical constants: 2018**. Reviews of Modern Physics **93**, 025010.

Tornatore, L., S. Borgani, K. Dolag, and F. Matteucci (2007). *Chemical enrichment of galaxy clusters from hydrodynamical simulations*. MNRAS **382**, 1050.

Truelove, J. K., and C. F. McKee (1999). *Evolution of Nonradiative Supernova Remnants*. ApJS **120**, 299.

Truelove, J. K., and C. F. McKee (2000). *Erratum: Evolution of Nonradiative Supernova Remnants*. ApJS **128**, 403.

Urošević, D., B. Arbutina, and D. Onić (2019). *Particle acceleration in interstellar shocks*. Ap&SS **364**,

185.

van Weeren, R. J., F. de Gasperin, H. Akamatsu, M. Brüggen, L. Feretti, H. Kang, A. Stroe, and F. Zandanel (2019). *Diffuse Radio Emission from Galaxy Clusters*. Space Sci. Rev. **215**, 16.

Vink, J. (2020). *Physics and Evolution of Supernova Remnants*. Astronomy and Astrophysics Library (Springer Nature Switzerland AG, Cham).

Wittor, D. (2021). *On the Challenges of Cosmic-Ray Proton Shock Acceleration in the Intracluster Medium*. New Astron. **85**, 101550.

Wolfram Research Inc., (2021). "Mathematica, Version 12.3." Champaign, IL, 2021.

Zirakashvili, V. N., and F. Aharonian (2007). *Analytical solutions for energy spectra of electrons accelerated by nonrelativistic shock-waves in shell type supernova remnants*. A&A **465** (3), 695.

Danksagung

Die Fertigstellung dieser Masterarbeit wäre ohne die Hilfe zahlreicher Personen nicht möglich gewesen. Abschließend möchte ich mich ganz besonders bedanken bei

- Klaus Dolag, der mir dieses (mir damals weitgehend unbekannte) Thema vorgeschlagen hat und von frühmorgens bis spätabends an der Sternwarte für Fragen verfügbar war. Ich habe im vergangenen Jahr unglaublich viel Neues gelernt, denn bei kaum einem anderen Masterthema hätte man so viele Fachgebiete miteinander verknüpfen können. Ich freue mich bereits auf die weitere Zusammenarbeit!

- Ildar Khabibullin, der mich laufend mit Literatur versorgt hat (darunter auch ein paar russische Schmankerl aus den 1960er Jahren) und sogar eigene Übungsaufgaben "zur Einstimmung" entworfen hat. Herzlichen Dank auch für die anregenden Diskussionen (im Spannungsfeld zwischen Physik, Mathematik und Philosophie) und die ausführliche Rückmeldung zu einem ersten Entwurf dieser Arbeit.

- Ludwig Böss, auf dessen umfangreiches Modul für kosmische Strahlung in *OpenGadget3* ich direkt aufbauen konnte. Danke auch für die vielen nützlichen Praxistipps sowie die große Hilfe bei der Implementierung und beim Aufsetzen der Simulationen.

- Leonard Romano, der mich mit zahlreichen Infos bezüglich der zeitlichen Entwicklung von Supernovaüberresten versorgt hat.

- Giovanni Morlino, der mir freundlicherweise sein Mathematica Notebook zur Verfügung gestellt hat, mit dem ich letztendlich die Spektren für Protonen und Elektronen berechnet habe.

- Der CAST-Gruppe für die freundliche Arbeitsumgebung und den regen gedanklichen Austausch über alle möglichen Themenbereiche: von A wie Axion-Quark-Nuggets bis Z wie Zwerggalaxie.

- Meinen Eltern, für die laufende Unterstützung und den positiven Zuspruch, ohne den ich es vermutlich gar nicht erst nach München geschafft hätte.

Selbstständigkeitserklärung

Hiermit erkläre ich, Daniel Karner, die vorliegende Arbeit selbstständig verfasst zu haben und keine anderen als die in der Arbeit angegebenen Quellen und Hilfsmittel benutzt zu haben.

Ort, Datum der Abgabe

Unterschrift